The Dissertation Committee for Corey Michael Staller Certifies that this is the approved version of the following Dissertation:

Electron Transport in Doped Semiconductor Nanocrystals

Committee:

Delia Milliron, Supervisor

Deji Akinwande

Brian Korgel

C. Buddie Mullins

Electron Transport in Doped Semiconductor Nanocrystals

by

Corey Michael Staller

Dissertation

Presented to the Faculty of the Graduate School of

The University of Texas at Austin

in Partial Fulfillment

of the Requirements

for the Degree of

Doctor of Philosophy

The University of Texas at Austin
December 2018

Acknowledgements

The completion of a PhD is achieved through long hours, hard work, and being headstrong enough to keep pushing through a tidal wave of failure. This is sometimes mistakenly given as a credit to the individual who is newly minted as “doctor.” It is instead equally an achievement of the people with whom the individual has interacted. They might be a labmate that was accepting of the individual’s strong personality, a personal confidant that provided a hug on a bad day, or a one the many forms of mentors that taught the individual tools to be successful. Whatever I have achieved with the submission of this dissertation is thanks to the incredible people I have met along the way.

I came to The University of Texas at Austin with the sole intent of working under Professor Delia Milliron. As such, I would like to start with a gracious thank you to Delia. I had the pleasure of interacting with Delia as her student, her teaching assistant, and her graduate student. I can unequivocally state that Delia embodied the epitome of an ideal professor in all aspects (although writing ten homework assignments as your teaching assistant sucks, I won’t hold that against you). Thank you for welcoming me early in my career and taking my omnipresent group meeting commentary seriously as I developed into a scientist. The trust you have in me to know my field and to solve difficult problems is truly humbling. I would be a shadow of the scientist I am today without the four years of tutelage from you and, yet, know there is still so much you could teach me.

To the post-doctoral researchers I have worked with directly, Ajay, Byung Hyo, Gabriel, Omid, and Yang, thank you for teaching me and being a pleasure to interact with. Ajay, thank you for taking time to teach me your CZTS synthesis and for teaching me that sometimes it is OK to take minimal but sufficient notes, even if it frustrates others. Also, I’m sorry about that one time I broke your thermocouple finger in my first year. Byung Hyo, thank you for always being available to help me in lab and for teaching me your sol-gel infill procedure. Gabriel, thank you for being humble, witty, and personable. You make everyone around you better by providing an example of an amazing person and scientist. Omid, thank you for teaching me ALD, helping me expand my knowledge of depletion, and having interesting scientific discussion with me. Yang, thank you for constantly smiling and brightening the mood. It made the early years of graduate school tolerable.

To the past graduate students I have interacted with, thank you for helpful feedback, interesting talks, and making tough times a little better. Amy, from one Midwesterner to another, thank you for making the group and Austin feel like home. You were always willing to inconvenience yourself to help others, reassured me to pay no mind to whatever was frustrating me, and were a good friend. Evan, thank you for your constant guidance, acting as a second adviser and lab manager, and taking time to help me when you did not really want to or need to. I will never forget you telling me in my first year to never treat a technique or phenomenon as a black box. Ankit, thank you for endless amounts of talking about science and not getting frustrated when your long deposition was met with “wait… what?” You are a great coworker, coauthor, and friend. Clay, thank you for being the nicest person on planet earth and a humble, thorough, and incredibly intelligent scientist. I have never been more lost than when you brought up high level quantum physics, like, every group meeting. Rob, thank you for giving me critical feedback despite your hatred of transport, caring strongly about helping labmates’ science, constantly trying to make me be social, and reassurances of the normalcy of imposter syndrome. Our too long and often way too late League of Legends sessions were a blast. Gary, Gary, Gary, what is there to say about ole Gare-bear? Gary, thank you for teaching me how to discuss science fluently and efficiently, constantly pushing me to explain my argument better, and endless philosophic discussions about any topic imaginable. I can, with full honesty, say you must be the most intelligent person I have ever met, neurotic as hell, but intelligent. You are going to do something incredible with your time on Earth and I look forward to watching it happen.

To the current graduate students I have interacted with, thank you for good times and good lessons. Sungyeon, thank you for having endless grit, silently managing the lab, doing anything for anybody at any time, and still managing to be a caring father and husband. You are the most underappreciated member of our lab. Camila, thank you for growing to appreciate my sometimes brash personality, exchanging feedback with me, sharing those lab management burdens with Sungyeon, and doing high level science while grinding through grant proposals. Shin, thank you for being the most over the top person in the Milliron lab. You seamlessly mix a high level understanding of synthesis and materials chemistry with crazy conspiracies and aspirations(?) of industrial military complex riches. You're a national treasure. Never change. Lauren, thank you for your strong emphasis on physical and mental health in group meeting and assistance in making the Milliron lab a safe place to work. Young Stephen, I wanted so badly to omit you ala Gary, but I could not bring myself to do such a thing. As such: Young Stephen, thank you for being a good colleague and friend. You are a critical thinker, a problem solver, and reliable person. You have earned every right to relinquish the moniker "Young Stephen" as you're everything a PI could want in a senior member. Therefore: Stephen, I hope that you never forget that you are a true LSPR expert, high quality scientist, and a, in your words, "gosh damn" phenomenal person. Manny, thank you for adventuring into a new project with me (and not holding it against me for having to pull out of the project), watching my dogs at a moment's notice, and being a chill goofball. I hope you develop your confidence and learn to venture self-assuredly into topics that make you uncomfortable as you mature as a scientist. You are an expert of surface chemistry and assembling NCs. You have earned the right to be confident in your opinions. Dan and Natalie, thank you for being amazing friends. Thank you for the many drinks and increasingly pessimistic outlooks on science as the drinks piled up until we forgot we were graduate students and became just drunk folks at a bar (or, more often, Brennan's house). You are truly awesome and caring people. Brennan, thank you for being my best friend in graduate school. You project nothing but positive feelings, are interested in nothing more than making those you care about happy, and never waver in being there if I need you. I hope life finds a way to give you everything you deserve. Thank you for good times, good workouts, good beers, and good company.

To my collaborators, thank you for long talks and reliable results. Ben, thank you for always questioning my analysis to the benefit of us both, constructively accepting when we have disagreeing theories, and bending over backwards to bring us to a successful paper. Zack, thank you for prioritizing running my samples on the PPMS, always being up for a good discussion, and leaving an open invitation to future collaborations. My collaboration with Ben and Zack was the type of collaboration that makes other scientists jealous and moves science forward leaps and bounds. Katelyn, thank you for being understanding when things do not go forward smoothly and being on the ball with feedback. Elijah, thank you for your endless interest in discussing science and willingness to freely engage in collaboration.

Before mentioning the folks I knew prior to UT, an interjection is necessary. If I have accomplished anything during my time at UT, it is meeting, interacting with, and working with some of the most amazing and brilliant people on this planet. I can walk away assured that, no matter what happens to my science, I will remember each of you and hold our interaction as an achievement.

I would now like to thank my parents, Will and Stacey, and my brother, Derek. Thank you for unlimited amounts of support throughout my life and science career. You were given a giant task in consistently trying to teach me the importance of education and getting me to take school seriously. You supported me when I was devastated that every university rejected my application and Mizzou was the only school that accepted me. You continued to encourage me when I had academic success at Mizzou. You supported me when I decided I needed to attend graduate school because I needed to prove something to myself, even though it was a financially questionable decision. And finally, you were very understanding when graduate school meant I could not visit you often because I had to study for qualifiers or was too stressed out to leave work or needed to finish a paper before the New Year. I hope you can look back and say the, assuredly stressful, times of watching me do everything in my power to make bad choices were worth the person I have become. I am eternally grateful.

Finally, thank you to Camille. If I dared to aspire to properly thank you, I would need to write another dissertation titled “Why I am thankful for Camille” that would most assuredly rival this one in length. Thank you for taking a risk in engaging in a relationship with some guy that lived 3 hours away because we had undeniable chemistry. Thank you for supporting me for the past 6.5+ years. You were supportive when I didn’t respond to your texts because I was busy wrecking myself at library from 9AM to 2AM for weeks at a time and when I could not see you for a month at a time because I was too busy to take a weekend off. Thank you for moving 900 miles to Austin, Texas with me to face adversity, nonstop stress, and endlessly missing your family. You have personally sacrificed more than anybody could reasonably ask of another person and never held it against me or my pursuit of science. I am nothing but proud to be with you. You are an amazingly caring, stunningly beautiful, supremely intelligent, and astoundingly thoughtful person. I hope I have made you feel proud, fulfilled, loved, and, most importantly, happy over the years and can continue to do so *ad infinitum*.

Abstract

Electron Transport in Doped Semiconductor Nanocrystals

Corey Michael Staller, PhD
The University of Texas at Austin, 2018

Supervisor: Delia Milliron

Electron transport through semiconductor nanocrystal (NC) systems is almost entirely understood by analogs to bulk science. The physics governing electron transport within NCs is entirely analogous to bulk semiconductors with extreme spatial constraints. In contrast, the physics of electrons conducting between NCs is understood through the physics of amorphous materials, granular metals, or bulk semiconductors, depending on the structure of the NC ensemble. Herein is an investigation of how dopant distribution engineering can be utilized to modulate near surface depletion in NC films. The dependence of NC film conductivity on dopant distribution is eliminated by surface passivation. A code to fit the optical absorption of colloidal NCs is developed to account for surface scattering, depletion, size heterogeneity, and dopant heterogeneity. This code is used to define the conduction within an individual NC. The intra-NC conduction is used as a metric to describe and define the phase diagram of NC film electron transport. Using the criteria developed here, we make metallic films in a controlled manner.

This work illustrates an overview of bulk electron transport and an introduction of NC film electron transport in Chapter 1. These descriptions will then be used to investigate the powerful capability to engineer intra-NC dopant distribution to manipulate NC film conductivity in Chapter 2. The intra-NC conductance is then investigated using a

novel code to fit the optical absorption of NCs in Chapter 3. With a deep understanding of intra-NC transport, the electron transport phase diagram is constructed in Chapter 4.

Table of Contents

List of Tables

List of Figures

Chapter 1: Introduction

Much of the underlying physics that describes NC electron transport was previously established in or draws very heavily upon solid state physics models for crystalline and amorphous materials. A useful starting point for envisioning a NC system is such that the intra-NC dynamics are governed by crystalline transport equations under extreme geometric constrains while the inter-NC dynamics are governed by amorphous transport concepts and equations. For this reason, it is important to review conduction through bulk materials prior to examination of electron transport in nanocrystal (NC) systems. Rather than a complete review of crystalline transport, in the interest of brevity, this section will only discuss bulk metallic transport due to its relevance to the work presented.

CONDUCTION IN BULK MATERIALS

Metallic Conduction

Metallic conduction throughout this work will be treated under the Drude model and the free electron approximation. This framework assumes conduction electrons act as a gas in which electrons are non-interacting, undergo diffuse (non-directional) scattering events instantaneously, and move ballistically between scattering events. The atoms, in contrast, are assumed to be stationary. The Drude conductivity, σ, is described by (1.1).[1]

$$\sigma = \frac{n_e q^2 \tau}{m^*} \qquad (1.1)$$

where n_e is the electron concentration, q is the electron charge, τ is the relaxation time (time between scattering events), and m^* is the effective electron mass. Examination of (1.1) shows two measureable properties (σ & n), one universal constant (q), and two immeasurable properties (τ & m^*). The effective electron mass is defined through quantum mechanics to simply define the curvature of the conduction band and can thus be derived theoretically, leaving only the relaxation time as an unknown. Due to inadequacies of the Drude model to account for various scattering sources, the relaxation time has been defined in an ad hoc manner to explain various conduction phenomena.

The relaxation time is defined by (1.2).

$$\tau = \frac{l}{v_F} \qquad (1.2)$$

where l is the mean free path of an electron and v_F is the Fermi velocity defined by (1.3).

$$v_F = \frac{\hbar}{m^*}(3\pi^2 n_e)^{\frac{1}{3}} \qquad (1.3)$$

where $\hbar$ is Planck's constant. The Fermi velocity is the effective velocity affected on an electron in a material based on its momentum. Perhaps more intuitively, the mean free path is the distance an electron travels between scattering events in the material. There are many scattering sources in a given material, such as grain boundaries, impurities (ionized and neutral), electron-electron, electron-phonon, surfaces, etc. While it may seem overwhelming to sum each of these scattering sources to get a mean spacing, the empirical Mathhiessen's rule provides a simple calculation (1.4).

$$\frac{1}{l} = \sum \frac{1}{l_i} \qquad (1.4)$$

where l_i is the mean free path accounting for only scattering source i. Matthiessen's rule states that the effective mean free path and, thus, the conductivity is dominated by the scattering source with the shortest mean free path.

The two defining characteristics of metallic electron transport are a finite resistivity at 0K and a positive trend of resistivity with temperature as shown in Figure 1.1 for an Ag thin film.[1,2] The finite resistivity at 0K comes as a result of metals exhibiting a non-thermally activated electron concentration. The positive slope of resistivity with temperature is due to electron-phonon scattering as the main scattering source for metallic materials at a constant electron concentration. Additionally, Figure 1.1 shows the effect of surface scattering across a range of film thicknesses, illustrating the concept of Mathhiessen's rule.

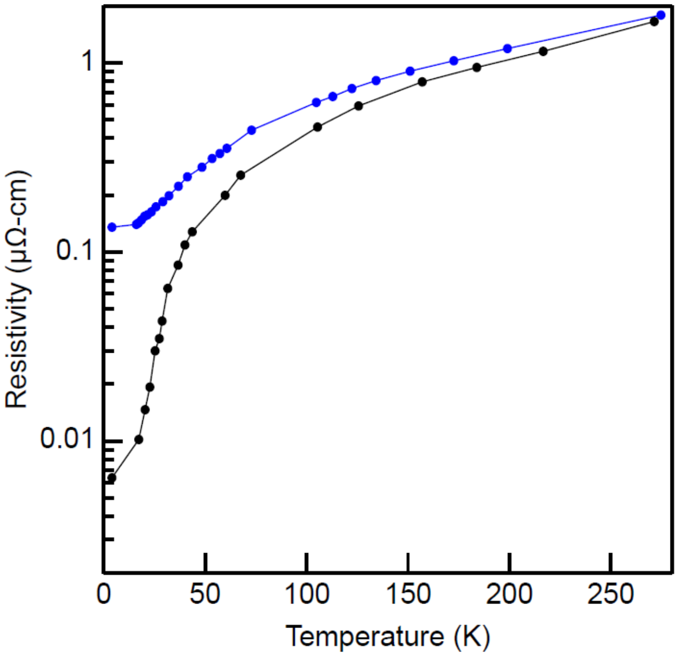

Figure 1.1: Temperature dependent resistivity in thin Ag films shows finite resistivity at 0K and a positive trend of resistivity with temperature. 170nm thick Ag film (blue) is significantly more resistive than bulk films (black). Mathhiessen's rule gives a strong dependence of resistivity on film thickness. Reproduced from ref 2.

Amorphous Conduction

Amorphous materials are defined by a lack of long-range atomic order yielding dire electronic consequences. A typical metallic density of states is shown in Figure 1.2a compared to that of an amorphous material (Figure 1.2b).[3–5] Amorphous materials have density of states that tail into the band gap caused by the short-range order present throughout the material, which on first inspection might seem to destroy the band gap and improve conduction. This is not the case, however, as these mid gap states are localized to these regions of order. This results in a mobility gap.[3] The mobility edge defines the electron energy at which states are delocalized (above the mobility edge in the conduction band or below the mobility edge in the valence band). The shape of the density of states and the mobility edge energy depends on the degree of ordering within and the composition of the amorphous material.

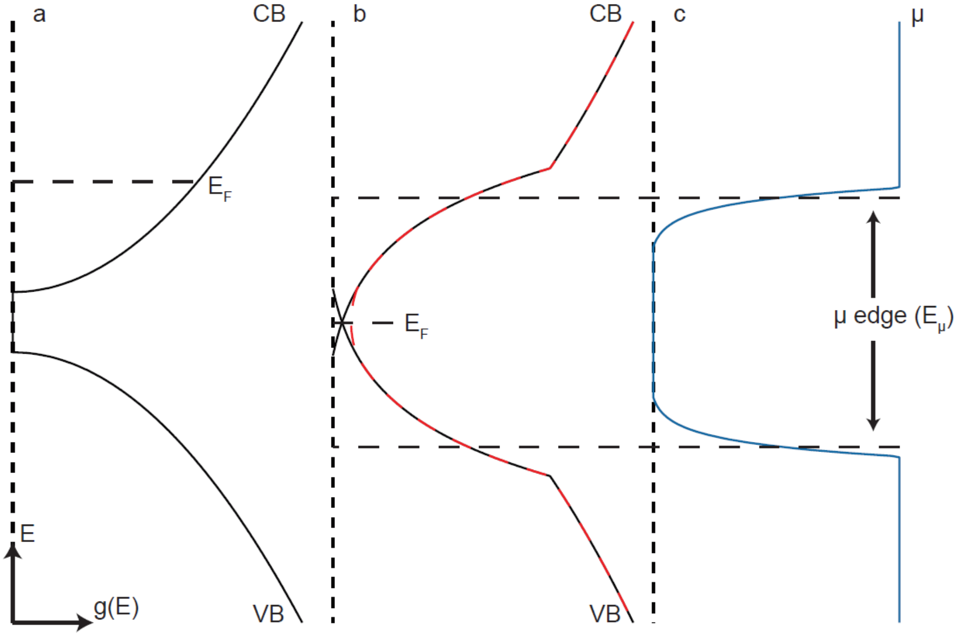

Figure 1.2: Density of states for metal (a) and amorphous (b) materials. States which would be forbidden in a crystalline material, such as within the band gap, are instead occupied in amorphous materials. These states are localized, however, and result in a mobility edge (c) that defines the energy of mobile carriers.

Localization of conduction electrons within the mobility gap has significant consequences for the mechanisms of electron transport. While electrons in a Drude system move ballistically between scattering events, localized electrons must overcome both a spatial barrier of distance, r_{ij}, and an energetic barrier, E_A, to move (Figure 1.3).[6] Each energy well has some characteristic size, a, known as the electron localization length, and is simply defined as the inverse of the wavefunction decay rate. The wavefunction decay rate scales as the square root of the depth of the well ($E_\mu - E_F$). The phenomenon involved in the migration of electrons between these energy wells is an inelastic tunneling process referred to as hopping. The Miller-Abraham model (1.5) describes charge carrier hopping mechanisms.[7]

$$\sigma \propto Aexp\left(-\frac{2r_{ij}}{a}\right) exp\left(-\frac{E_{ij}}{k_B T}\right) \qquad (1.5)$$

where σ is conductivity, A is a material-dependent constant, r_{ij} is the distance between sites i and j, a is the inverse of the wavefunction decay rate (called the electron localization length), E_{ij} is the energetic barrier encountered moving from site i to j, k_B is the Boltzmann constant, and T is temperature. The Miller-Abraham model is a multiplication of a thermal Boltzmann probability and a spatial tunnel junction probability. Conductivity in a hopping system is governed simply by the most probable electron transitions; that is, hops of the shortest distance for the lowest energetic penalty.

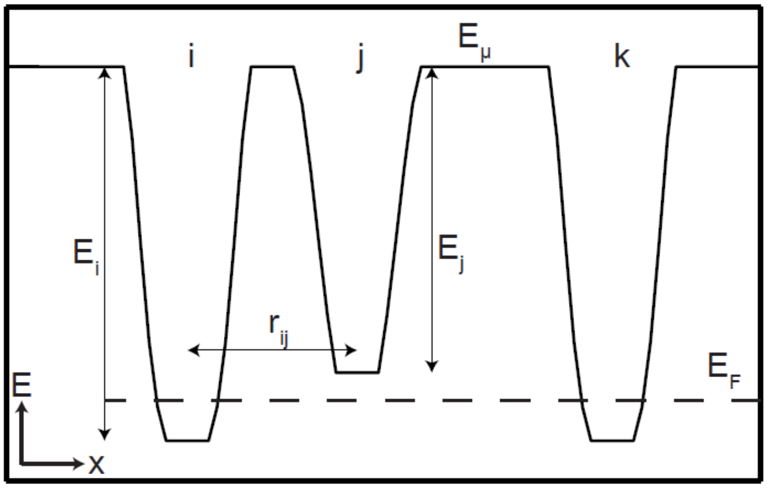

Figure 1.3: Energy well diagram. Example of three NCs in series in E-x space shows varying well depths and spacing.

Consider the simplest case where each hop will be conducted between neighboring wells. Such a situation will occur when there is low variation in the energetic barrier or when the energetic barrier to hopping is small relative to thermal energy. The result is a substantial probability "penalty" for hops further than nearest neighbor without a significant benefit to thermal activation probability. This case is known as nearest neighbor hopping and its temperature dependence is described by (1.6).[5]

$$\sigma = Bexp\left(-\frac{E_A}{k_B T}\right) \qquad (1.6)$$

where B is a constant and E_A is the effective activation energy. In nearest neighbor hopping, the spatial component is combined into the temperature independent pre-exponential constant. Thermally, this process varies as a simple Arrhenius activated process where the activation energy is nonspecific to any particular energetic barrier, rather a summation of all energy changes undergone by an electron during a given hop.

Consider the case where the energetic barrier to hopping varies wildly or is significantly above thermal energy and the most probable hopping distance is not the nearest neighbor as that hop may have a low energetic probability. Instead, the electron loses favorability in the spatial probability to gain a heavy favorability in energetic probability by hopping beyond the nearest neighbor to a site of lower energetic cost. As temperature increases, the energetic benefits of hopping further become lessened relative to thermal energy and the average hop distance shortens. This situation is known as variable range hopping (VRH). The rate at which the average hop distance changes with temperature is dependent on the origin of the energetic barrier.

There are two primary VRH mechanisms: Mott VRH and Efros-Shklovskii VRH, which differ in the energetic barrier origin and exhibit different thermal dependences. Mott VRH assumes that the density of states is constant throughout an energy range, $E_F \pm E_A$. This is true when the only contribution to the energetic barrier is the difference in energy between the initial and final states of the electron. This assumption is valid for samples of large localization length or high dielectric constant as will be discussed later.

Mott VRH is a common conduction mechanism for amorphous intrinsic semiconductors such as Si and Ge.

Mott VRH temperature dependence is described by (1.7a).[6]

$$\sigma = Cexp\left(-\left(\frac{T_0^m}{T}\right)^{0.25}\right) \qquad (1.7a)$$

where C is a constant and the characteristic temperature, T_0^m, is

$$T_0^m = \frac{21.2}{k_B g(E_F)\xi^3} \qquad (1.7b)$$

where $g(E_F)$ is the density of states at the Fermi energy.

In contrast to Mott VRH, Efros-Shklovskii VRH does not assume a constant density of states at the Fermi energy. Instead, conduction electrons must overcome a capacitive energetic barrier to move from site i to j, known as charging energy. This, in effect, causes the density of states to bend about the Fermi energy where an electron at the Fermi energy cannot contribute to conduction. Density of states bending occurs in a charging energy dominated system and not a Mott system. In a charging energy dominated system, an electron may not be spontaneously added to an electron cloud without paying an energetic penalty. This results in zero density of states at the Fermi energy, known as a Coulomb gap.[8] The density of states increases as energy squared about the Fermi energy as shown in Figure 1.4 Efros-Shklovskii VRH is a common conduction mechanism for amorphous doped semiconductors such as P:Ge. The non-constant density of states near the Fermi energy gives rise to differing thermal dependence shown in (1.8a).

$$\sigma = Dexp\left(-\left(\frac{(T_0^{ES})}{T}\right)^{0.5}\right) \qquad (1.8a)$$

where D is a constant and the characteristic temperature, T_0^{ES}, is

$$T_0^{ES} = \frac{(2.8q^2)}{4\pi\varepsilon\varepsilon_0\xi k_B} \qquad (1.8b)$$

where ε is the static dielectric constant and ε_0 is the permittivity of free space.

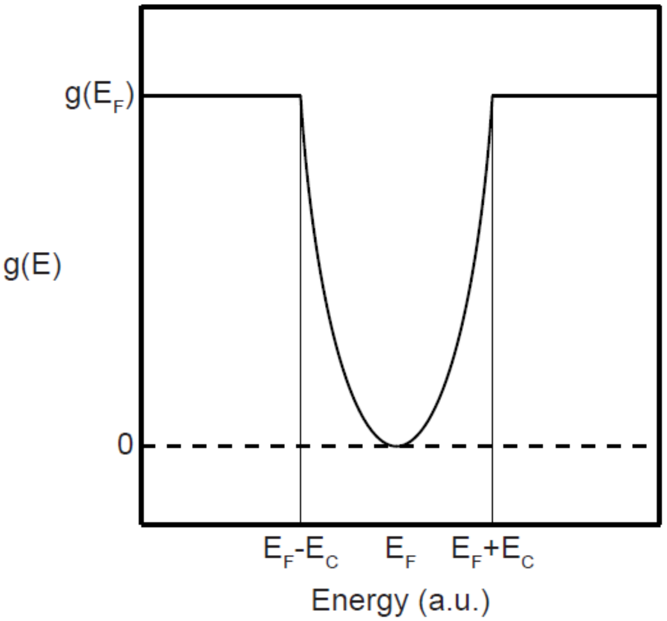

Figure 1.4: Density of states in the Efros-Shklovskii model.

DOPED METAL OXIDES

There is not a person in the world that has spent a day in a developed nation and not seen or interacted with a metal oxide. Metal oxides are ubiquitous in daily life due to the flexibility in physical properties they display. Metal oxides are used in catalytic, electronic, optical, and sensing applications. The assortment of applications incorporating metal oxides stems from exploitation of well-known defect chemistries.

Defects in Metal Oxides

Many types of defects are prominent in metal oxides. Of principle interest in this work are those that modulate conductivity through controlling electron concentration. The numerous defects in this category include intrinsic defects (metal/oxygen vacancies, metal/oxygen interstitials, and defect/interstitial clusters) and extrinsic defects (ionized dopants and neutral dopant clusters). This section will focus on those that are most common and consider indium oxide as a model system. The most prominent intrinsic defect is the oxygen vacancy (1.9).[9]

$$O_O^x \rightarrow \frac{1}{2}O_2(g) + V_O^{\bullet\bullet} + 2e' \quad (1.9)$$

Oxygen vacancy doped indium oxide films have electron concentrations ranging from 1E15 – 4E20 cm^{-3}, representing oxygen vacancy densities of 5E14 – 2E20 cm^{-3} (0 atomic% – 0 atomic% $V_O^{\bullet\bullet}$).[9,10] The electron concentration of an indium oxide film is largely influenced by the partial pressure of oxygen within which the material is exposed and the temperature of material synthesis or deposition. The upper end of electron concentration expands with the introduction of extrinsic aliovalent dopants. Indium oxide is accepting of a wide array of dopants such as Mn, Fe, Co, Sn, etc. Due to the relevance to later chapters, tin-doped indium oxide (Sn:In_2O_3, ITO) is examined here (1.10).[9]

$$SnO_2 \xrightarrow{In_2O_3} Sn_{In}^{\bullet} + O_O^x + e' + \frac{1}{2}O_2(g) \quad (1.10)$$

ITO films have electron concentrations up to 1.5E21 cm^{-3} at 10 atomic% Sn.[10] This high electron concentration is very high; however, when the density of Sn atoms at 10 atomic% Sn (3E21 cm^{-3}), the activation of dopants is only half.[9–11] This is the result of a dopant compensation region of the Brouwer diagram for ITO. Below ~3 atomic% Sn dopant activation is very nearly unity. Above this, dopant activation decreases monotonically with each additional dopant. This results from the formation of neutral $2Sn_{In}^{\bullet}O_i''$ cluster formation (1.11).[9,12]

$$(2Sn_{In}^{\bullet}O_i'')^x \rightarrow \frac{1}{2}O_2(g) + 2Sn_{In}^{\bullet} + 2e' \quad (1.11)$$

Though neutral defect clusters have a deleterious effect on the conductivity of ITO films, such defects do not override the enormous boost granted by higher electron concentration even with 50% activation at 10 atomic% Sn. As a result ITO films, ubiquitous in technologies today, are often 10 atomic% Sn.

Transparent Conductive Oxides

Transparent conductive oxide (TCO) films are implemented as the transparent electrode in electronic displays, solar cells, and electrochromic devices. Metal oxide films are the ideal material for transparent electrodes due to their high transparency and conductivity. Many metal oxides have band gaps well over 3 eV and do not exhibit other absorption processes in the visible spectrum.[13] Additionally, metal oxide conductivity can be tuned for specific applications by changing dopant concentration.[9,10,14] The choice of material for TCOs is motivated by a cost-benefit analysis where ITO, while exhibiting very high conductivity, is expensive and aluminum-doped zinc oxide (AZO), while cost effective, exhibits a lower conductivity. Despite the higher cost of ITO, it dominates the TCO market.

The primary advantage of ITO over other metal oxide TCOs is the higher upper limit of conductivity of 2E4 S/cm. This high upper limit does not come with an inability to achieve lower conductivity films, however. Highly oxygen vacancy doped indium oxide films exhibit electron mobility near 100 cm^2/Vs and conductivity over 2E3 S/cm.[10] Electron mobility in ITO goes as $n_e^{-2/3}$.[9] This causes highly doped ITO to exhibit conductivity 5x that of indium oxide despite having more than 10x higher electron concentration. Though manipulation of dopant concentration in ITO is a powerful technique for manipulating conductivity, the practicality of this approach is limited due to the deposition techniques typically used.

ITO thin films are deposited using sputtering techniques in high vacuum. The benefits of such deposition techniques are the reproducibility and high conductivity. However, such vacuum deposition techniques require a sputtering target of the precise composition desired for the thin film. This makes using composition to control conductivity extremely cost prohibitive. The typical ITO film for TCO applications is 10 mass% Sn ITO and the film conductivity is manipulated through the crystallite grain size of the film. This technique allows film conductivity to range from 1 to 1E4 S/cm.

Electron conduction in ITO thin films proceeds through metallic transport (Figure 1.5).[15] The resistivity of ITO thin films increases linearly with temperature. This temperature dependence results from electron-phonon scattering, which increases linearly with temperature in ITO. The resistivity flattens out at low temperatures as resistivity is dominated by ionized impurity scattering. ITO sample resistivity of this form is indicative, though not a sufficient condition, of a metal.

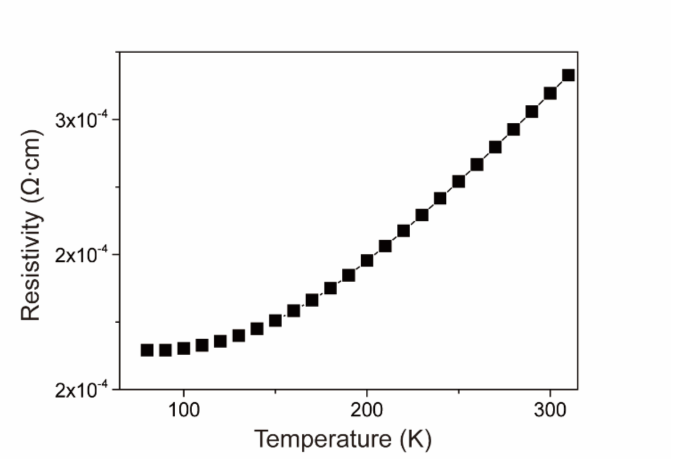

Figure 1.5: Temperature dependent resistivity of a commercial ITO thin film shows metallic transport. Reproduced from ref 15.

CHARGE TRANSPORT IN NANOCRYSTALS

TCO thin films are of fundamental importance in the modern world due to their vast applications.[14,16] These applications require high conductivity, which has traditionally been achieved through vacuum deposition of amorphous or crystalline doped metal oxide films. An effort to reduce manufacturing cost by moving away from vacuum deposition has motivated research on using films of colloidal nanocrystals (NCs) as TCO films.[16] However, colloidal NCs are synthesized with long chain organic capping ligands resulting in spatial separations between neighboring NCs that act as tunneling barriers (Figure 1.6).[17–19] Separation of NCs by ligands causes the localization of conduction electrons. Due to electron localization, much like amorphous semiconductors, electron transport proceeds through a hopping mechanism and is governed by the Miller-Abraham model. Inspection of (1.5) leads to two obvious routes to improve NC film conductivity – reducing the distance between sites and lowering the energetic cost of hopping.

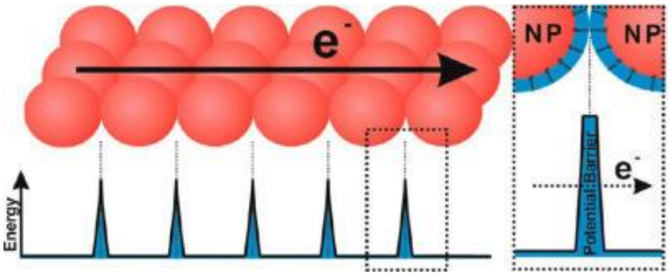

Figure 1.6: The charge transport dilemma is based on the spatial separation of electron clouds caused by insulating ligands. Reproduced from Ref 17.

Varying Ligands

Many efforts have focused on reducing the distance between NCs to improve electron transport through NC films. Initial work on colloidally synthesized NC films concentrated on exchanging the organic capping ligands used in synthesis with a variety of organic ligands of different lengths or bonding arrangements to modify inter-NC charge transfer or hopping.[18–21] The effects of ligand length are most clearly illustrated in films of ligand-capped Au nanoparticles (NPs). Wuelfing et al. investigated the effect of thiol ligand length on ~2nm diameter Au NPs (Figure 1.7a).[22] They find an exponential dependence of conductivity on ligand length down to C5 where the conductivity saturates. Several years later, Zabet-Khosousi et al. investigated the use of bifunctional thiol ligands to modulate conductivity of films of 5nm diameter Au NPs (Figure 1.7b).[23] The observed an abrupt metal-insulator transition (MIT) at C5. On the metallic side of the MIT conductivity showed no clear dependence on ligand length, illustrating a high degree of wavefunction overlap between NPs.

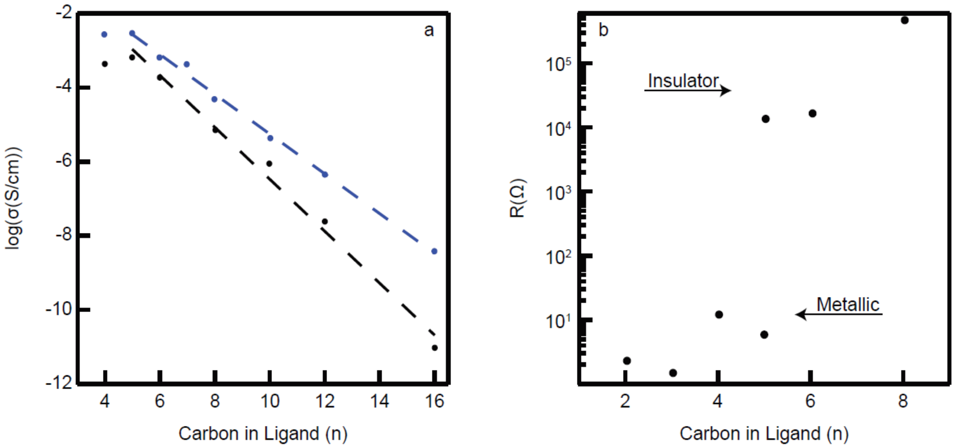

Figure 1.7: Effect of ligand length on conductivity. Plot of conductivity at 70 (blue) and -60 °C (black) vs number of carbons in the alkanethiolate chains of Au NPs (1.5) (a). Resistance of thiol cross linked Au NP films at 200 K as a function of n (b). Reproduced from ref 22 (a) and 23 (b).

The observations of ligand length influencing Au NP film conductivity were qualitatively reproduced in semiconductor NC films. Zarghami et al. investigated exchanging long oleate (C18) ligands with formic (C1), acetic (C2), and oxalic (C2, bicarbonate) ligands *in situ* in films of PbSe NCs.[19] This work found a ~20x increase in film conductivity for formate-capped NCs compared to acetate-capped NCs. Interestingly, this study used C2 bicarbonate and C1 carbonate ligands and was unable to observe a MIT for semiconductor NCs. Semiconductor NC films with any ligands still in place are unable to access the MIT or achieve conductivity comparable to bulk materials.

Various ligand stripping and decomposition reactions have been developed to improve the conductivity of NC films. Among these strategies is the decomposition of formate ligands. Garcia et al. used an *in situ* formic acid ligand exchange followed by annealing under inert conditions to yield a ligand-free NC film.[24] Other strategies have been the use of colloidal ligand removal such as those developed by Dong et al.[25] Removal of ligands from NC surfaces often leads to several orders of magnitude increase in conductivity. While this strategy significantly improves film conductivity, removal of ligands exposes NC surfaces to adventitious chemical species, such as water that leads to hydroxylation, forming surface states that are difficult to control and can be harmful to charge transport through NC films.

Near Surface Depletion

One method to improve conduction through NC films is to use atomic layer deposition (ALD) to cap bare NC arrays with metal oxides, such as alumina (Al_2O_3).[26–29] Specifically, Thimsen et al. found that ZnO NC films with alumina capping layers had conductivity eight orders of magnitude higher than that of bare films.[26] Ephraim et al. investigated the cause of the significant conductivity improvement using *in situ* resistivity measurements of ZnO NC films under exposure to forming gas, a common reducing treatment.[27] Forming gas exposed samples asymptotically approach the resistivity of alumina infilled films (Figure 1.8). This implies the significant film performance improvement following alumina deposition is due to the removal of adsorbed water species by trimethylaluminum, the precursor used during alumina ALD. These studies suggest that adsorbed water species play a direct role in affecting film conductivity but the mechanism by which adsorbed water species actually lead to reduced conductivity remained unexplored. Zandi and Agrawal et. al. reported that electrochemical modulation of optical absorption in tin-doped indium oxide (ITO) NC films can be explained by the formation of a depletion region near NC surfaces.[30,31] We can therefore hypothesize that the enhanced electron transport in films whose surface hydroxyls have been eliminated is a result of alleviating depletion effects that were present due to the hydroxyl-associated surface states.

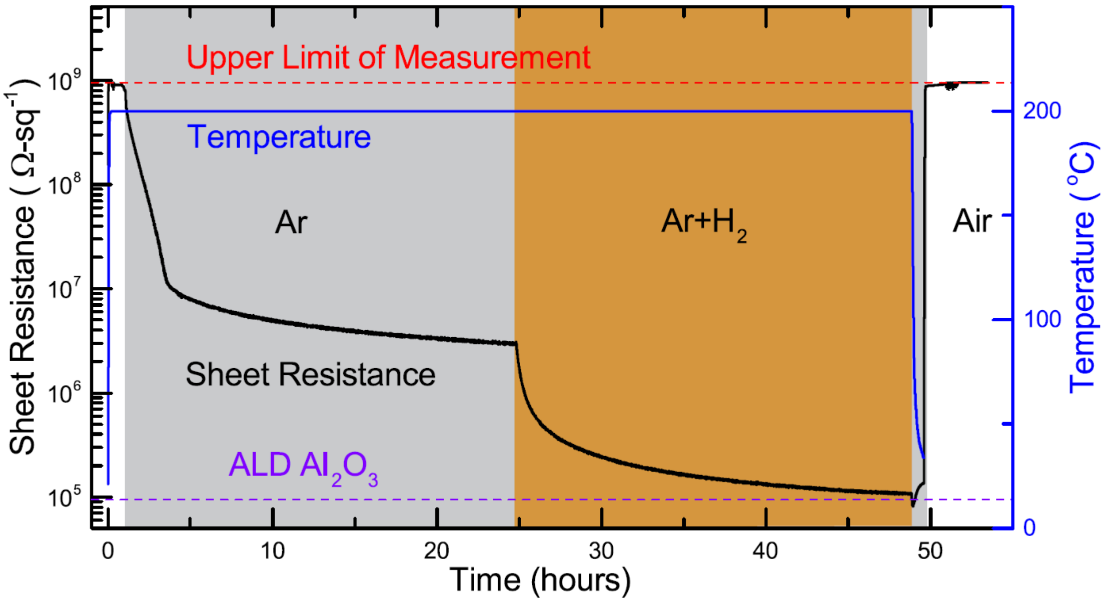

Figure 1.8: Mechanism of alumina ALD improving conductivity is shown by a comparison of ALD-capped films and films exposed to forming gas at moderate temperatures. Reproduced from reference 27.

METHODS

This section is devoted to a detailed explanation of experimental methods and internal tricks that enable this work to be conducted.

NC Synthesis

ITO NCs were synthesized by modification of methods published by the Hutchison group.[32] NCs were synthesized by adding 4.7 mmol of metal precursor (In(III)Acetate$_3$ and Sn(IV)Acetate$_4$) to 10 mL of oleic acid in a round bottom flask. This will be referred to as the precursor flask. The precursor flask is then put under vacuum and heated to 110°C for 1 hour with one pump/purge midway through the hour. The precursor flask is then put under nitrogen and heated to 150°C for 2 hours to generate In- and Sn-oleate. Concurrently, 12 mL of oleyl alcohol is put in a second round bottom flask, called the reaction flask. The reaction flask is put under vacuum and heated to 150°C for 2 hours with one pump/purge midway through. The reaction flask is then heated to 290°C under nitrogen. Once the In- and Sn-oleate reaction has finished, the contents of the precursor flask are pulled into a syringe for slow injection into the reaction flask. The injection rate is set to 0.2 mL/min and the injection volume depends on the desired core size. Following the injection the reaction flask is allowed to stay at 290°C for 20 min before being cooled to room temperature.

After the flask has cooled to below 70°C, there are two routes for washing the NCs dependent on whether the NCs will be shelled or not. If the NCs will not be shelled, the NCs are washed 5 times. In the first wash, 1 vol% oleylamine is added to the NC solution followed by 100 vol% ethanol. The solution is centrifuged at 9000 RPM for 5 min, supernatant is disposed, and the NCs are dispersed in hexane. For all following NC washing steps, when solutions are crashed, ethanol is added until the solution just turns an opaque milky color. In the second and third wash, 1 vol% oleylamine and 1 vol% oleic acid is added to the hexane solution and the solution is crashed with ethanol followed by centrifugation at 7500 RPM for 5 min and NC are dispersed in hexane. In the fourth and fifth wash, the hexane solution is crashed with ethanol and centrifuged at 7500 RPM for 5 min and NCs are dispersed in hexane. Finally, without the addition of ethanol, the solution is centrifuged at 5000 RPM for 5 min and the supernatant is retained. If the NCs will be shelled, the NC cores are washed 3 times. In the first wash, 100 vol% ethanol is added followed by centrifugation at 9000 RPM. NC cores are dispersed in hexane. In the second and third wash, NC cores are crashed using ethanol followed by centrifugation at 7500 RPM for 5 min before dispersion in hexane. Finally, without the addition of ethanol, the solution is centrifuged at 5000 RPM for 5 min and the supernatant is retained.

For shelling, the NC core dispersion in hexane is added to the reaction flask with oleyl alcohol. The reaction flask is put under vacuum with the temperature controller set to 25°C to remove hexane. Once bubbling stops, the synthesis is conducted in an identical manner as the core synthesis with volume of reaction mixture injected dictating shell thickness. These NCs are then washed in accordance with the above paragraph.

NC Film Spincoating

NC film quality is highly dependent on the treatment of substrates and dispersions prior to spincoating. Film substrates, 2x2cm Si or 1.5x1.5cm quartz for this work, were cleaned by submersion in solvent and 30min sonication in the order of chloroform, acetone, isopropanol (IPA), and toluene (if using nonpolar dispersions). The substrates are stored in IPA (polar solvents) or toluene (nonpolar solvents) for 24 hours or more before film deposition. NC films throughout this work were spincoated from a NC dispersion in a mixed solvent of 1:1 hexane:octane. To prepare this solution, ethanol was added to NC dispersions in hexane until the solution turns an opaque milky color and was centrifuged at 7500 RPM for 5 min. The supernatant is then discarded and centrifuge tube is held upside-down for the NCs to dry mildly before they are dispersed in 1:1 hexane:octane to yield a NC loading of 50-60 mg/mL. The NC dispersion rests for 24 hours prior to spincoating.

The procedure of the NC film deposition plays the final role in determining film quality and thickness. NC dispersions were filter using a 0.2 μm syringe filter immediately prior to spincoating films. Each substrate was blow dried with nitrogen immediately before spincoating. 30-45 μL of the NC dispersion were pipetted onto the substrate and the spincoater was started. The spincoating program for all films in this work was the following: 0s ramp to 1000 RPM for 60s followed by 0s ramp to 4000 RPM for 30s. The thickness of the films is NC radius dependent, ranging from 70nm for 5nm diameter NCs to 180nm for 20nm diameter NCs. Films were treated with either a formic acid (Chapter 2) or ammonium hydroxide (Chapter 4) ligand exchange and anneal at 300°C or 200°C, respectively, for an hour.

Atomic Layer Deposition

The atomic layer deposition (ALD) presented throughout this work functions on the propagation of surface hydroxyls. This necessitates a high degree of consistency in sample treatment prior to ALD. Samples that underwent the formic acid ligand exchange and decomposition were stored in air for at least 3 weeks while the samples that underwent the ammonium hydroxide ligand exchange were stored in a vacuum desiccator immediately following the anneal. Each of these conditions result in the full hydroxylation of NC surfaces and yields a consistent substrate for ALD. ALD was conducted in a Cambridge Nanotech Savannah S100 atomic layer deposition chamber.

Alumina ALD procedure – Samples are stabilized at 180°C under flowing nitrogen at 0.5 Torr for 10 min followed by a 0.1s water pulse. Each cycle of alumina ALD consists of a 0.1s pulse of trimethylaluminum (TMA), a 30s purge, a 0.1s pulse of water, and a 30s purge. This procedure yields 0.11nm alumina per cycles.

Indium oxide ALD procedure – The indium precursor, cyclopentadienylindium(I) (indium-cp), tube is heated to 70°C. Samples are stabilized at 180°C under flowing nitrogen at 0.5 Torr for 10 min followed by simultaneous 0.1s water and 0.15s ozone pulses. Each cycle of indium oxide ALD consists of a 5s pulse of indium-cp, a 30s purge, simultaneous 0.1s water and 0.15s ozone pulses, and a 30s purge. This procedure yields 0.15nm indium oxide per cycles.

Solution Spectroscopy of NC Dispersion

When measuring solution spectra of NC dispersions, NC stability is highly important for ensuring measurements represent only a summation of individual particles and prevention of NC deposition. Highly stable NC solutions were prepared in 0.5 mg/mL oleic acid in tetrachloroethylene (TCE). To prepare this solution, ethanol was added to NC dispersions in hexane until the solution turns an opaque milky color and was centrifuged at 7500 RPM for 5 min. The supernatant is then discarded and centrifuge tube is held upside-down for the NCs to dry mildly before they are dispersed in 0.5 mg/mL oleic acid in TCE to yield a 20 mg/mL stock solution. The NC dispersion rests for 24 hours prior to measurement.

The stock solution was centrifuged at 6000 RPM immediately before measurements. Each measurement is conducted by diluting the stock solution into 0.5 mg/mL oleic acid in TCE using mass ratio to determine dilution factor. The liquid cell was rinsed three times with the solution to be measured before being filled. Fourier-transform infrared (FTIR, Bruker) spectroscopy measurements were taken from 450 cm-1 to 6500 cm-1 after a 10 min sample chamber purge under 8 SCCM flowing nitrogen. The sample was transferred to the UV-vis-NIR (Cary, Cary series Agilent) and measurements were taken from 3031 cm-1 to 37000 cm-1. The following dilution was made while this measurement was taking place. Due to limitations of the FTIR source, only data below 5000 cm-1 is trusted. Overlap of FTIR and Cary data between 3500 cm-1 and 4500 cm-1 is ensured and the data series are stitched together during data analysis.

When measuring solution spectra of NC dispersions, NC stability is highly important for ensuring measurements represent only a summation of individual particles and prevention of NC deposition. Highly stable NC solutions were prepared in 0.5 mg/mL oleic acid in tetrachloroethylene (TCE). To prepare this solution, ethanol was added to NC dispersions in hexane until the solution turns an opaque milky color and was centrifuged at 7500 RPM for 5 min. The supernatant is then discarded and centrifuge tube is held upside-down for the NCs to dry mildly before they are dispersed in 0.5 mg/mL oleic acid in TCE to yield a 20 mg/mL stock solution. The NC dispersion rests for 24 hours prior to measurement.

The stock solution was centrifuged at 6000 RPM immediately before measurements. Each measurement is conducted by diluting the stock solution into 0.5 mg/mL oleic acid in TCE using mass ratio to determine dilution factor. The liquid cell was rinsed three times with the solution to be measured before being filled. Fourier-transform infrared (FTIR, Bruker) spectroscopy measurements were taken from 450 cm-1 to 6500 cm-1 after a 10 min sample chamber purge under 8 SCCM flowing nitrogen. The sample was transferred to the UV-vis-NIR (Cary, Cary series Agilent) and measurements were taken from 3031 cm-1 to 37000 cm-1. The following dilution was made while this measurement was taking place. Due to limitations of the FTIR source, only data below 5000 cm-1 is trusted. Overlap of FTIR and Cary data between 3500 cm-1 and 4500 cm-1 is ensured and the data series are stitched together during data analysis.

Conductivity Measurements

Before discussing details of taking conductivity measurements, there are a few important considerations. All electronic measurements in this work were conducted on samples on quartz, as the substrate must be sufficiently insulating and chemically inert such that its effects on conductivity and film properties may be completely ignored. One issue with measuring a spincoated film is thickness variations near the film edge. A uniform film thickness square is scribed in the center of the sample to isolate this measurement area from the edges. Finally, for particularly resistive samples, thin slices of indium wire may be pressed onto the corners of the sample area to improve electronic contact between probes and sample.

Room temperature conductivity measurements were collected on an Ecopia Hall Effect measurement system (HMS-5000) in the 4-point probe Van der Pauw geometry. Four gold spring-clip contacts (A, B, C, D) were placed directly on the corners of a film. The system runs eight measurements: I(AB)_V(CD), -I(AB)_-V(CD), I(BC)_V(DA), -I(BC)_-V(DA), I(CD)_V(AB), -I(CD)_-V(AB), I(DA)_V(BC), -I(DA)_-V(BC) where I(WX) are the current source electrodes and V(YZ) are the voltage measurement electrodes. The measured voltages are plugged into the Van der Pauw (1.12).

$$\sigma^{-1} = \rho = \frac{\pi t_s}{2\ln(2)}\left(\frac{f_1\left(\left(V(CD)\right)-\left(-V(CD)\right)+\left(V(DA)\right)-\left(-V(DA)\right)\right)}{4I} + \frac{f_2\left(\left(V(AB)\right)-\left(-V(AB)\right)+\left(V(BC)\right)-\left(-V(BC)\right)\right)}{4I}\right) \quad (1.12)$$

where t_s is the film thickness, f_1 and f_2 are geometric correction factors, and I is the current used for all measurements. The constants f_i are defined by (1.13) and (1.14).

$$Q_1 = \frac{\left(V(CD)\right)-\left(-V(CD)\right)}{\left(V(DA)\right)-\left(-V(DA)\right)} \; (1.13a)$$

$$Q_1 = \frac{\left(V(AB)\right)-\left(-V(AB)\right)}{\left(V(BC)\right)-\left(-V(BC)\right)} \; (1.13b)$$

$$\frac{Q_i-1}{Q_i+1} = \frac{f_i}{0.693} arc\cosh\left(\frac{exp\left(-\frac{0.693}{f_i}\right)}{2}\right) \quad (1.14)$$

Solving (1.14) for f_i corrects for non-ideal sample geometries (differing from a perfect square). This allows the Van der Pauw geometry to be accurate for any shape sample of uniform thickness.

Temperature dependent conductivity measurements were done on a Quantum Design Physical Properties Measurement System. Rather than simply scribing the measured sample to isolate the center, the sample is broken to a size below 1x1cm. The sample is wired using XX gauge copper wire to indium leads as shown in Figure 1.12. This configuration allows resistance measurements in perpendicular directions, such that the entire sample is characterized. Current was swept from 1 to 10 μA in 3 μA increments was applied through adjacent corners of the sample and the voltage measured on the other two corners. A second measurement is made in the perpendicular direction. The conductance values for the two configurations were then used to compute the sheet conductance numerically using (1.15).

$$\exp(-\pi R_1 t_s \sigma) + \exp(-\pi R_2 t_s \sigma) = 1 \qquad (1.15)$$

where R_i is the resistance in a direction and σ is the film conductivity. Conductivity data is collected between 2K and 300K in both the cooling and warming directions. The conductivity vs T curve was compared with the cool down curve to ensure no time dependence on conductivity. The temperature was held at each temperature set point during the IV sweep.

Ellipsometric Porosimetry Measurements

Spectroscopic ellipsometry data was obtained using a J. A. Woollam M-2000 Spectroscopic Ellipsometer DI from 193 nm to 1690 nm. The J. A. Woollam Environment Cell was used to change the relative partial pressure of toluene while collecting ellipsometry data to monitor changes in film optical constants as the medium dielectric is modulated in a controlled manner. The angle of incident light was fixed at 70° relative to the sample, which corresponds to a normal incidence with respect to the cell window. Optical constants were obtained by fitting spectroscopic ellipsometry data over the spectral range of 400 nm to 1000 nm in CompleteEASE software and approximating the film as a Cauchy oscillator. The Lorentz-Lorentz equation was used to calculate the volume of toluene in film pores as a function of toluene partial pressure, which was fed into an effective medium approximation. Evolution of film optical constants with toluene partial pressure was fit for film porosity.

X-ray diffraction (XRD) measurements

XRD patterns of ITO NC films were collected on a Rigaku Miniflex 600 diffractometer using Cu K_α radiation. Films were identical to those imaged by SEM. NCs were sized using the Debye-Scherrer equation, $t = \frac{\lambda}{\beta\cos(\theta)}$, where t is the NC diameter, λ is the x-ray wavelength (0.15418 nm), β is the full-width at half-max (FWHM) of the XRD peak, and θ is the Bragg angle of the XRD peak. The FWHM is corrected for instrumental broadening by, $\beta = \left(w_{\mathrm{exp}}^2 - w_{ins}^2\right)^{\frac{1}{2}}$, where w_{exp} is the experimental XRD peak FWHM and w_{ins} is the instrumental broadening as measured from the FWHM of LaB_6.

X-ray photoelectron spectroscopy (XPS) measurements

XPS was conducted on Kratos x-ray photoelectron spectrometer – axis ultra DLD using Al K_α x-ray source. Samples were identical to those imaged by SEM. XPS spectra were calibrated to the C 1s peak at 284.8 eV. Analysis was done using CasaXPS software. Near surface dopant concentration was assessed by calculating the ratio of Sn 3d peak area to the total metal peak area.

Scanning electron microscopy (SEM) and scanning transmission electron microscopy (STEM) measurements

SEM and STEM images were taken with a Hitachi S-5500. Samples for STEM measurements were drop cast on copper TEM grids with carbon supports (400 mesh, TedPella). NCs were sized by image analysis (shown below). Samples for top-down and cross-section film SEM were prepared by spin coating ITO NC dispersions in a mixed solvent of 1:1 hexane:octane on undoped silicon substrates and processed as discussed in main text.

Inductively coupled plasma-atomic emission spectroscopy (ICP-AES) measurements

The overall tin dopant concentration and volume fraction of ITO NCs were characterized by ICP-AES on a Varian 720-ES ICP Optical Emission Spectrometer. NCs were digested with neat aqua regia and allowed to rest for 24-48 hr before dilution to 2 vol%. The volume fraction of ITO was calculated from the concentration of In and Sn in the analyte using an assumed stoichiometry of $(In+Sn)_2O_3$ and density of 7140mg/mL.

Chapter 2: Tuning Nanocrystal Surface Depletion by Controlling Dopant Distribution as a Route Toward Enhanced Film Conductivity

This chapter text and figures have been adapted with permission from reference 29, Copyright © 2018, Nano Letters. Written in collaboration with Zachary Robinson, Ankit Agrawal, Stephen Gibbs, Benjamin Greenberg, Sebastien Lounis, Uwe Kortshagen, and Delia Milliron. My contributions include experimental design, synthesis of most samples, characterization (XRD, XPS, optical, STEM, SEM, etc) of all samples, variable temperature conductivity measurements of several samples, variable temperature data analysis, and principle draft author.

Electron conduction through bare metal oxide nanocrystal (NC) films is hindered by surface depletion regions resulting from the presence of surface states. We control the radial dopant distribution in tin-doped indium oxide (ITO) NCs as a means to manipulate the NC depletion width. We find in films of ITO NCs of equal overall dopant concentration that those with dopant-enriched surfaces show decreased depletion width and increased conductivity. Variable temperature conductivity data shows electron localization length increases and associated depletion width decreases monotonically with increased density of dopants near the NC surface. We calculate band profiles for NCs of differing radial dopant distributions and, in agreement with variable temperature conductivity fits, find NCs with dopant-enriched surfaces have narrower depletion widths and longer localization lengths than those with dopant-enriched cores. Following amelioration of NC surface depletion by atomic layer deposition of alumina, all films of equal overall dopant concentration have similar conductivity. Variable temperature conductivity measurements on alumina-capped films indicate all films behave as granular metals. Herein, we conclude that dopant-enriched surfaces decrease the near-surface depletion region, which directly increases the electron localization length and conductivity of NC films.

SPATIALLY LIMITED ELECTRON TRANSPORT

Transparent conductive oxide (TCO) thin films are of fundamental importance in the modern world due to their vast application in optoelectronic devices such as displays, solar cells, and electrochromic windows.[14,16] These applications require high conductivity, which has traditionally been achieved through vacuum deposition of amorphous or crystalline doped metal oxide films.[16] An effort to reduce manufacturing cost by moving away from vacuum deposition has motivated research on using films of colloidal nanocrystals (NCs) as TCO films. However, colloidal NCs are synthesized with long chain organic capping ligands resulting in spatial separations between neighboring NCs that act as tunneling barriers.[17–19] Carrier conduction in these systems occurs through a hopping mechanism, which is described by the Miller-Abraham model (1.5).

$$\sigma \propto Aexp\left(-\frac{2r_{ij}}{a}\right) exp\left(-\frac{E_{ij}}{k_B T}\right) \qquad (1.5)$$

where σ is conductivity, A is a material-dependent constant, r_{ij} is the distance between sites i and j, a is the inverse of the wavefunction decay rate (called the electron localization length), E_{ij} is the energetic barrier encountered moving from site i to j, k_B is the Boltzmann constant, and T is temperature.[7] Inspection of (1.5) leads to two obvious routes to improve NC film conductivity – reducing the distance between sites and lowering the energetic cost of hopping.[33,34]

Many efforts have focused on reducing the distance between NCs to improve electron transport through NC films. Initial work on colloidally synthesized NC films concentrated on exchanging the organic capping ligands used in synthesis with a variety of organic and inorganic ligands of different lengths or bonding arrangements to modify inter-NC charge transfer or hopping.[18–21] However, NC films with any ligands still in place are often too resistive to be suitable for device applications. Various ligand stripping and decomposition reactions have been developed to improve the conductivity of NC films.[19,24] Removal of ligands from NC surfaces often leads to several orders of magnitude increase in conductivity. While this strategy significantly improves film conductivity, removal of ligands exposes NC surfaces to adventitious chemical species, such as water that leads to hydroxylation, forming surface states that are difficult to control and can be harmful to charge transport through NC films.

One method to improve conduction through NC films is to use atomic layer deposition (ALD) to cap bare NC arrays with metal oxides, such as alumina (Al_2O_3).[26–28,35,36] Specifically, Thimsen et al. found that ZnO NC films with alumina capping layers had conductivity eight orders of magnitude higher than that of bare films.[26] This approach was later elaborated upon by Ephraim et al., who explained that the significant film performance improvement following alumina deposition is due to the removal of adsorbed water species by trimethylaluminum, the precursor used during alumina ALD.[27] These studies suggest that adsorbed water species play a direct role in affecting film conductivity but the mechanism by which adsorbed water species actually lead to reduced conductivity remains unexplored.[26,37] Recently, Zandi and Agrawal et. al. reported that electrochemical modulation of optical absorption in tin-doped indium oxide (ITO) NC films can be explained by the formation of a depletion region near NC surfaces.[37] We can therefore hypothesize that the enhanced electron transport in films whose surface hydroxyls have been eliminated is a result of alleviating depletion effects that were present due to the hydroxyl-associated surface states. Here we examine the role that depletion plays in inhibiting charge transport, and we study how the properties of NCs and their surfaces can be tuned to reduce depletion effects and improve transport.

Specifically, we report the influence of the intra-NC dopant distribution on conductivity of ITO NC films. Films comprised of NCs of similar size and overall tin concentration show a marked difference in film conductivity when the radial dopant distribution is manipulated. Bare NC films of a given overall dopant concentration exhibit higher conductivity, larger electron localization length, and lower contact resistance when dopant concentration is high near the NC surface. The dependence of electronic properties on dopant distribution is understood by examining how the intra-NC band profile is altered by dopant segregation in the presence of a depletion region near the NC surface. Following alumina ALD, films display comparable conductivity and contact resistance, independent of NC dopant profile, confirming that depletion-related resistance plays a dominant role in differentiating the electronic behavior of bare NC films of differing intra-NC dopant profiles.

EXPERIMENTAL PROCEDURES

ITO NCs were synthesized using a two-step method adapted from the slow growth methods developed by Jansons et. al.[32] The dopant distribution was controlled by synthesizing ITO NC cores of a desired dopant concentration, which then undergo a washing procedure before reintroduction to a reaction flask for shell growth of desired dopant concentration and shell thickness (Section 1.4). This synthetic method leads to highly controlled core and shell sizes and low size polydispersity. Core and overall particle sizes were measured by Scherrer analysis of the ITO (222) XRD peak and validated by scanning transmission electron microscopy (Figures 2.1, 2.2, 2.3). Dopant incorporation was quantified by elemental analysis using inductively coupled plasma-atomic emission spectroscopy (ICP-AES) for overall Sn dopant concentration and X-ray photoelectron spectroscopy (XPS) with an Al K_α source (1486.7 eV) to assess the near-surface Sn dopant concentration (Figure 2.4). Al K_α source energy corresponds to a photoelectron escape depth of about 1.5 nm.[38]

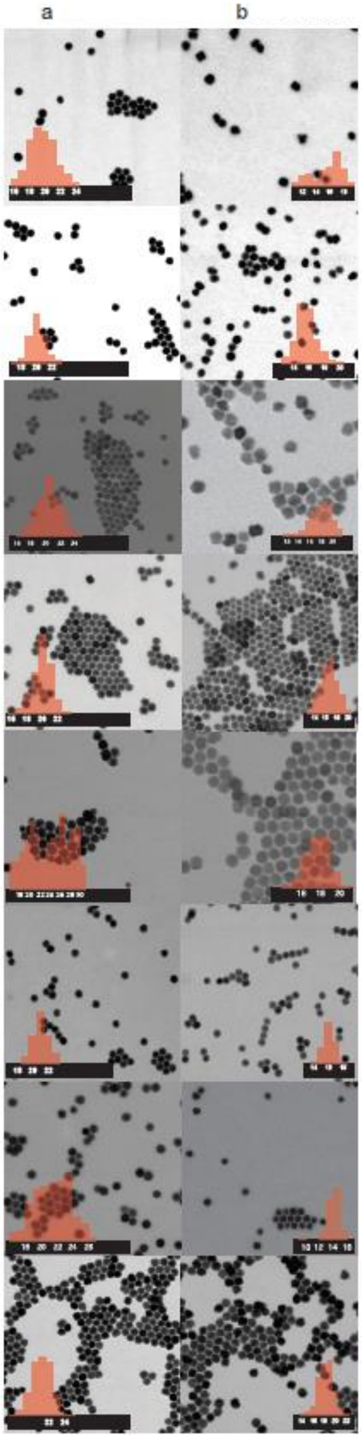

Figure 2.1: Scanning transmission electron microscopy (STEM) images of overall ITO NCs (a) and cores (b) for Core8 (i), Core5 (ii), Core4 (iii), Uniform (iv), Shell4 (v), Shell5 (vi), Shell8A (vii), and Shell8B (viii). Scale bars represent 300nm (a) and 100nm (b).

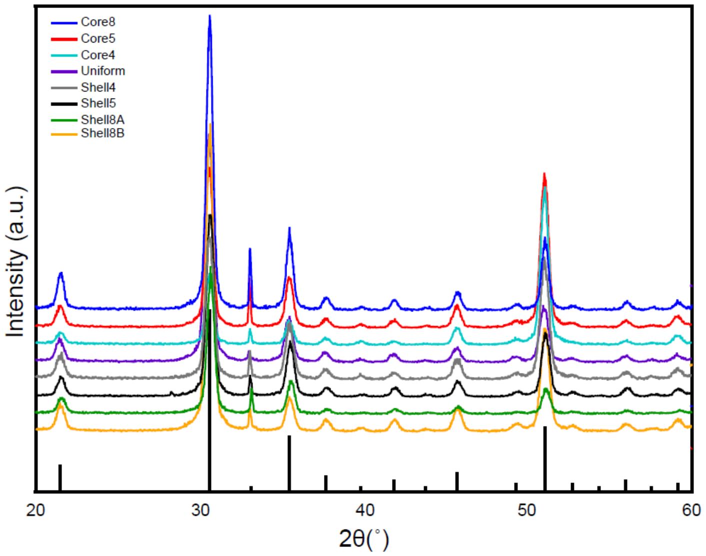

Figure 2.2: Overall ITO NC crystal structure. All samples show agreement with bixbyite ITO reference (sticks shown above along x-axis).

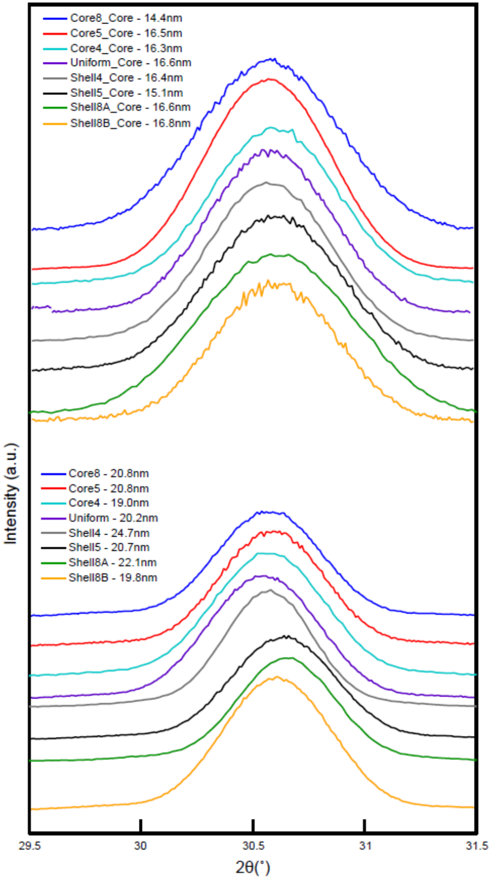

Figure 2.3: (222) XRD peaks of ITO NC cores (a) and overall ITO NCs (b). NC sizes were assessed by Scherrer analysis.

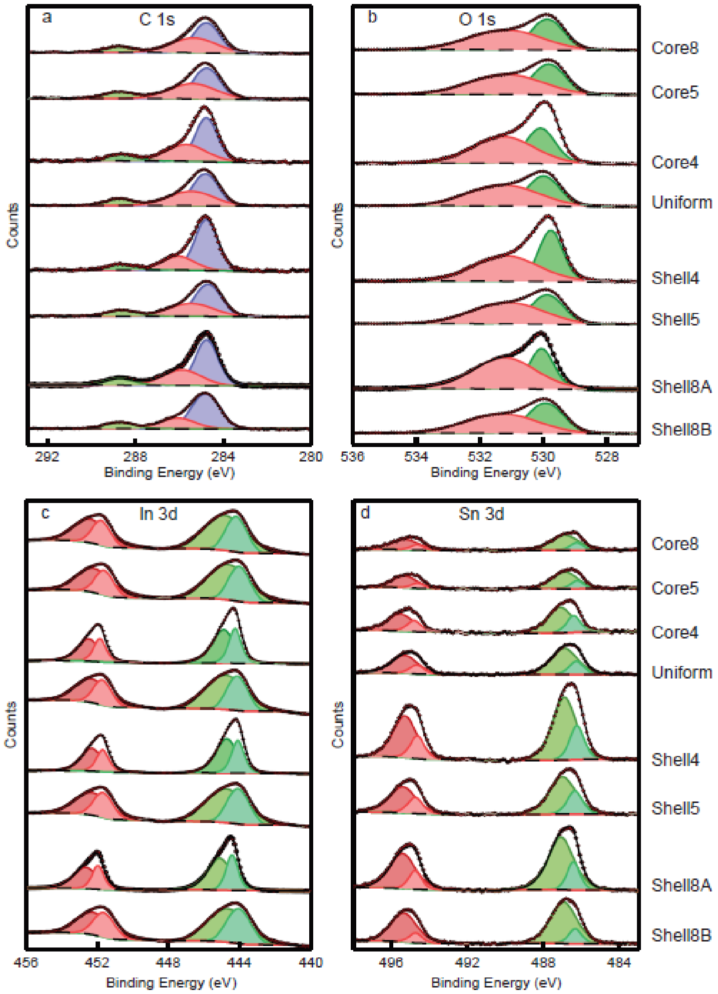

Figure 2.4: X-ray photoelectron spectroscopy (XPS) of C 1s (a), O 1s (b), In 3d (c), and Sn 3d (d) peaks for ITO NC films.

Colloidal NCs were spin-coated from a concentrated dispersion in a mixed solvent of hexane and octane (1:1) onto silicon and quartz substrates, yielding approximately 100 nm thick films. To enhance electron transport, the organic ligands used in colloidal NC synthesis were removed by an *in situ* ligand displacement with formic acid followed by a 60 minute anneal at 300°C in flowing nitrogen gas to decompose and desorb the remaining organic matter.[24] Ligand removal was verified by Fourier-transform infrared spectroscopy (Figure 2.5). The resulting films were highly transparent at visible wavelengths (Figure 2.6). Scanning electron microscopy (SEM) images show densely packed films with direct contact between NCs and minimal cracking (Figure 2.7). Porosity of NC films prepared on silicon substrates was determined using ellipsometric porosimetry (EP) with toluene as the dielectric contrast solvent. EP data from 400 nm to 1000 nm wavelength was fit using software provided by JA Woollam and yielded consistent volume fractions between 0.72 and 0.78 for all films (Figure 2.8).

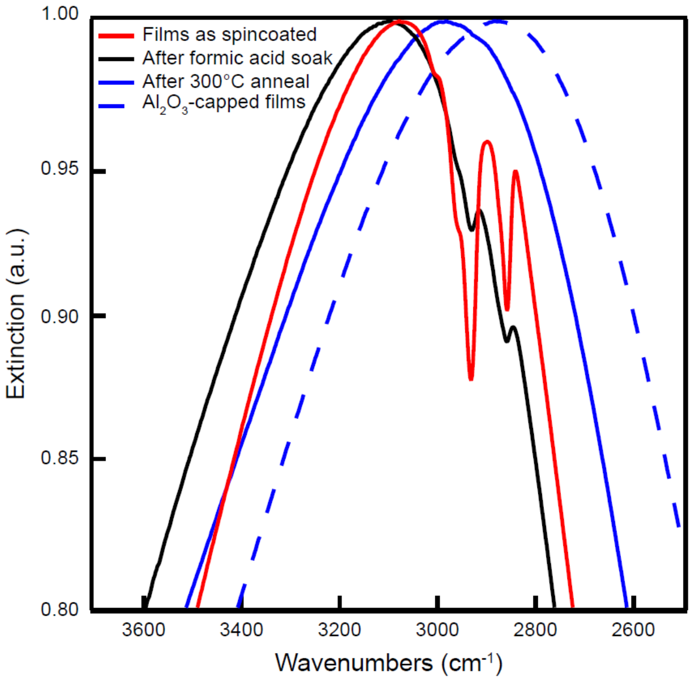

Figure 2.5: Ligand exchange and removal tracked by Fourier-transform infrared (FTIR) spectroscopy. The removal of ligands was verified using FTIR spectroscopy. The native ligands (oleic acid and oleylamine) have long carbon chains which show a strong C-H stretch absorption in the infrared. The C-H stretch absorption can be seen to shrink significantly following the formic acid soak and is removed completely following annealing for 1 hour at 300°C.

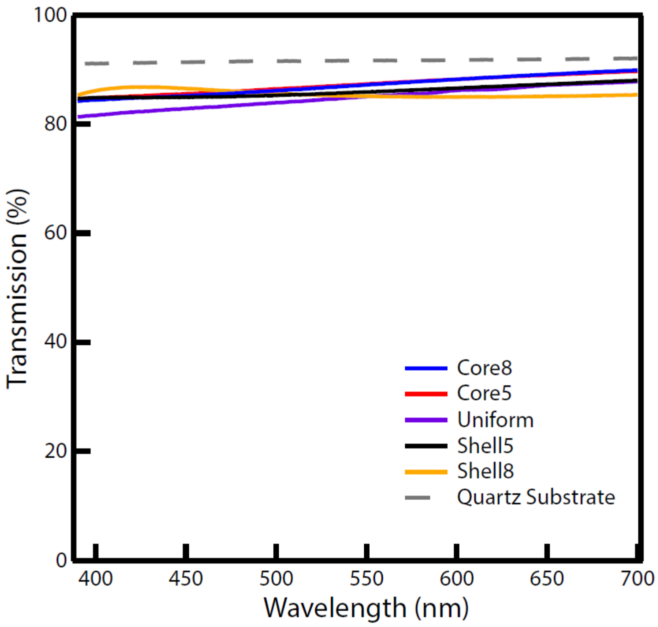

Figure 2.6: Bare ITO NC film optical transparency. All measured films show a wide transparency window across the visible range.

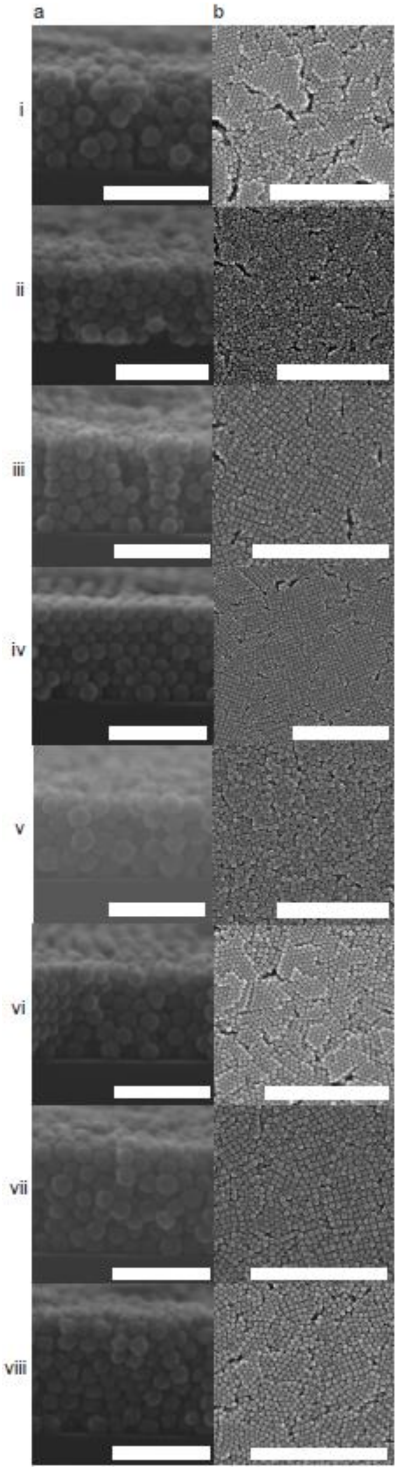

Figure 2.7: Bare NC film on silicon SEM cross-section (a) and top-down (b) for Core8 (i), Core5 (ii), Core4 (iii), Uniform (iv), Shell4 (v), Shell5 (vi), Shell8A (vii) and Shell8B (viii). Scale bars represent 100nm for cross-section and 500nm for top-down.

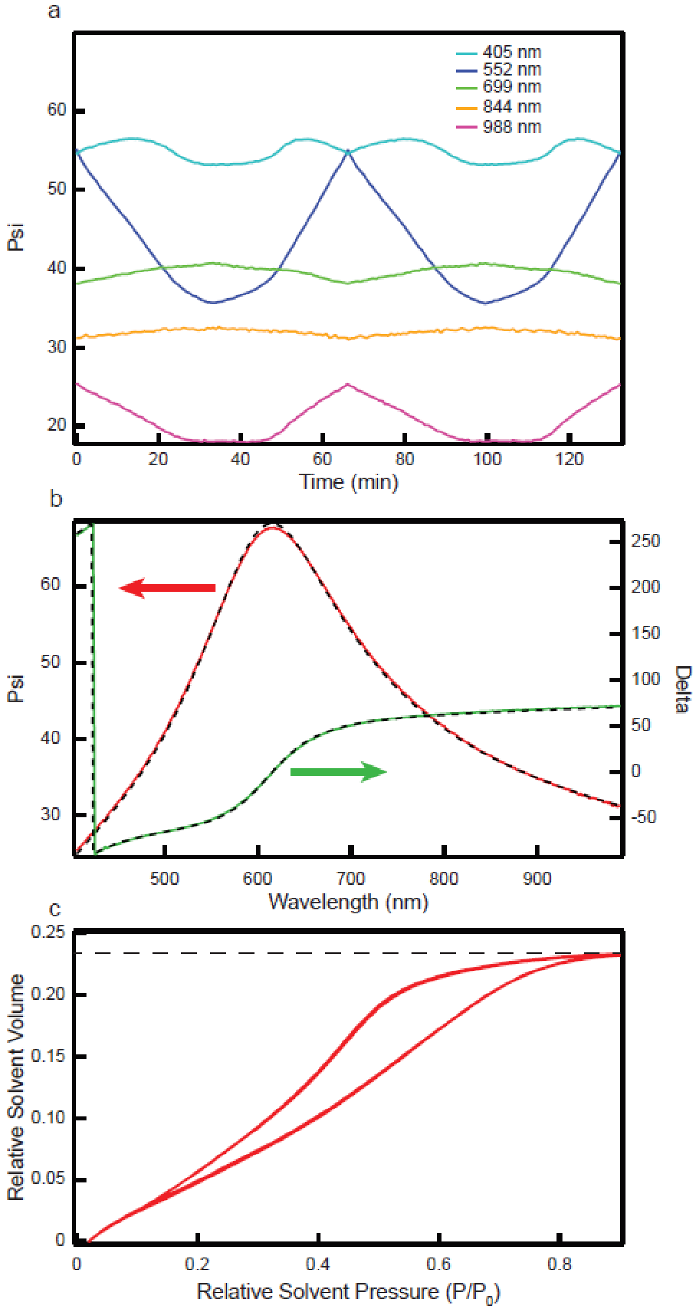

Figure 2.8: Ellipsometric porosimetry (EP) data and analysis of Shell8. EP data was collected from 0.02 to 0.9 relative solvent pressure with toluene as the solvent. Samples were cycled twice to ensure samples were not altered as a result of solvent exposure. Evolution of Psi with time (relative solvent pressure) (a), initial Psi and Delta with fits (dashed line) (b). Relative solvent volume as a function of solvent pressure (c). The maximum relative solvent volume is the sample porosity as shown by the dashed line.

To understand the influence of dopant distribution on film electronic properties when surface depletion is suppressed, bare NC films were capped with 40 ALD cycles of alumina deposition to passivate NC surfaces. Deposition was carried out in a Savannah ALD chamber using previously reported methods.[27] Trimethylaluminum was used as the aluminum precursor and deposition was carried out at 180°C. These conditions correspond to a growth rate of about 0.11 nm per ALD cycle.[26] SEM and time-of-flight secondary ion mass spectrometry (TOF-SIMS) showed 40 cycles of alumina deposition penetrated through the full film thickness and resulted in nearly complete infilling of NC films and deposition of a thin overlayer on the films (Figure 2.9 & 2.10). A similar approach was used by Ephraim et. al., who reported that deposition of alumina on surface segregated ITO NC films by ALD removes adsorbed water species and yields conductive ITO-alumina composites.[27]

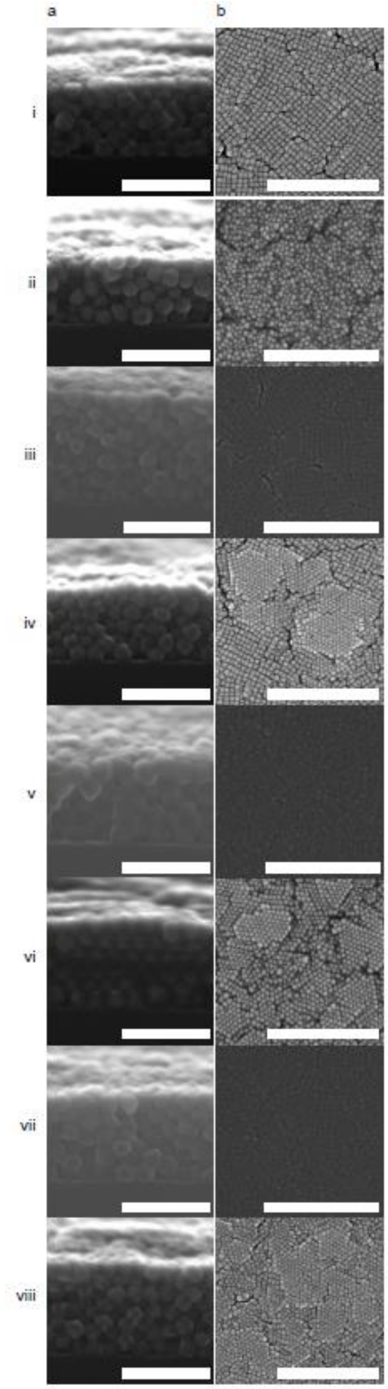

Figure 2.9: Alumina-capped NC film on silicon SEM cross-section (a) and top-down (b) for Core8 (i), Core5 (ii), Core4 (iii) Uniform (iv), Shell4 (v), Shell5 (vi), Shell8A (vii), and Shell8B (viii). Scale bars represent 100nm for cross-section and 500nm for top-down.

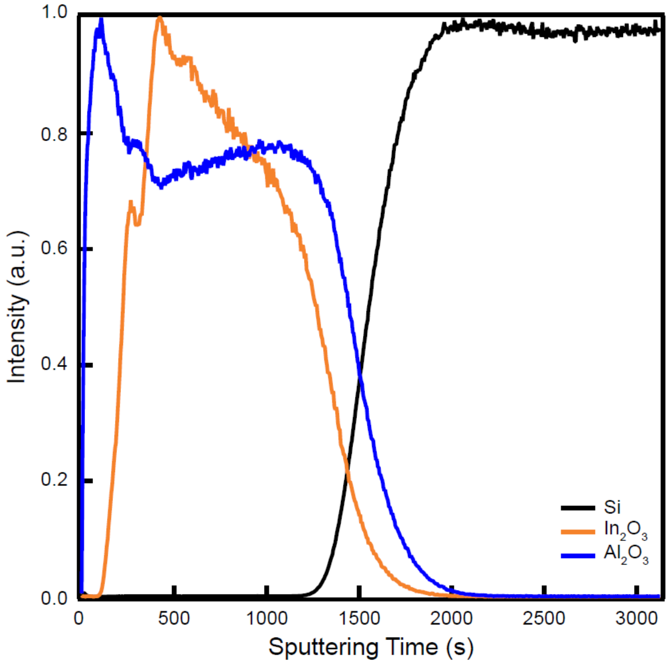

Figure 2.10: Alumina deposition penetration profile. Alumina deposition can be seen to permeate through the full film thickness by time-of-flight secondary ion mass spectrometry (TOF-SIMS). TOF-SIMS shows alumina fully permeates the NC film, as seen by Al_2O_3 tracking well with In_2O_3 as a function of sputtering time up to the onset of the silicon substrate, as well as forming an overlayer on top of the NC film.

To minimize aberrations in data, all analyses were conducted on samples that were exposed to ambient lab air for at least 23 days (Figure 2.11). Room temperature conductivity measurements were collected on an Ecopia Hall Effect measurement system (HMS-5000) in the 4-point probe Van der Pauw geometry. Gold spring-clip contacts were placed directly on the films and edge effects were minimized by isolating a uniform square region in the center of the film using a diamond scribe. Variable temperature conductivity measurements were conducted in a Physical Property Measurement System (PPMS) from as low as 2 K up to 300 K in both decreasing and increasing temperature directions. Ohmic contact was established using indium solder pads. Bare and alumina-capped NC film room temperature conductivity data represents an average over 6 samples and 2 samples, respectively.

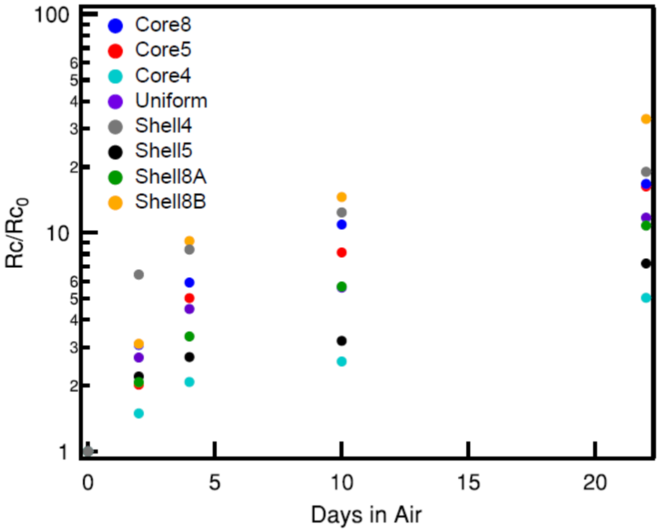

Figure 2.11: Bare ITO NC air sensitivity. The resistivity of bare ITO NC films is highly sensitive to ambient air exposure. The air sensitivity of metal oxide NC film resistivity is attributed to adsorbed water species at the NC surface.[26,27] This can cause otherwise identical films to display significantly different resistivity data due to different air exposure times.

Poisson’s equation was solved numerically for spherical nanocrystals with a given radial dopant profile and surface potential, E_S, using a finite element method. The charge density at any point inside the nanocrystal is made up of mobile electrons and immobile ionized impurity centers. Here, we have shown the potentials used to solve the Poisson’s equation (Figure 2.12). E_F is the Fermi energy level, E_{CB} is the conduction band minima, E_{VB} is the valence band maxima, E_I is the reference potential and center of the band gap.

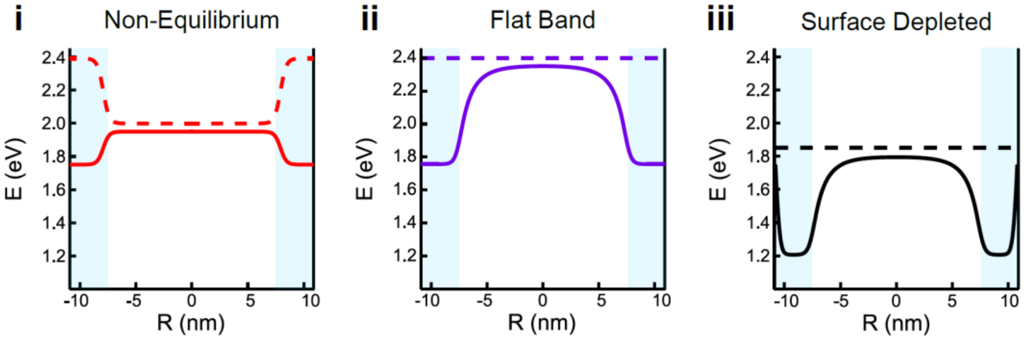

Figure 2.12: Band profile of Core5 under non-equilibrium (i), flat band (ii), and surface depleted (iii) conditions. The non-equilibrium case shows the band profile and Fermi level before the equilibration of the Fermi level. The flat band case shows the core-shell equilibrium band profile with passivated surfaces, i.e. the surface potential is equal to the Fermi level of the shell species). The surface depleted case is the result of imposing a surface potential 0.2 eV below the flat band potential of indium oxide on case (ii).

Here, we adapted the dimensionless form of Poisson's equation derived by Seiwatz and Green[39] to solve numerically for a spherical nanoparticle in Cartesian coordinates as,

$$\nabla^2 u = -\frac{e^2 \rho}{\varepsilon \varepsilon_0 k_B T} \qquad (2.1)$$

The non-dimensional potential is defined as, $u = \frac{E_F - E_I}{k_B T}$, and k_B is the Boltzmann constant and T is temperature. ε_0 is the vacuum permittivity, ε is the static dielectric constant, and ρ is the charge density.

$$\rho = \{\rho_D(r) - \rho_A(r) + p(r) - n(r)\} \qquad (2.2)$$

where, $\rho_D(r)$ is the radially changing donor dopant density, $\rho_A(r)$ is the acceptor dopant density, $p(r)$ is hole density, $n(r)$ is electron density. Here, since we only have aliovalent donor dopants, $\rho_A(r) = 0$.

The free electron concentration in the parabolic conduction band is equal to,

$$n(r) = 4\pi \left(\frac{2 m_e k_B T}{h^2}\right)^{\frac{3}{2}} \left(F_{\frac{1}{2}}\left(u - w_{C,I}(r)\right)\right) \qquad (2.3)$$

where $F_{\frac{1}{2}}(\eta) = \int_0^\infty \frac{x^{\left(\frac{1}{2}\right)} dx}{1+\exp(x-\eta)}$ and $w_{C,I} = \frac{E_{CB}(r) - E_I}{k_B T}$

Similarly, hole concentration in the parabolic valence band is equal to

$$p(r) = 4\pi\left(\frac{2m_h k_B T}{h^2}\right)^{\frac{3}{2}}\left(F_{\frac{1}{2}}\left(w_{V,I}(r) - u\right)\right) \qquad (2.4)$$

where $w_{V,I} = \frac{E_{VB}(r) - E_I}{k_B T}$

If the donor energy level is E_D, the activated dopant concentration can be expressed as,

$$\rho_D(r) = \frac{N_D(r)}{1 + 2\exp\left(u - w_{D,I}\right)} \qquad (2.5)$$

where $w_{D,I} = \frac{E_D(r) - E_I}{k_B T}$

Substituting all the individual terms into (2.1)

$$\nabla^2 u = -\frac{e^2}{\varepsilon\varepsilon_0 k_B T}\left\{\frac{N_D(r)}{1 + 2\exp\left(u - w_{D,I}\right)} + 4\pi\left(\frac{2m_h k_B T}{h^2}\right)^{\frac{3}{2}}\left(F_{\frac{1}{2}}\left(w_{V,I}(r) - u\right)\right) - 4\pi\left(\frac{2m_e k_B T}{h^2}\right)^{\frac{3}{2}}\left(F_{\frac{1}{2}}\left(u - w_{C,I}(r)\right)\right)\right\} \qquad (2.6)$$

with the boundary condition,

$$u = u_{surf} = \frac{E_{surf} - E_I}{k_B T} \qquad (2.7)$$

Poisson's equation (2.6) was solved in COMSOL using a finite element scheme.

BARE NC FILMS

To investigate the role that dopant distribution plays in conductivity of ITO films, it was necessary to synthesize a series of NCs with similar size and overall dopant concentration (two properties that are known to affect conductivity)[40–42] but with variations in the radial profile of dopants. More specifically, thanks to unprecedented size and dopant incorporation control afforded by the synthetic methods advanced by Janson et al,[32] we varied the density of dopants radially within each NC while keeping the overall dopant concentration and NC diameter nearly constant at 3 at% and 20 nm, respectively. The eight samples investigated here are uniformly-doped (Uniform), core-doped with an undoped shell:4 at% core (Core4), 5 at% core (Core5), and 8 at% core (Core8), and shell-doped with an undoped core: 4 at% shell (Shell4), 5 at% shell (Shell5), 8 at% shell (Shell8A), and 8 at% shell at 2.5 at% overall (Shell8B). NC sizes and dopant profile are summarized in Table 2.1: Discrepancies between nominal shell dopant concentration and that measured by XPS may be due to moderate redistribution of Sn during NC synthesis. However, the near-surface Sn concentration observed by XPS is unaffected by the ligand removal and annealing processes (Figure 2.13 and Table 2.2). Despite this, comparing tin content by XPS and ICP-AES shows significant dopant segregation for all core-shell samples and a clear trend of increasing near-surface dopant concentration from Core8 to Shell8A.

Table 2.1: ITO NC core-shell structure.

Sample	Dopant Distribution	Core Diameter (nm)	Overall Diameter (nm)	at% Sn by ICP-AES	at% Sn by XPS
Core8	Core-doped	14.4	20.8	3.3±0.2	2.2
Core5	Core-doped	16.5	20.8	3.1±0.3	2.4
Core4	Core-doped	16.3	19.0	2.7±0.1	2.4
Uniform	Uniform	16.6	20.2	3.0±0.1	3.9
Shell4	Surface-doped	16.4	24.7	3.2±0.1	5.3
Shell5	Surface-doped	15.1	20.7	3.1±0.2	6.5
Shell8A	Surface-doped	16.6	22.1	3.3±0.1	6.8
Shell8B	Surface-doped	16.8	19.8	2.5±0.1	6.3

Core and overall NC sizes by Scherrer analysis, overall tin dopant concentration by ICP-AES and near surface tin dopant concentration by XPS.

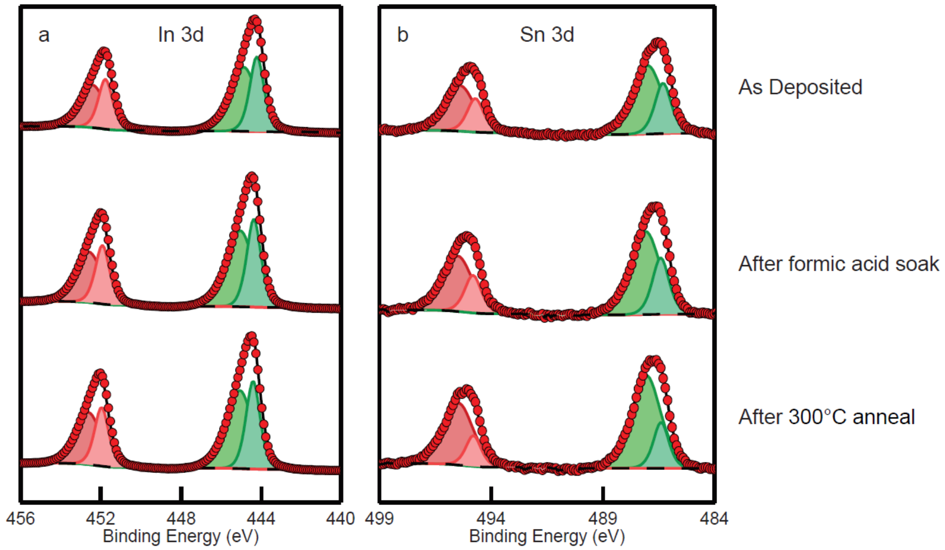

Figure 2.13: Film processing XPS. XPS of In 3d (a) and Sn 3d (b) peaks for a Shell5 NC film as deposited, after 30 minute formic acid soak, and after 1 hour anneal at 300°C.

Table 2.2: Near surface tin density during film processing.

Processing Step	**Near surface tin density (at%)**
As deposited	6.4
After formic acid soak	6.5
After 300°C anneal	6.5

XPS analysis shows no significant redistribution of tin during film processing. Numbers presented are calculated using XPS data shown in Figure 2.12.

We measure conductivity of bare films following prolonged ambient lab air exposure to minimize variations in surface chemistry from sample to sample. Bare film conductivity is shown in Figure 2.14. Conductivity of all samples of equal overall dopant concentration shows an exponential dependence on the near-surface dopant concentration. Core8 and Core5 exhibit the lowest average conductivity of the series at 0.154 S-cm^{-1} and 0.168 S-cm^{-1}, respectively. As dopants are placed closer to the surface, the conductivity more than doubles upon reaching uniform distribution, where the measured conductivity was 0.343 S-cm^{-1}. Finally, Shell5 and Shell8A show the highest conductivity of the series at 0.901 S-cm^{-1} and 1.11 S-cm^{-1}, respectively, representing a nearly nine-time increase from the lowest conductivity sample, Core8. We note that while Shell8B has a high dopant concentration on the surface, it shows a significantly lower conductivity than expected based on the trend observed for the four other samples. One possible explanation for this deviation may be Shell8B having a significantly lower overall dopant concentration. This explanation is supported by Shell8A having an increased overall dopant concentration, with only modest changes to NC size and near surface dopant density, the conductivity increases nearly an order of magnitude and follows the predicted trend. However the material-dependent constant, A, in the Miller-Abraham model and its dependence on dopant concentration are highly uncertain.[6,42–44] We refrain from analyzing the room temperature conductivity of bare films of Shell8B for this reason.

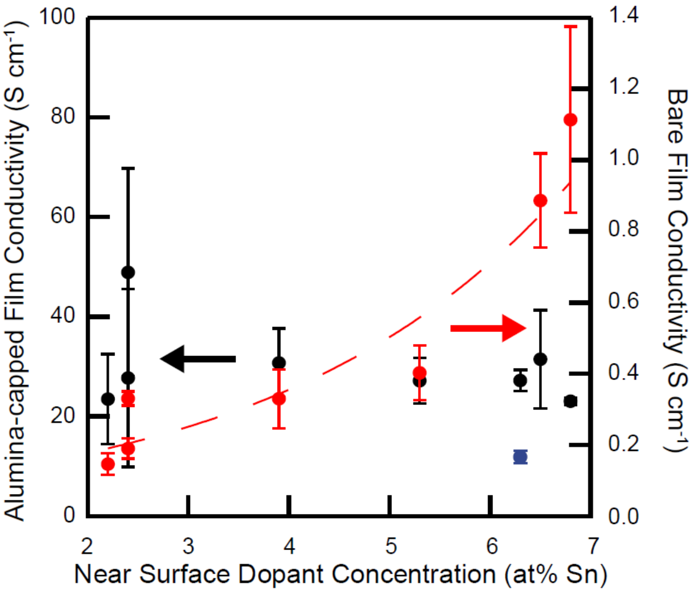

Figure 2.14: Film conductivity. Room temperature conductivity for bare ITO NC films of equal overall dopant concentration shows an exponential dependence on the near surface dopant concentration, as measured by XPS. This dependence is not observed in the room temperature conductivity of alumina-capped ITO NC films. Dashed line shows an exponential fit of bare film conductivity. The blue point represents Shell8B, which was not included in the fit.

Comparing room temperature conductivity of films is useful in determining the optimal material for a device, but gives little insight into the differences in electron transport physics underlying these differences. Analysis of the underlying physics requires films to be viewed as a random resistor network composed of randomly positioned bonds, i.e. conduction pathways, each with a finite resistance, R_{bond}. For NC films with much lower conductivity than their bulk analogue, bond resistance is approximately equal to the contact resistance, R_C, which describes the tunneling resistance between NCs,[16] and is calculated from the links and nodes model in three dimensions as

$$R_C \approx R_{bond} = \frac{(\varphi-\varphi_0)^{1.9}}{2\sigma r_0} \qquad (2.8)$$

where σ is the film conductivity, φ is the NC volume fraction, φ_0 is the percolation threshold, and r_0 is the NC radius.[45,46] We assume the percolation threshold to be that of randomly packed spheres, approximately 0.2.[47] Inter-NC contact resistances are reported in Table 2.3. When R_C is greater than the critical tunneling resistance, which is determined by the ratio of charging energy to the mean energy spacing in a single grain, a material behaves as an insulator and conduction is dominated by a hopping mechanism.[48]

Table 2.3: Localization length and contact resistance.

	Bare			Alumina-capped		
Sample	Simulated Localization Length (nm)	Localization Length (nm)	Contact Resistance (kΩ)	Simulated Localization Length (nm)	Metallic Grain Size (nm)	Contact Resistance (kΩ)
Core8	18.2	18.2±1.2	1206±248	≥ 20.8	25.0±0.4	19.9±0.2
Core5	19.2	18.1±1.1	787±118	≥ 20.8	22.0±0.4	19.2±0.2
Core4	18.3	16.9±1.6	524±98	≥ 19.0	19.4±0.7	14.1±0.2
Uniform	19.8	18.5±1.1	443±111	≥ 20.2	22.1±0.4	20.8±0.1
Shell4	≥ 24.7	35.0±2.8	288±55	≥ 24.7	22.7±0.5	25.3±0.2
Shell5	20.6	21.8±1.9	158±24	≥ 20.7	22.7±0.5	19.8±0.2
Shell8A	≥ 21.5	33.8±2.4	121±28	≥ 21.5	22.8±0.5	21.8±0.3
Shell8B	≥ 19.8	25.1±1.5	1040±106	≥ 19.8	24.9±0.7	24.0±0.3

Bare films: localization length determined by carrier concentration profile simulations, localization length determined by ES-VRH-GD fits, and contact resistance found using the links and nodes model. Alumina-capped films: localization length determined by carrier concentration profile simulations and metallic grain size and contact resistance found by granular metal fits. Fitted parameter error corresponds to a 99.5% confidence interval.

The critical tunneling resistance defines the maximum tunneling resistance for a granular film to exhibit metallic (or granular metal) conduction. If the tunneling resistance between two NCs is greater than the critical tunneling resistance, the film is expected to behave as an insulator and conduction will proceed through a hopping mechanism. The critical tunneling resistance in units of $e^2/\hbar$, where e is the electron charge and $\hbar$ is Planck's constant, is defined by

$$R_{bond}^{C} = \frac{6\pi}{\ln\left(\frac{E_C}{\delta}\right)} \qquad (2.9)$$

Charging energy

$$E_C = \frac{e^2}{2\pi\varepsilon_c\varepsilon_0\alpha} \quad (2.10)$$

where ε_0 is the permittivity of vacuum, and α is the grain diameter

Effective dielectric constant

$$\varepsilon_c = \frac{\pi}{2}\varepsilon_m\left(\frac{2\epsilon}{\pi\varepsilon_m}\right)^{\frac{2}{5}} = 1.99 \qquad (2.11)$$

where ε_m is the dielectric constant of the medium (1 for air) and ϵ is the dielectric constant of the NC (9)

The mean energy spacing in a single grain

$$\delta = \left(g_{E_F}V_{NC}\right)^{-1} \qquad (2.12)$$

where V_{NC} is the NC volume

The density of states at the Fermi level

$$g_{E_F} = \frac{3^{\frac{1}{3}}m_e^{*}n_e^{\frac{1}{3}}}{\hbar^2\pi^{\frac{4}{3}}} \qquad (2.13)$$

where m_e^{*} is the effective mass of an electron ($0.4m_e$ for ITO) and n_e is the electron concentration.

We assume complete dopant activation such that electron concentration is defined by (3E20)*(at% Sn overall) where 3E20 is the density of indium atoms in ITO. Values from these calculations and experimental bond resistance are shown in Table 2.4. R_C is well above the critical tunneling resistance for all NC films indicating that electrons must hop between NCs.

Table 2.4: Critical bond resistance.

Sample	α (nm)	n_e (cm^{-3})	g_{E_F} (J^{-1}m^{-3})	δ (J)	E_C (J)	R_{bond}^{C} (kΩ)	R_{bond}^{Exp} (kΩ)
Core8	20.8	9.90E+20	1.02E+46	2.08E-23	1.11E-20	38.82	1206
Core5	20.8	9.30E+20	1.00E+46	2.12E-23	1.11E-20	38.95	787
Core4	19	8.10E+20	9.57E+45	2.91E-23	1.22E-20	40.41	524
Uniform	19.4	9.00E+20	9.91E+45	2.64E-23	1.19E-20	39.90	443
Shell4	24.7	9.60E+20	1.01E+46	1.25E-23	9.37E-21	36.86	288
Shell5	20.6	9.30E+20	1.00E+46	2.18E-23	1.12E-20	39.07	158
Shell8A	21.5	9.90E+20	1.02E+46	1.88E-23	1.08E-20	38.41	159
Shell8B	19.8	7.50E+20	9.32E+45	2.64E-23	1.17E-20	40.04	1040

α is the grain (NC) diameter, n_e is the electron concentration, g_{E_F} is the density of states at the Fermi level, δ is the mean energy spacing, E_C is the charging energy, R_{bond}^{C} is the critical bond resistance, R_{bond}^{Exp} are calculated bond resistances from experimental values.

In films with no necking between NCs, R_C is primarily defined by a tunneling junction with resistance proportional to $\exp(s\sqrt{2m^*U_0}/\hbar)$ where s is the barrier width, U_0 is barrier height, m^* is the effective mass of an electron (0.4m$_e$ for ITO), and $\hbar$ is Planck's constant.[42] We use the magnitude of R_C as a metric to estimate the tunneling width. The barrier height, equal to the work function at the NC surface, is determined by the surface state energy due to Fermi level pinning and is assumed to be equal for all samples. One should note that this analysis is a simple estimate as the tunneling resistance has a pre-exponential factor that may have a dependence on overall dopant concentration or dopant distribution. However, it is clear from the order of magnitude difference in R_C between Shell8A and Core8 that NC dopant distribution significantly affects the tunneling barrier.

We performed variable temperature conductivity measurements on the bare NC films to gain further insight on how intra-NC dopant profiles influence the inter-NC tunneling junctions (Figure 2.15a). Conductivity increases monotonically with increasing temperature for all films, characteristic of electrons conducting through a hopping mechanism. The temperature dependence of conductivity in an electron hopping regime is described by

$$\sigma(T) = \sigma_0 * \exp\left(-\left(\frac{T_0}{T}\right)^m\right) \quad (2.14)$$

where σ_0 is treated as a material-dependent constant, T_0 is a characteristic temperature, and m depends on the specific hopping mechanism.[6] Zabrodskii analysis indicates m values of nearly 0.78 for all bare samples we measured (Figure 2.16).[49] Atypical values of m (those other than 0.25, 0.5, or 1) were investigated by Houtepen et. al. and were explained by thermal broadening of energy levels within the density-of-states.[50] This broadening depends on the temperature dependence of heat capacity for the active material. While Houtepen et. al. assumed a constant heat capacity and found an m-value of 0.66, we used a power law fit to the ITO heat capacity ($C_p \propto CT^p$) to capture this temperature dependence in the model. Starting from the general form (2.15).

$$g(E) = g_0 \exp\left(-\frac{(E-E_0)^2}{2k_B T^2 C_V(T)}\right) \quad (2.15)$$

A materials heat capacity is temperature dependent for temperatures below its Debye temperature, θ_D, (for ITO, θ_D=1000K)[51]. If the heat capacity of approximated as a power-law in temperature where Cp=C*T^p, the tunneling rate is given by (2.16).

$$\Gamma \propto \exp\left(-\frac{2R}{a} - \frac{\Delta E^2(1+p)}{4k_B T^{p+2} C}\right) \quad (2.17)$$

where ΔE is the energetic barrier to hopping, a is the electron localization length, and R is the hopping distance, given by (2.18).

$$R = \frac{A}{\Delta E^n} \quad (2.18)$$

where A and n are constants that depend on the hopping mechanism. By plugging (2.18) into (2.17) and maximizing Γ with respect to ΔE, we find the most optimal energetic barrier (2.19) and hopping distance (2.20) as a function of temperature.

$$\Delta E_{opt} = \left(\frac{4AnCk_B T^{2+p}}{a(1+p)}\right)^{\frac{1}{2+n}} \quad (2.19)$$

$$R_{opt} = A\left(\frac{a(1+p)}{4AnCk_B T^{2+p}}\right)^{\frac{n}{2+n}} \quad (2.20)$$

Plugging (2.19) & (2.20) into (2.17) yields the general expression for hopping in systems with a Gaussian broadening of energy levels (2.21).

$$\mathit{\Gamma} \propto \exp\left(-\left(\frac{(1+p)^n A^2 (2+n)^{2+n}}{a^2 4^n k_B^n C^n n^n T^{pn+2n}}\right)^{\frac{1}{2+n}}\right) \qquad (2.21)$$

For $\left(n = 1 \,\&\, A = \frac{e^2}{4\pi\varepsilon\varepsilon_0}\right)$ and p = 0.34 (Figure 2.17), Efros-Shklovskii variable-range hopping with a Gaussian dispersion of energy levels (ES-VRH-GD) to have an m value of 0.78. The ES-VRH-GD characteristic temperature in this regime is then defined as

$$T_0 = \left(\frac{3.15e^4}{4\pi^2\varepsilon^2 k_B C a^2}\right)^{\frac{1}{3}} \qquad (2.22)$$

where $C \approx 27$ is the heat capacity power-law coefficient for ITO, e is the electron charge, ε is the dielectric constant of the film, and a is the electron localization length. The film effective dielectric constant was calculated using methods developed by Reich and Shklovskii.[52] Here, the electron localization length defines the diameter of a sphere within which mobile electrons are confined at 0K. Fits to variable temperature data and the corresponding localization lengths are reported in Figure 2.15b and Table 2.3, respectively. Fitting error is reported in Table 2.5.

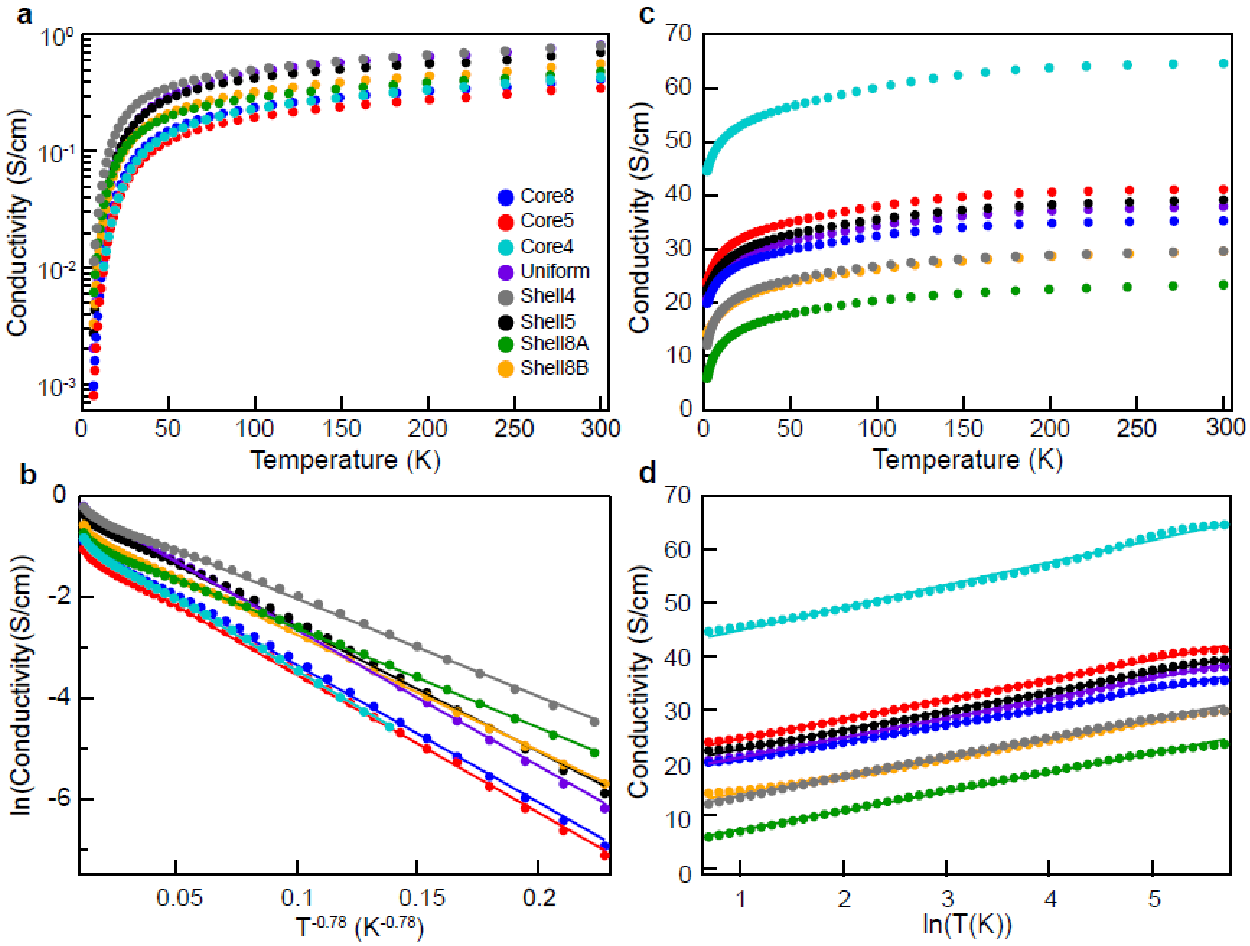

Figure 2.15: Temperature dependence of electron transport in bare (a, b) and alumina-capped (c, d) ITO NC films. Conductivity v. Temperature (a) and Efros-Shklovskii variable range hopping with a Gaussian dispersion of energy levels fit for bare ITO NC films (b). Conductivity v. Temperature (c) and granular metal conduction mechanism for alumina-capped ITO NC films (d). Markers indicate experimental data and lines show fits to ES-VRH-GD (b) and the granular metal (d) conduction mechanisms.

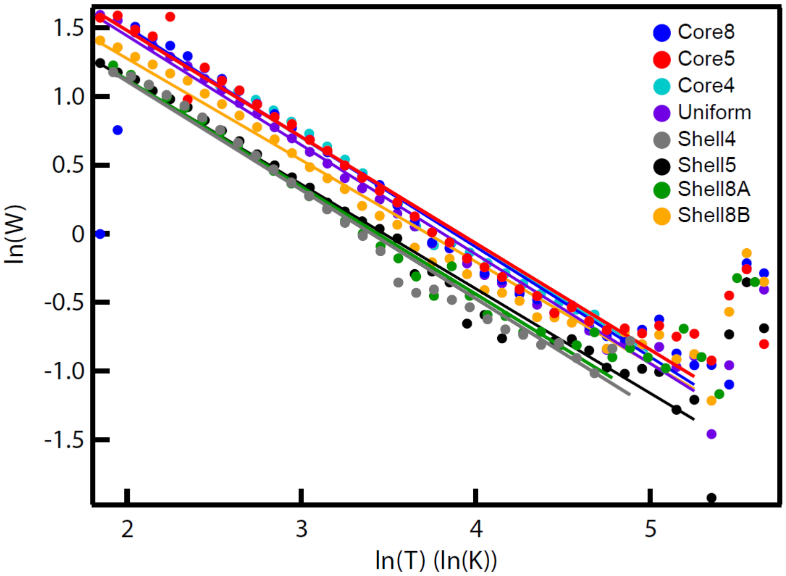

Figure 2.16: Zabrodskii analysis shows slopes near 0.78 for all samples measured. Exact values found are 0.78 (Core8), 0.78 (Core5), 0.78 (Core4), 0.78 (Uniform), 0.79 (Shell4), 0.75 (Shell5), 0.78 (Shell8A), and 0.70 (Shell8B). This indicates a temperature dependence of $\sigma \propto \exp(-T^{-0.78})$.[49]

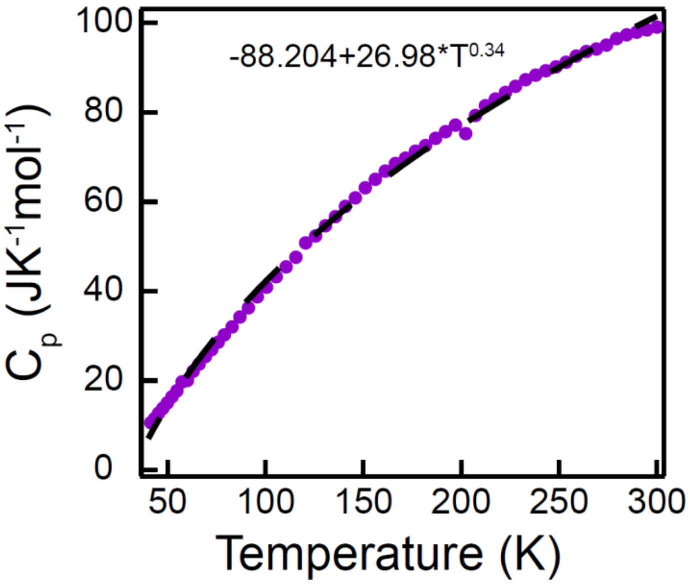

Figure 2.17: ITO heat capacity. Markers indicate data taken from Ref 6 and dashed line shows a power-law fit from ~40K to ~300K.[53]

Variable temperature conductivity data was fit using a 99.5% confidence interval to determine error in calculated values. Error propagation was calculated in following manner.

For a functional form $A = \exp(B)$ the mean value of A, μ_A, and the standard deviation of A, σ_A, can be calculated by:

$$\mu_A = \exp(\mu_B) \qquad (2.23a)$$

$$\sigma_A = |\mu_A * \sigma_B| \qquad (2.23b)$$

For a functional form $A = xB^b$

$$\mu_A = x * (\mu_B)^b \qquad (2.24a)$$

$$\sigma_A = \left|\mu_A * b * \left(\frac{\sigma_B}{\mu_B}\right)\right| \qquad (2.24b)$$

Table 2.5: Bare film variable temperature conductivity fitting error.

Sample	**σ_0 (S/cm)**	**T_0 (K)**	**a (nm)**
Core8	0.53 ± 0.02	68.9 ± 1.5	18.2 ± 1.2
Core5	0.44 ± 0.02	69.1 ± 1.4	18.1 ± 1.1
Core4	0.53 ± 0.02	72.4 ± 2.2	16.9 ± 1.6
Uniform	0.96 ± 0.04	68.1 ± 1.4	18.5 ± 1.1
Shell4	0.90 ± 0.03	44.5 ± 1.2	35.0 ± 2.8
Shell5	0.89 ± 0.05	61.0 ± 1.7	21.8 ± 1.9
Shell8A	0.52 ± 0.02	45.5 ± 1.1	33.8 ± 2.4
Shell8B	0.64 ± 0.02	55.5 ± 1.1	25.1 ± 1.5

The mean and standard deviation for σ_0 was calculated using (2.23a,b) from fitted values of $ln(\sigma_0)$. The mean and standard deviation for T_0 was calculated using (2.24a,b) from fitted values of $T_0^{0.78}$. The mean and standard deviation for a was calculated using (2.24a,b) from fitted values of T_0.

ES-VRH-GD fits to variable temperature conductivity data indicate the electron localization length increases as dopants move toward the surface. Core8 NC films exhibit a localization length nearly 3 nm smaller than the NC diameter while Shell4, Shell8A, and Shell8B show some degree of delocalization of electrons beyond the size of the NCs. The monotonic growth of localization length with increasing overall dopant concentration has been established as a signature of approaching the metal-insulator-transition in NC films.[36,42,45] Interestingly, despite having the lowest overall dopant concentration, Shell8B shows a longer localization length than the core-doped and uniformly doped samples measured here. Previously, studies of the connection between localization and dopant concentration considered only films of uniformly doped NCs and those with passivated surfaces. Here we reveal that the more relevant property for bare NC films is the concentration of dopants in the near surface region. This is because greater (lesser) dopant density at the surface reduces (increases) the effects of surface depletion. Thus, films of low overall dopant concentration NCs can be engineered to produce a large localization length by controlling the dopant distribution.

To further understand the trend of localization length with changing dopant distribution, we simulated the band profiles within isolated ITO NCs with radially controlled dopant distribution in the presence of surface states that are approximated to be 0.2 eV below the conduction band minimum of indium oxide (Figure 2.18). The trends are qualitatively accurate throughout a range of surface state energies (Figure 2.19).[37] In uniformly-doped ITO NCs (Figure 2.18ci), the band profile is easily understood as a radial depletion region near the NC surface. When dopants are segregated, the band profile becomes significantly more complex. Tin dopants decrease the electronic band gap of indium oxide while also increasing the optical band gap due to state filling, i.e. the Burstein-Moss effect.[54,55] This means that in addition to band bending at the surface, band bending will occur near the interface of doped and undoped regions within the NC. In core-doped ITO NCs (Figure 2.18a,bi), a relatively low density of charged defects near the surface results in a wide depletion region that extends to the doped core. In contrast, surface-doped ITO NCs (Figure 2.18d,ei) have a high density of charged defects near the surface, resulting in a sharper, narrower depletion region, which we have correlated with an expanded localization length in films fabricated from these NCs.

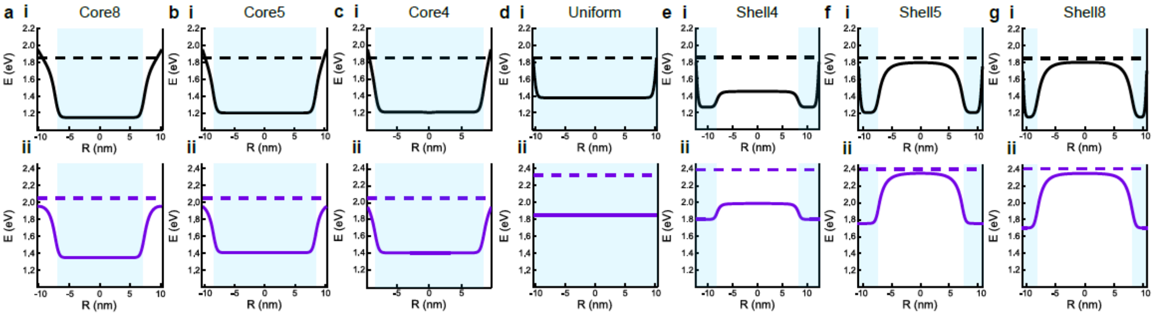

Figure 2.18: Simulated band profiles. Intra-NC band profile for Core8 (a), Core5 (b), Core4 (c), Uniform (d), Shell4 (e), Shell5 (f), and Shell8 (g) with a surface potential 0.2 eV below the flat band potential of indium oxide (a-e i) and equal to the flat band potential of the shell species (a-e ii). The latter represents the absence of surface-state induced depletion. In all cases, the horizontal dashed line is the Fermi level and the blue shaded region indicates the region of enriched dopants. R = 0 denotes the center of a NC and maximum |R| denotes the surface.

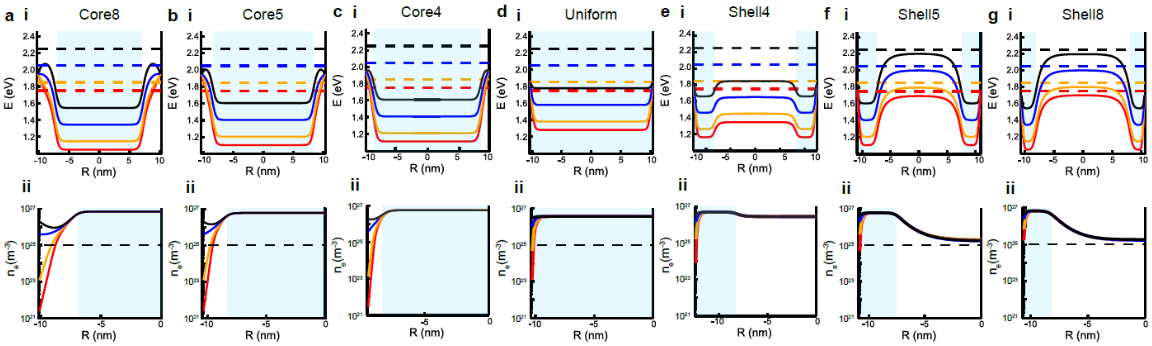

Figure 2.19: Band profiles under various surface potentials. Intra-NC band (i) and radial electron concentration (ii) profiles for Core8 (a), Core5 (b), Core4 (c), Uniform (d), Shell4 (e), Shell5 (f), and Shell8 (g) with a surface potential 0.3 eV below (red), 0.2 eV below (orange), 0 eV above (blue), 0.2 eV above (black) the flat band potential of indium oxide. The horizontal dashed line is the Fermi level (i) or critical carrier concentration (ii). In all cases, the blue shaded region indicates the region of enriched dopants. R = 0 denotes the center of a NC and maximum |R| denotes the surface. For all simulations showing a surface state below the flat band potential of indium oxide the absolute surface state energy does not change the qualitative interpretation of the data. This range of surface state energy is consistent with literature values of surface hydroxyls, ranging from 0.1 to 1 eV below the indium oxide conduction band minimum.[26,37]

We simulated electron concentration profiles to visualize how these band profiles influence the electron localization length for each dopant distribution in a NC-NC tunneling junction (Figure 2.20a-e). The electron localization length is defined here as the diameter of a sphere containing all space with an electron concentration of greater than

10^{25} m^{-3}, the critical electron concentration for metallic behavior in ITO according to the Mott criterion.[3] Using this definition, we examine the electron localization compression due to depletion, which is simply the difference between the physical diameter of the NC and the electron localization length. As shown in Figure 2.20a,b,c, the extended surface depletion region in core-doped samples leads to significant localization length shrinkage in Core8, Core5, Core4 of 2.6 nm, 1.6 nm, and 0.7 nm, respectively. For uniform dopant distribution (Figure 2.20d), the localization length is compressed only slightly, about 0.4 nm. Finally, when the majority of dopants are near the surface (Figure 2.20e,f,g), the localization volume is approximately the size of the NC with Shell5 having 0.1 nm compression and Shell4 and Shell8 being fully delocalized within the NC. Shell4 achieves full delocalization while Shell5 does not due to the larger diameter of Shell4. The definition of electron localization length in our simulations is simplified by ignoring wavefunction decay beyond the metallic region of the NC. Despite this, the trend observed in simulations is mirrored in localization lengths determined by analysis of variable temperature conductivity data (Table 2.3). Without considering wavefunction decay beyond the physical NC dimensions our simulation cannot describe electron localization lengths greater than the NC diameter; however, the simulated intra-NC electron concentration profiles for Shell4 and Shell8 agree with the possibility for electron delocalization outside of the NC, as suggested by the experimental variable temperature conductivity data.

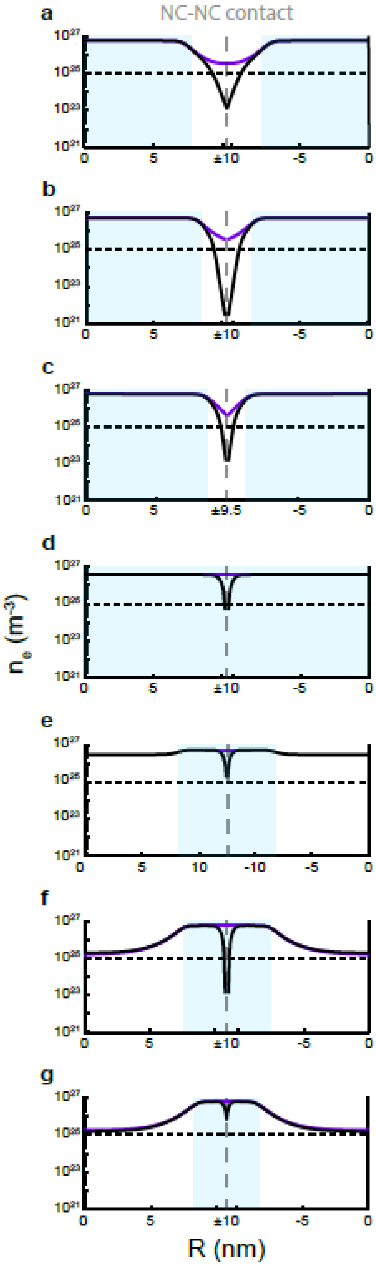

Figure 2.20: Simulated electron concentration profiles. Radial electron concentration profile for Core8 (a), Core5 (b), Core4 (c), Uniform (d), Shell4 (e), Shell5 (f), and Shell8 (g) with a surface potential 0.2 eV below the flat band potential of indium oxide (Black) and equal to the flat band potential of the shell species (Purple). Vertical dashed line is where neighboring NCs touch and horizontal dashed line is the critical carrier concentration. In all cases, the blue shaded region indicates the region of enriched dopants. R = 0 denotes the center of a NC and maximum |R| denotes the surface.

The importance of the localization length and its magnitude relative to the NC size is apparent as we return to analyze the limiting factors in achieving high conductivity NC films. The contact resistance, analyzed as a tunneling junction, is $R_C \propto \exp\left(s\sqrt{2m^*U_0}/\hbar\right)$. Again, s defines the separation between the edges of electron localization volumes. Using a simple model of two NCs in contact at a point, and electronically connected by a tunnel junction due to depletion, s is simply the electron localization compression discussed above (Figure 2.20). From our analysis, as the dopant profile moves toward the surface, there is monotonic decrease in s. This diminished barrier width implies a decrease in contact resistance, in agreement with experimental results for Core8 through Shell8A.

ALUMINA-CAPPED FILMS

Following alumina deposition, the conductivity of all films increased significantly as shown in Figure 2.14. All capped-NC films exhibit nearly identical conductivity. We performed variable temperature conductivity measurements on NC films after alumina capping to gain insight on electron transport barriers (Figure 2.15c). While conductivity of alumina-capped films increases monotonically with increasing temperature for all films, conductivity is consistent with a logarithmic dependence on temperature. Conduction of this type has been observed in granular ITO thin films and is ascribed to a granular metal conduction mechanism.[51,56,57] We note that while hopping conduction is a description of electrons overcoming a Coulombic blockage by undergoing hops of thermally varying distances, the granular metal conduction model describes the competition between Coulombic barriers and NC-NC coupling. Granular metal conduction depends on the grain (NC) size and the degree of coupling, reflected in tunneling conductance between neighboring NCs, rather than the electron localization length. The temperature dependence of conductivity in granular metals is described by

$$\sigma = \sigma_0 \left(1 + \frac{1}{2\pi g_T d} \ln\left(\frac{k_B T}{g_T E_C}\right)\right) \qquad (2.25)$$

where $\sigma_0 = g_T \left(\frac{2e^2}{\hbar}\right) \alpha^{2-d}$, g_T is the non-dimensional tunneling conductance between grains, α is the grain diameter, d is the system dimensionality, and $E_C = \frac{e^2}{2\pi\varepsilon\alpha}$ is the charging energy of a grain.[48,56] Metallic grain size and tunneling conductance were calculated from the slope and intercept, respectively, of σ vs $\ln(\mathrm{T})$ as shown in Figure 2.15d. Metallic grain size and tunneling conductance are reported in Table 2.3. Fitting constants and error are reported in Table 2.6.

Table 2.6: Alumina-capped film variable temperature conductivity fitting error.

Sample	A (S/cm*ln(K))	R_C (kΩ)	B (S/cm/ln(K))	α (nm)
Core8	17.2 ± 0.2	20.0 ± 0.2	3.28 ± 0.06	25.0 ± 0.4
Core5	20.6 ± 0.2	19.2 ± 0.1	3.72 ± 0.07	22.0 ± 0.4
Core4	40.6 ± 0.5	14.1 ± 0.2	4.22 ± 0.14	19.4 ± 0.7
Uniform	17.2 ± 0.2	20.8 ± 0.1	3.71 ± 0.06	22.1 ± 0.4
Shell4	10.0 ± 0.3	25.2 ± 0.2	3.61 ± 0.08	22.7 ± 0.5
Shell5	18.8 ± 0.3	19.8 ± 0.2	3.61 ± 0.08	22.7 ± 0.5
Shell8A	3.7 ± 0.3	31.8 ± 0.3	3.6 ± 0.1	22.8 ± 0.5
Shell8B	10.9 ± 0.3	24.0 ± 0.3	3.30 ± 0.09	24.9 ± 0.7

The mean and standard deviation for α was calculated using S14a,b from fitted values of B. The mean of R_C was solved for numerical from fitted values of A and calculated values of α. The standard deviation of R_C was then determined by solving for R_C using each permutation of A and α mean values and plus/minus their standard deviations and then taking the standard deviation of those 9 values.

There are three criteria for the granular metal conduction model to be valid:[56,58]

1. The intra-grain conductance is greater than the tunneling conductance ($g_0 \gg g_T$)
2. The tunneling conductance is greater than the critical tunneling conductance ($g_T > g_T^C$)
3. Must be in the high temperature limit to ignore quantum effects ($T > g_T\delta$)

Each of these criterion is addressed following equations presented by Beloborodov *et. al.*[56]

1. $g_0 > g_T$

The intra-grain conductance in units of $e^2/\hbar$ is defined by

$$g_0 = \frac{E_{Th}}{\delta} \qquad (2.26)$$

Thouless energy

$$E_{Th} = \frac{4\hbar D_0}{\alpha^2} \qquad (2.27)$$

Classical diffusion coefficient

$$D_0 = \frac{v_F^2 \tau}{d} \qquad (2.28)$$

where d is grain dimensionality (3 here)

Fermi velocity

$$v_F = \frac{\hbar}{m_e^*}(3\pi^2 n_e)^{\frac{1}{3}} \qquad (2.29)$$

Taking the mean free path of an electron to be approximately the diameter of a single grain,

$$\tau = \frac{\alpha}{v_F} \qquad (2.30)$$

Plugging (2.30) into (2.28),

$$D_0 = \frac{v_F \alpha}{d} \qquad (2.31)$$

Values from these calculations and tunneling conductance are shown in Table 2.7.

Table 2.7: Intra-NC and tunneling conductance.

Sample	v_F (m/s)	D_0 (m^2/s)	E_{Th} (J)	g_0 $(e^2/\hbar)$	g_T $(e^2/\hbar)$
Core8	8.93E+05	6.19E-03	3.81E-20	1837	0.651
Core5	8.74E+05	6.06E-03	3.73E-20	1762	0.676
Core4	8.35E+05	5.29E-03	3.90E-20	1341	0.915
Uniform	8.65E+05	5.59E-03	3.96E-20	1500	0.623
Shell4	8.84E+05	7.27E-03	3.18E-20	2538	0.512
Shell5	8.74E+05	6.00E-03	3.77E-20	1729	0.654
Shell8A	8.93E+05	6.40E-03	3.69E-20	1963	0.407
Shell8B	8.14E+05	5.37E-03	3.65E-20	1384	0.539

v_F is the Fermi velocity, D_0 is the classical diffusion coefficient for electrons, E_{Th} is the Thouless energy, g_0 is the intra-NC conductance, and g_T is the tunneling conductance from the granular metal fit.

Tunneling conductance is much lower than intra-grain conductance for all measured samples. This criteria shows that tunneling between grains in the rate limiting step in electron conduction through these films.

2. $(g_T > g_T^C)$

The critical tunneling conductance in units of $e^2/\hbar$ is defined by

$$g_T^C = \frac{\ln\left(\frac{E_C}{\delta}\right)}{6\pi} = \frac{1}{R_{bond}^C}$$

Using (2.9) – (2.13) with $\varepsilon_m = 9$ for alumina, g_T^C and g_T are shown in Table 2.8.

Table 2.8: Critical and experimental tunneling conductance.

Sample	g_T^C $(e^2/\hbar)$	g_T $(e^2/\hbar)$
Core8	0.265	0.651
Core5	0.264	0.676
Core4	0.252	0.915
Uniform	0.256	0.623
Shell4	0.283	0.512
Shell5	0.263	0.654
Shell8A	0.268	0.407
Shell8B	0.255	0.539

g_T^C is the critical tunneling conductance and g_T is the tunneling conductance from the granular metal fit.

All samples measured show tunneling conductance well above the critical tunneling conductance. The critical tunneling conductance defines the criterion for a material to behave as a metal.

3. $(T > g_T\delta)$

Using equations (2.12) and (2.13) as well as experimental g_T, $g_T\delta$ is shown in Table 2.9.

Table 2.9: Quantum temperature upper limit.

Sample	$g_T\delta$ (K)
Core8	0.978243503
Core5	1.037151399
Core4	1.929305428
Uniform	1.19146053
Shell4	0.464919533
Shell5	1.033654454
Shell8A	0.553859376
Shell8B	1.030478677

Temperature $g_T\delta$ defines the temperature above which quantum effects no longer significantly influence electron physics in a material. All fits in this work were done at or above 2K. Therefore, we do not expect significant quantum effects.

The grain size in ITO NC films with alumina capping does not show a clear dependence on dopant distribution as localization length did in bare films, but rather becomes approximately equal to the NC diameter for all samples based on granular metal fits of variable temperature conductivity data. Simulated band profiles for passivated surface ITO NCs (Figure 2.19a-eii) show the electron concentration exceeds the critical value throughout the NCs despite the presence of the core-shell interface band bending. Shell- and uniformly-doped NCs (Figure 2.19c,d,eii) show a flat band on the surface while in core-doped NCs the accumulation region from the core has not yet reached flat band at the NC surface (Figure 2.19a,bii). Examination of electron concentration profiles (Figure 2.20) provides an explanation for the experimental observation that grain size does not show a clear dependence of dopant distribution. As shown in the figure, the localization length expands upon passivation of the surface, eliminating the separation between electron localization volumes (Figure 2.20). NC localization volumes are now metallic spheres touching via point contacts, which have a significantly lower contact resistance due to a decreased tunneling barrier width. Dopant profile dependence is observed in neither grain size nor contact resistance following surface passivation by ALD.

In conclusion, dopant distribution within NCs was shown to be an effective means to influence the electronic properties of bare ITO NC films (including overall conductivity, contact resistance, and electron localization length) at a constant overall tin concentration. These effects were understood based largely on the variations dopant distribution effected on the near-surface depletion layer. The model typically used to analyze variable temperature conductivity assumes full dopant ionization and uniform electron distribution within NCs, which is obviously not a fully physical description of our materials. However, no established theories describing electron conduction through NC films explicitly incorporate the potential for dopant segregation or intra-NC band bending. The assumptions of uniform electron distribution and full dopant ionization create some uncertainty in the meaning of the ES-VRH-GD derived localization length. However, considering the localization lengths derived from simulated electron concentration profiles agree well with the values derived from these fits to the experimental data suggests that any error caused by these assumptions is small compared to the influence of dopant segregation on transport properties. Conclusions drawn here should be viewed as a general case for doped semiconductors in the presence of surface states as our simulations and their interpretations are applicable across a range of systems.

We have examined the influence of dopant distribution within ITO NCs on the conductivity of NC films while also considering the presence of surface defects and the potential to passivate surface defects using ALD. Intra-NC dopant distribution plays a strong role in determining macroscopically observable electronic properties, such as film conductivity, and microscopic electronic properties, such as localization length and contact resistance, of bare NC films. The influence of dopant distribution on the properties listed above is the result of modulating surface depletion as these effects are eliminated following the deposition of alumina. These experimental results were supported by simulations of intra-NC band profiles, which showed identical trends in electron localization and its implications on contact resistance. Dopant distribution engineering offers a promising route through surface modification to improve the conductivity of NC films for device applications. Using intra-NC dopant distribution to tune surface depletion additionally creates interesting new avenues of study regarding phenomena and applications that depend on the interaction between the conduction electrons and the surrounding environments such as electrochromic devices, plasmonics materials, sensors, and catalysts.

Chapter 3: Influence of Surface Scattering on Optical Extinction Properties of Semiconductor Nanocrystals

This chapter text and figures have been adapted with permission from an in preparation work written in collaboration with Ankit Agrawal, Stephen Gibbs, Camila Saez, Robert Johns, and Delia Milliron. C.M.S. wrote the HEDA model, synthesized, characterized (SEM and ICP-AES), measured and fit optical extinction of ITO NCs. A.A. assisted in conceptualizing and writing the HEDA model. S.L.G. developed colloidal NC optical measurement techniques. C.A.S.C. conducted and analyzed SAXS measurements. R.W.J. assisted in experimental design and contributed intellectually. D.J.M. provided overall guidance. C.M.S. and D.J.M. wrote the manuscript with critical input from all the authors.

The optical extinction coefficient of localized surface plasmon resonance (LSPR) in doped semiconductor nanocrystals (NCs) is determined by free charge carrier concentration and the mechanisms for damping the oscillation of those free carriers. We investigate the extinction coefficient of tin-doped indium oxide (ITO) NCs through size and dopant concentration series and find extinction coefficients as high as 51.5 μm^{-1} in the near infrared for 8 atomic% Sn 20 nm diameter ITO NCs. We develop a new fitting procedure for the optical extinction of an ensemble of well-dispersed NCs that accounts for NC size heterogeneity, electron concentration heterogeneity, surface scattering, and near-surface electron depletion. This heterogeneous ensemble Drude approximation (HEDA) model utilizes the same number of variables as previous models and fits data as well or better while using inputs and fitting parameters that are described by physical phenomena. The model improves the understanding of free carrier motion in doped semiconductor NCs by more accurately extracting carrier concentration and carrier damping. The HEDA model captures individual NC optical properties and their contributions to the ensemble spectra. We find the extinction coefficient of an average NC varies linearly with a ratio of electron concentration to damping.

INTRODUCTION

Metal nanoparticles (NPs) and semiconductor nanocrystals (NCs) with high free charge carrier concentration are widely studied for their unique optical properties. Of principal importance is their strong, frequency-dependent polarizability arising from the oscillation of free charge carriers in response to incident electromagnetic radiation, otherwise known as a localized surface plasmon resonance (LSPR). The efficient extinction of incident radiation by nanoscale materials makes plasmonic NCs ideal candidates for use in electrochromic windows[24,59,60], sensors[61], and photothermal theranostics.[62–64] In contrast to metal NPs, doped semiconductor NCs derive free charge carriers from charge-compensated crystal defects. Consequently, doped semiconductors have carrier concentrations orders of magnitude lower than metals, placing the LSPR frequency (ω_{LSPR}) in the infrared (IR). The carrier concentration can easily be modulated in two ways: (1) synthetically through tuning dopant concentration and (2) post-synthetically by imposing an electrochemical bias or through photoelectrochemical charging. Unable to significantly modulate carrier concentration, metal NP LSPR frequency is primarily tuned by manipulating particle size and geometry.[65] The capability of tuning carrier concentration in semiconductor NCs IR LSPR tunability across a range of NC sizes, while Au NPs require sizes >200 nm or complex geometries to achieve IR absorption.[65,66] While several studies have investigated Au NP absorption coefficients, doped semiconductor NC absorption coefficients, particularly for doped metal oxides, are not yet established.[67,68] The applications mentioned above require high absorption coefficient materials to be feasible and given that doped metal oxide NCs show promise as strong IR absorbers, it is important to quantitatively investigate their optical extinction properties.

The far-field extinction spectrum of an ensemble of plasmonic NCs is influenced by a variety of factors. Of principal importance are damping processes that broaden the LSPR of individual NCs, broadening due to ensemble NC heterogeneity (heterogeneous broadening), and electron concentration. Individual NC damping is a direct measure of the electron mobility within a NC, which is dependent on the electron mean free path.

The mean free path has been proposed to be dominated by surface scattering in nanostructures with one or more dimensions smaller than the bulk mean free path. Wokaun et al. observed damping proportional to surface scattering in Ag NPs, which depends on electron concentration and NC radius.[69] The presence of surface scattering further necessitates accounting for near-surface depletion regions, which effectively shrink the volume accessible to conduction electrons. Zandi et al. and Agrawal et al. observed a strong effect of near-surface depletion regions on the optical properties of ITO NC films and dispersions.[30,31] Failure to account for near-surface depletion when fitting and interpreting LSPR spectra leads to an underestimation of damping within a NC due to an overestimate of volume accessible by conduction electrons.

Current optical models frequently convolute individual NC damping and heterogeneous broadening into a single damping term, leading to misinterpretation of material electronic properties. Despite the rather narrow size distributions achieved by recent synthetic developments, size polydispersity is still often nearly 10%.[29,32] A size distribution within an ensemble of NCs causes a distribution of intra-NC electron mobility due to variations in surface scattering, resulting in heterogeneous peak broadening. Additionally, Lounis et al. observed decreased dopant activation in ITO NCs in samples with dopant-enriched surfaces, indicating a decrease in dopant activation in the near-surface region.[11] The fraction of NC volume in the near-surface region shrinks monotonically as NC size increases. As a result, size polydispersity also creates free carrier concentration polydispersity within a population of NCs. Johns et al. showed striking variability in absorption peak energy and linewidth of single NC absorption spectra in populations of aluminum-doped zinc oxide and ITO NCs.[70] These results support the existence of significant carrier concentration polydispersity even among a group of NCs synthesized in the same batch, which results in heterogeneous broadening. Although many factors have been identified which influence the absorption spectrum of doped semiconductor NCs, a quantitative, physics-based model that captures each of these contributions has not yet been published.

Herein, we investigate the influence of NC size and dopant concentration on the extinction peak energy, lineshape, and extinction coefficient for doped semiconductor NCs. We use ITO NCs of varying dopant concentrations and sizes as a model system. Using quantitative analysis of optical spectra, we find the ITO NC extinction coefficient correlates strongly with NC size and dopant concentration. We suggest these correlations result from changes in electron concentration and damping due to differences in dopant activation, surface scattering, and near-surface depletion. We present a model for fitting optical spectra of NC ensembles that captures the effects of surface scattering, depletion near the NC surface, and heterogeneity in size and electron concentration. This procedure uses only well-known material constants and routinely measured NC physical properties to fit for a distribution of NC properties that cannot be easily measured directly, namely carrier concentration, carrier concentration polydispersity, and near-surface depletion width. We find the extinction coefficient of an average NC varies with a ratio between electron concentration and damping and the previously used model, the simple Drude model, underestimates the optical conductivity of NCs due to convoluting individual NC damping and heterogeneous broadening contributions. Finally, by analyzing the far-field response as a sum of contributions from individual NCs, the ensemble fit enables analysis of physical properties for the average NC within an ensemble.

THEORY

The Beer-Lambert Law defines the efficiency with which a material extinguishes light of a particular wavelength. The Beer-Lambert Law is considered from two perspectives. The first is within a homogeneous framework, represented as

$$A = \frac{\epsilon f_V l}{\ln(10)} \qquad (3.1)$$

where A is the measured extinction in base 10 log scale, also referred to as optical density (OD), f_V is the volume fraction of the absorbing material, l is the pathlength through the sample, $ln(10)$ is included to convert extinction to natural log scale, and ϵ is the extinction coefficient (μm^{-1}). The homogeneous extinction framework implicitly averages the extinction contributions of all NCs in the dispersion, yielding an effective extinction coefficient for a given distribution of NC sizes and dopant concentrations. The Beer-Lambert Law is capable of characterizing intra-NC electronic transport properties by modifications accounting for three phenomena: near-surface depletion, size polydispersity, and electron concentration polydispersity.

Metal oxide surfaces are passivated by adsorbed water species, including surface hydroxyls, that create a density of electronic states near the NC surface. For ITO, the surface states are within the optical band gap and result in a decreased electron concentration near the NC surface, known as a depletion region (Figure 3.1ai). Due to the buildup of electrostatic potential, depletion regions near the NC surface decrease the fraction of the NC volume accessible to conduction electrons, f_e (Figure 3.1aii). The radius of the spherical volume accessible to conduction electrons is $f_e^{1/3} r_{NC}$, where r_{NC} is the physical NC radius. This decreased radius is referred to as the electron accessible radius. Aside from decreasing the volume accessible to electrons, near-surface depletion creates a pseudo core-shell geometry where the NC is composed of a plasmonic core with an electron-deficient dielectric shell. This geometry requires a modification to the dielectric function of these materials to successfully model their optical response.

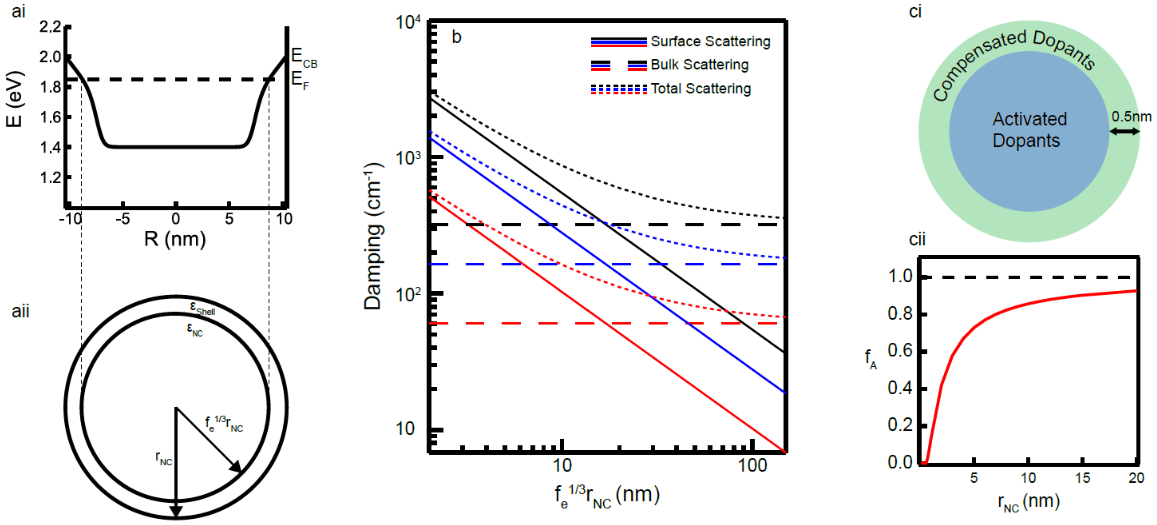

Figure 3.1: Theoretical concepts. NC with surface depletion band profile (ai) and schematic (aii), damping due to surface scattering, bulk scattering, and total scattering (b), and NC surface dopant compensation schematic (ci) and fractional activation (cii).

The LSPR line width of a single spherical NC is described by the damping constant, which is the rate at which conduction electrons scatter. While damping is often used as a fitting parameter, it can be calculated from the Drude conductivity as

$$\Gamma = \frac{(3\pi^2)^{\frac{1}{3}}\hbar}{m_e^*} n_e^{\frac{1}{3}} \left(\frac{1}{l_{MFP}}\right) \qquad (3.2)$$

where $\hbar$ is Planck's constant, m_e^* is the effective electron mass, n_e is the electron concentration, and l_{MFP} is the electron mean free path. For NCs of radius comparable to the material bulk mean free path, surface scattering influences the overall mean free path of NC conduction electrons. Surface scattering is included in the mean free path using an assumption of surface scattering being a specular scattering event and applying Matthiessen's rule as[71]

$$\frac{1}{l_{MFP}} = \left(\frac{1}{\frac{4}{3} r_{NC} f_e^{\frac{1}{3}}} + \frac{1}{l_{bulk}}\right) \qquad (3.3)$$

where l_{bulk} is the bulk mean free path (17 nm for ITO).[10] Surface damping contribution, bulk damping contribution, and total damping are plotted against the electron accessible radius for a range of electron concentrations in Figure 3.1b. Inspection of the total damping curve shows the dominance of surface scattering when the electron accessible radius is smaller than the bulk mean free path. Surface scattering becomes negligible at 150 nm, roughly 10x the bulk mean free path. The size-sensitivity of surface damping, particularly below 10 nm radius, and typical NC size polydispersity of about 10% emphasizes the need to account for NC size polydispersity when extracting NC properties for ensemble LSPR spectra.

Dopants in the near surface region of NCs and thin films exhibit a lower activation, which has strong implications for electron concentration.[11] We assume, at modest dopant concentrations, full activation of dopants outside of the near-surface region. The thickness of the deactivation layer is assumed to be 0.5 nm, half of an ITO unit cell, as shown in Figure 3.1ci.[9] Again, note the size-sensitivity of the fraction of activated dopants, f_A, in a uniformly doped NC for NCs of radius less than 10 nm (Figure 3.1cii). In NC populations of non-uniform size, dopant activation variations result in electron concentration heterogeneity. When measuring the optical response of an ensemble of NCs, both size polydispersity and carrier concentration variability will contribute to heterogeneous broadening of the LSPR peak. When not considered, heterogeneous broadening will obscure the values for carrier concentration and carrier damping deduced from the peak width. An alternative framework for the Beer-Lambert law is derived to take both near-surface depletion and NC heterogeneity into account. The new model is termed the Heterogeneous Ensemble Drude Approximation (HEDA).

We model size heterogeneity and electron concentration heterogeneity using Gaussian distributions, requiring modifications to existing optical models. To do this, we construct a two-parameter probability density function with a 41x41 data point mesh. The extinction of each of the 1600 points is probability-weighted and summed to give the ensemble extinction. The complex dielectric function, $\varepsilon_{NC,ij}(\omega)$, of each spherical electron cloud with radius, r_i, and electron concentration, $n_{e,j}$, is expressed using the Drude-Lorentz model

$$\varepsilon_{NC,ij}(\omega) = \varepsilon_\infty - \frac{\omega_{p,j}^2}{\omega^2 + i\omega\Gamma_{ij}} \qquad (3.4)$$

where ε_∞ is the material high-frequency dielectric constant, Γ_{ij} is the damping constant, and $\omega_{p,j}$ is the plasma frequency. The damping constant, Γ_{ij}, is defined using (3.2) and (3.3) as

$$\Gamma_{ij} = \frac{(3\pi^2)^{\frac{1}{3}}\hbar}{m_e^*} n_{e,j}^{\frac{1}{3}} \left(\frac{1}{\frac{4}{3} r_{NC,i} f_e^{\frac{1}{3}}} + \frac{1}{l_{bulk}} \right) \qquad (3.5)$$

where $\hbar$ is Planck's constant, m_e^* is the effective electron mass, and $n_{e,j}$ is the electron concentration. NC surfaces are relevant scattering sources and taken into consideration for NC radii less than 10 times the bulk electron mean free path as shown in Figure 3.1b. $\omega_{p,j}$ is defined as

$$\omega_{p,j} = \sqrt{\frac{q^2 n_{e,j}}{\varepsilon_0 m_e^*}} \qquad (3.6)$$

where q is the electron charge and ε_0 is the permittivity of vacuum. The presence of depletion near NC surfaces necessitates a core-shell model where the shell has a non-degenerate carrier concentration. The core-shell model utilizes a Maxwell-Garnett effective medium approximation (EMA) to define the dielectric function of a core-shell NC, $\varepsilon_{cs,ij}$, as

$$\varepsilon_{cs,ij}(\omega) = \varepsilon_{shell} \left(\frac{(\varepsilon_{NC,ij} + 2\varepsilon_{shell}) + 2f_e(\varepsilon_{NC,ij} - \varepsilon_{shell})}{(\varepsilon_{NC,ij} + 2\varepsilon_{shell}) - f_e(\varepsilon_{NC,ij} - \varepsilon_{shell})} \right) \qquad (3.7)$$

where ε_{shell} is the dielectric function of the depleted shell. It is noted that the EMA converges to $\varepsilon_{NC,ij}(\omega)$ when$f_e = 1$ and is therefore a general solution. In systems of non-interacting spheres the absorption cross section of a given particle, σ_{ij}, is defined by Mie theory as

$$\sigma_{abs,ij}(\omega) = 8\pi^2 r_{NC,i}^3 \omega \sqrt{\varepsilon_m} Imag \left\{ \frac{\varepsilon_{cs,ij}(\omega) - \varepsilon_m}{\varepsilon_{cs,ij}(\omega) + 2\varepsilon_m} \right\} \qquad (3.8)$$

where ε_m is the dielectric constant of the medium. For NCs smaller than 5% the wavelength of exciting light, scattering is negligible and extinction is assumed to be entirely due to absorption.[72] This assumption holds up to at least 150 nm diameter for ITO nanocrystals. Finally, the absorption cross section of all particles is then plugged into the heterogeneous Beer-Lambert law,

$$A = \frac{f_V l}{\ln(10)V} \sum_i^m \sum_j^n \left(\sigma_{abs,ij}(\omega) p_{n_{e,j}} p_{r_i} \Delta n_e \Delta r \right) \qquad (3.9)$$

where $p_{n_{e,j}}$ and $p_{r_{NC,i}}$ are the probabilities of $n_{e,j}$ and $r_{NC,i}$, respectively, Δn_e and Δr are the step sizes for n_e and r, respectively, and V is the probability normalized volume of a NC, defined as

$$V = \sum_i^m \sum_j^n \left(\frac{4}{3} \pi r_{NC,i}^3 p_{n_{e,j}} p_{r_{NC,i}} \Delta n_e \Delta r \right) \qquad (3.10)$$

Simulations of quantitative single NC extinction spectra using Equations (3.4)-(3.10) with varying electron concentration, size, and near-surface depletion are shown in Figure 3.2.

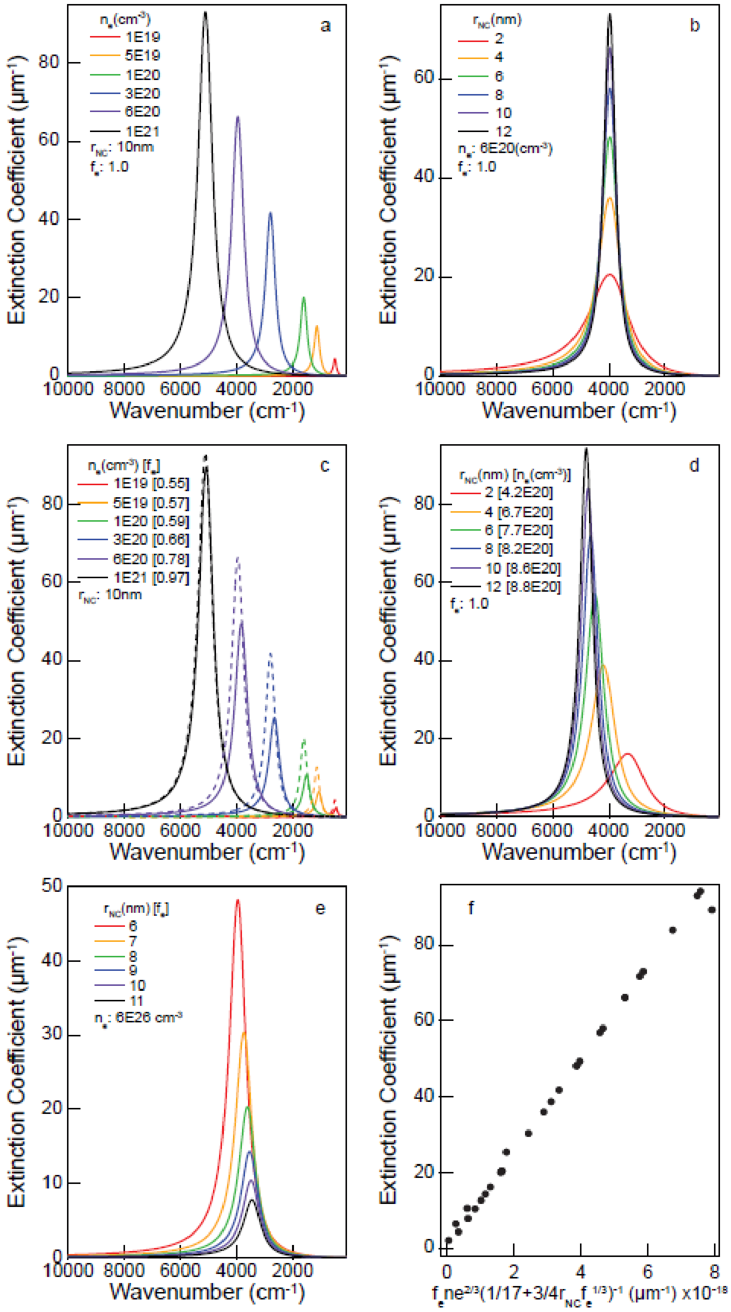

Figure 3.2: Simulated LSPR spectra with varying electron concentration (a), NC radius (b), electron concentration with a calculated depletion using a linear fit to Figure 5d (c), radius with a calculated electron concentration using a 0.5 nm surface deactivation layer (d), and depletion (e) and LSPR peak extinction coefficient v. a ratio of electron concentration to damping.

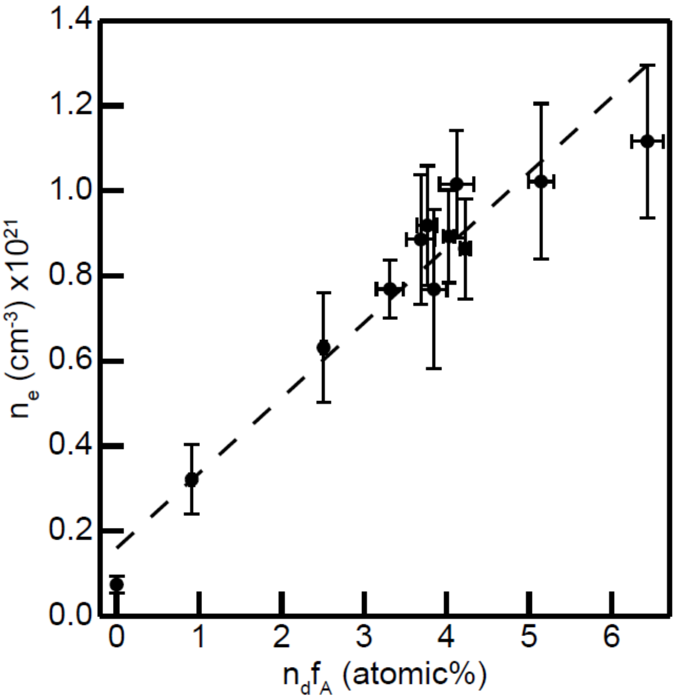

Figure 3.3: Dopant activation v. non-surface dopant concentration.

EXPERIMENTAL PROCEDURES

ITO NCs of varying dopant concentration and size were synthesized using adaptations of the slow injection method developed by Jansons et al.[32] This synthetic method leads to low polydispersity and highly controlled NC sizes and dopant concentration. The NC dopant concentration and size were varied by altering the molar concentration of tin and indium in the precursor solution and altering the injection volume, respectively. Overall NC size and size polydispersity were measured by small-angle x-ray scattering (SAXS) and verified by scanning transmission electron microscopy (STEM) image analysis (Figure 3.4 – 3.6). Overall dopant incorporation was quantified by elemental analysis using inductively coupled plasma-atomic emission spectroscopy (ICP-AES).

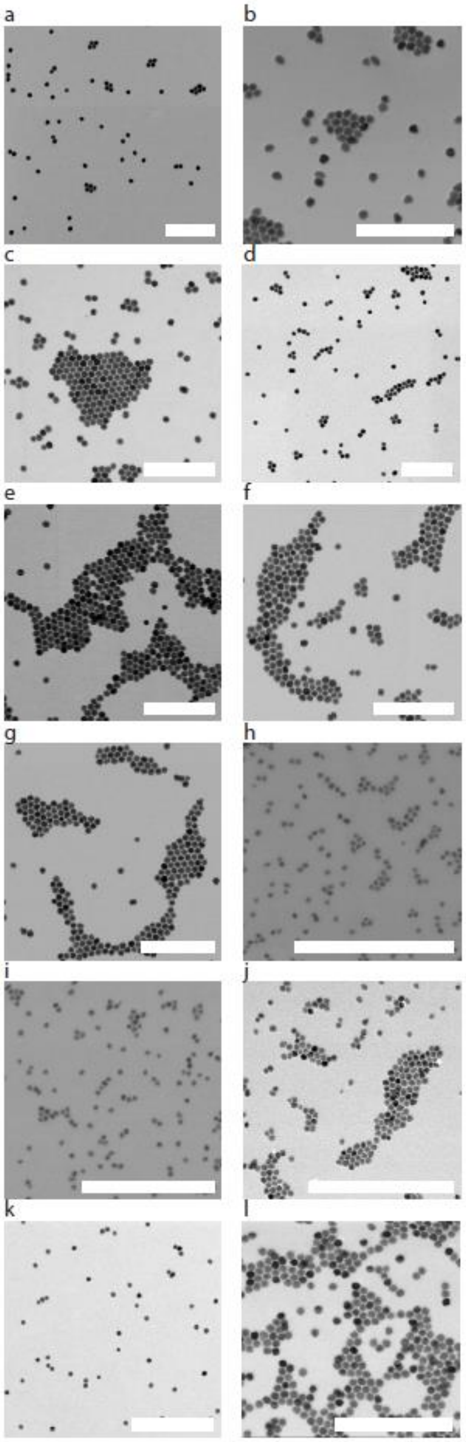

Figure 3.4: Scanning transmission electron microscopy (STEM) images of 20nm 0at% (a), 1at% (b), 3at% (c), 4.5at% (d), 5at% (e), 6.5at% (f), and 8at% (g) ITO NCs and 8nm (h), 9nm (i), 13nm (j), 14nm (k), and 16nm (l) 5at% ITO NCs. Scale bars represent 200nm.

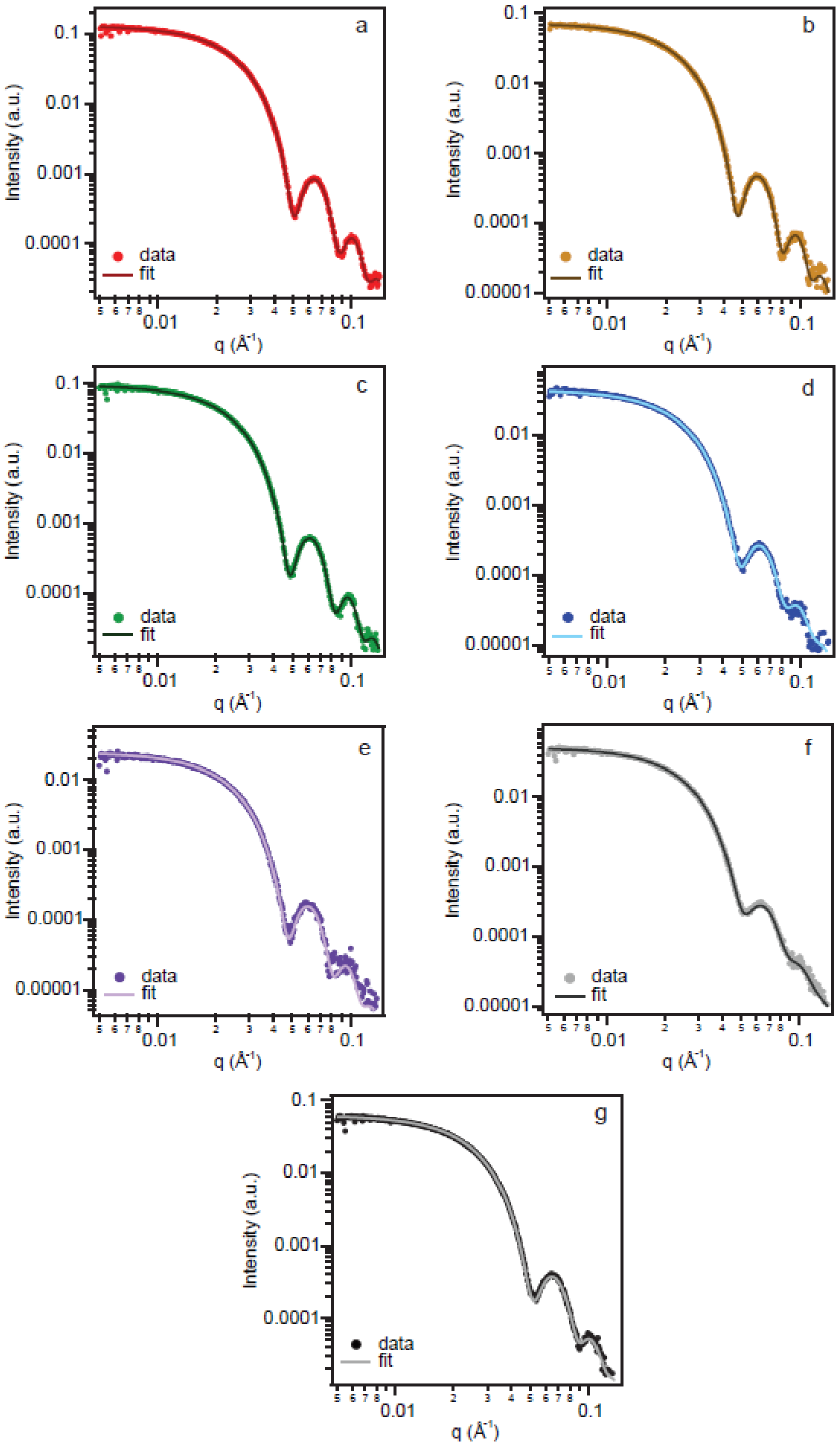

Figure 3.5: Doping series small-angle x-ray scattering.

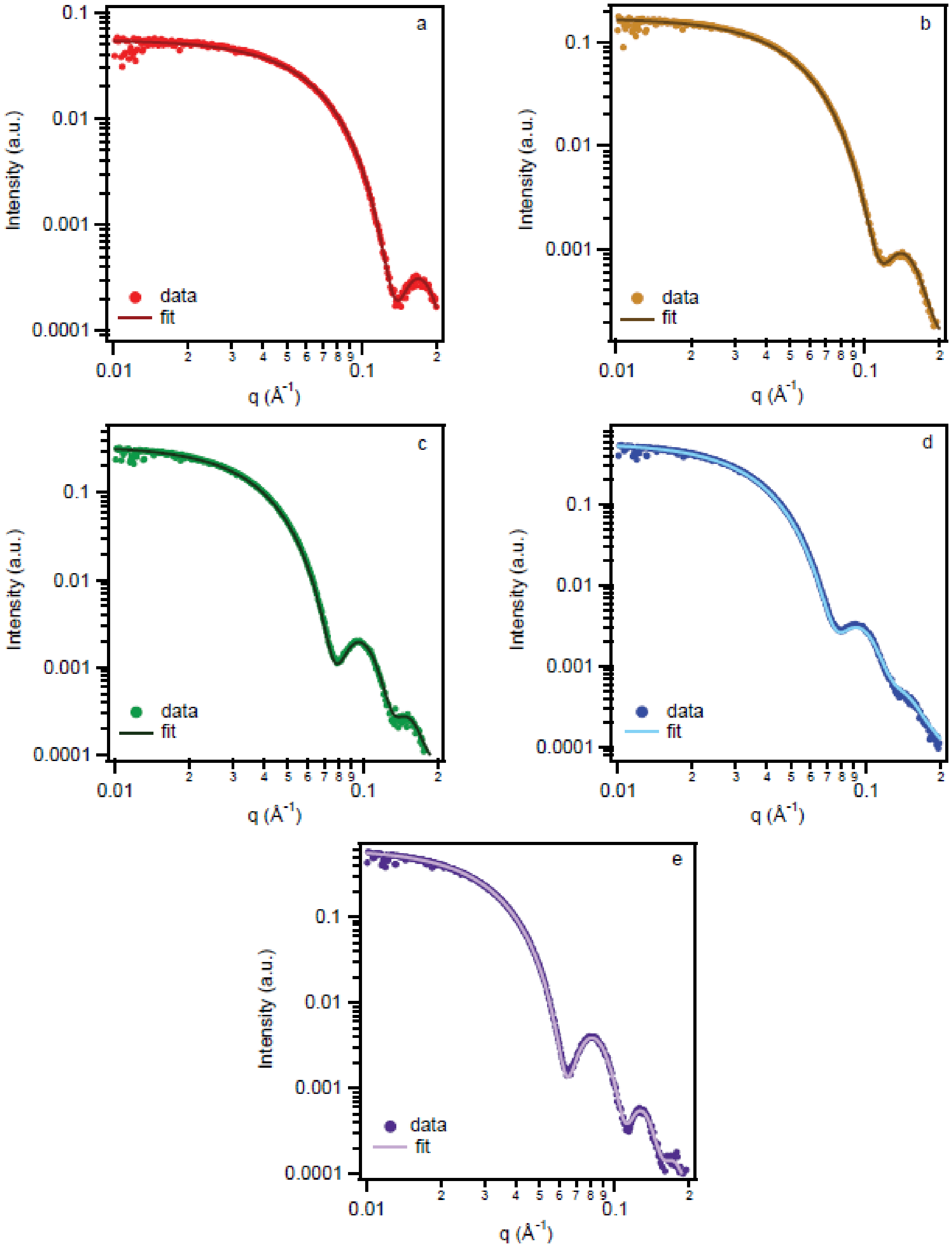

Figure 3.6: Size series small-angle x-ray scattering.

Stock NC dispersions for optical measurements were prepared in a solution of 1.8 mM oleic acid in tetrachloroethylene (TCE). Dilute dispersions in 1.8 mM oleic acid in TCE were prepared from stock solutions immediately before optical measurement and dilution factors were calculated using mass fractions of stock to total solution for each sample. Optical measurements were taken on dilute dispersions in a 0.5 mm pathlength liquid cell (Buck Scientific) with KBr windows using Fourier transform infrared (FTIR) spectroscopy (Bruker Vertex 70) and UV-vis-NIR (Agilent Cary series) spectrometers. All spectra were taken in transmission mode and are reported as extinction. NC volume fraction was determined using ICP-AES measurements of stock solutions. Fits to optical extinction spectra were conducted using a MATLAB code (Appendix I).

To investigate the optical extinction coefficient of ITO NCs, optical spectra were taken of NC dispersions at various NC volume fractions. Figure 7a shows a representative dilution series at 5 different dilution factors ranging from 840x to 160x relative to the stock solution. Accurate application of Mie theory requires the absence of NC-NC interactions such as NC-NC coupling or aggregation. This condition can be tested by varying the volume fraction of NCs in solution and inspecting extinction spectra for any response other than a linear dependence of OD on NC concentration across all wavelengths. This criterion is validated in two ways. First, when normalized, spectra of all dilutions overlap nearly perfectly (Figure 7b). Second, the peak extinction at ω_{LSPR} is plotted against NC volume fraction and shown to be linear (Figure 7c). The extinction coefficient is calculated from the slope of that line.

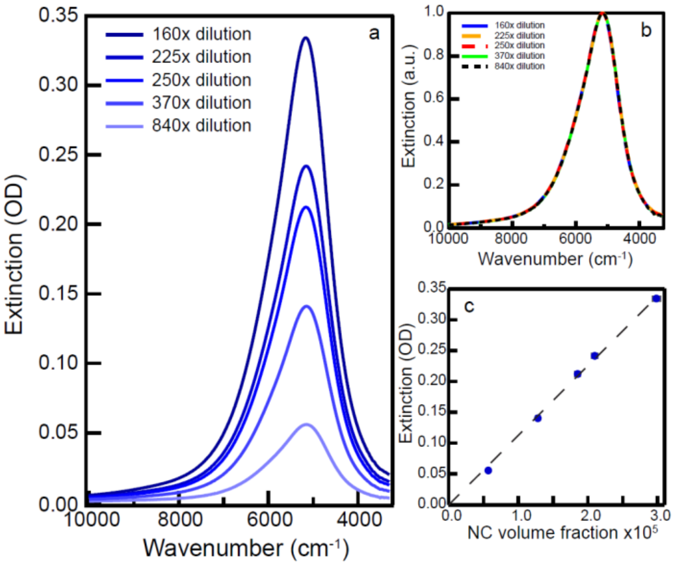

Figure 3.7: Extinction coefficient dilution series (a), normalized dilution spectra (b), and linear fit to extinction v. NC volume fraction at LSPR peak maximum (c) for 6.5 atomic% Sn doped 20nm ITO.

EXTINCTION COEFFICIENT OF ITO NCS

Two series were prepared to investigate the role of NC size and dopant concentration in the optical properties of ITO NCs: a size series from 8 to 20 nm diameter at 5 atomic% Sn and a doping series from 0 atomic% Sn to 8 atomic% Sn at 20 nm diameter. For each sample, the extinction coefficient at ω_{LSPR} was extracted from a linear fit of a series of dilution measurements as described previously. While the extinction coefficient is not useful for probing the physics of systems with heterogeneous broadening, it is a critical engineering parameter for the applications previously mentioned.

Figure 3.8a shows the quantitative extinction spectrum of each sample in the dopant series. Increasing dopant concentration causes a significant blue shift and increased intensity of the ITO LSPR peak as expected for an increase in carrier concentration. Inspection of Figure 3.8b shows an approximately linear relationship between extinction coefficient and dopant concentration up to about 5 atomic% Sn. The saturation or significant slowing of the trend with further doping is understood by a dopant compensation region in the Brouwer diagram of ITO above 5 atomic% Sn wherein it becomes favorable for the positive charge associated with Sn defect is compensated by forming a neutral defect cluster with a nearby oxygen interstitial.[9,12] The linear increase of extinction coefficient with dopant concentration can be ascribed to proportionally increasing electron concentration. This interpretation is supported by an increase of the optical band gap with dopant concentration, consistent with increasing electron concentration increasing, i.e. the Burstein-Moss effect (Figure 3.9).

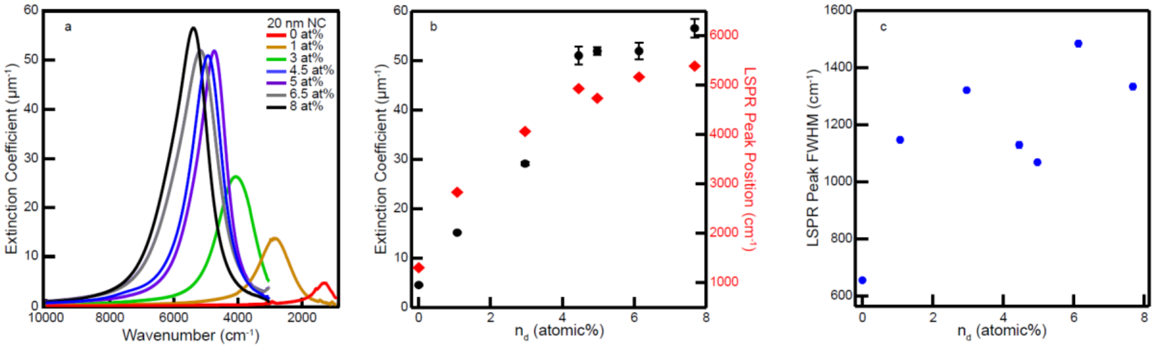

Figure 3.8: Dopant concentration series LSPR extinction spectra normalized to extinction coefficient (a), extinction coefficient and LSPR peak energy v. dopant concentration, n_d, (b), and LSPR peak full-width at half-maximum (FWHM) v. dopant concentration (c).

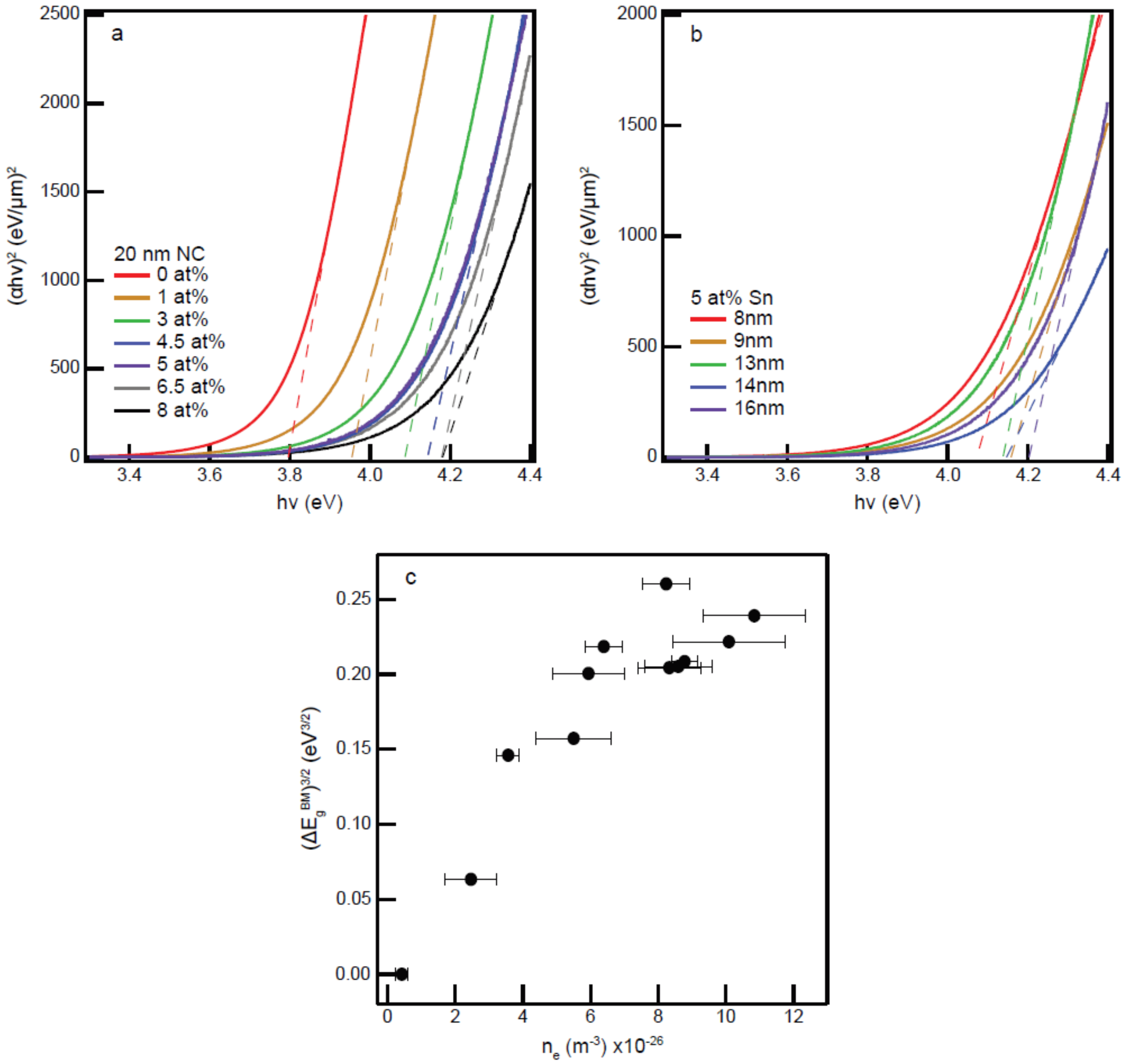

Figure 3.9: Tauc plot of ITO NCs showing optical bandgap widening with increasing dopant concentration (a) and NC radius (b).

LSPR peak energy rapidly increases with dopant concentration under 4.5 atomic% Sn before beginning to saturate, consistent with increased electron concentration. In the absence of near-surface depletion regions, the LSPR peak energy is expected to blue shift proportional with the square root of electron concentration. However, an increase in surface depletion width insulates the free electron core from the host dielectric with an electron-deficient, high dielectric, insulating shell. This change in dielectric surroundings means that increasing depletion width causes an LSPR red shift, and thus complicates the relationship between carrier concentration and LSPR peak frequency. This observation agrees with observations above that increasing dopant concentration primarily increases the electron concentration. Dopant concentration has a significant effect on LSPR peak width (Figure 3.8c). The LSPR peak full-width at half-maximum (FWHM) trends upward with increased dopant concentration. This trend is consistent with increased electron concentration at a constant NC radius leading to increased damping according to (3.2). However, FWHM is not sufficient to describe damping physics as it contains contributions from single NC damping and heterogeneous broadening.

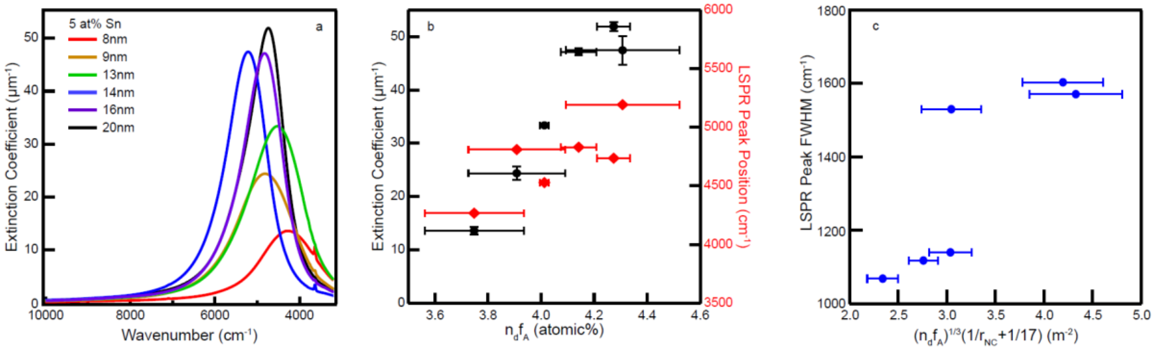

Figure 3.10: Size series LSPR extinction spectra normalized to extinction coefficient (a), extinction coefficient and LSPR peak energy v. activated dopant concentration (b), and LSPR peak full-width at half-maximum (FWHM) v. theoretical total damping (c). The orange (b) and purple (c) data points refer to the 13nm sample.

Figure 3.10a shows the quantitative extinction spectrum of each sample in the size series. Dopant activation is expected to be a function of purely size for dopant concentrations below ~5 atomic% Sn as shown in Figure 3.1cii. Due to this, dopant activation could be assumed constant for the dopant concentration series throughout the range of modest dopant concentration. For the size series the activated dopant concentration is defined as $n_d f_A$ where n_d is the dopant concentration by ICP-AES. Extinction coefficient trends approximately linearly with the activated dopant concentration (Figure 3.10b). This correlation is attributed, in part, to an increase of electron concentration at increased NC size and is supported by an increase of the optical band gap with NC radius at constant 5 at% Sn (Figure 3.9).

LSPR peak energy trends upward with activated dopant concentration. This is expected due to electron concentration increasing with NC radius, though this trend is still convoluted with changes to the near-surface depletion region volume fraction due NC size. NC radius is seen to have a strong effect on LSPR peak width (Figure 3.10c). The LSPR FWHM trends toward larger values as NC radius becomes smaller. The size effect on dopant activation convolutes the effect of decreasing mean free path due to surface scattering. Interestingly, smaller NCs have a lower expected electron concentration yet exhibit significantly larger values of FWHM. This is consistent with damping becoming surface scattering dominated, though it fails to capture heterogeneous broadening due to the size polydispersity of these samples, which ranges from 5% to 12%.

The extinction coefficients at the LSPR peak of ITO NCs reported here range from 4.5 μm^{-1} at 1300 cm^{-1} for 20 nm undoped indium oxide NCs to 51.5 μm^{-1} at 5289 cm^{-1} for 20 nm 8 atomic% Sn ITO NCs. It is interesting to compare the extinction coefficient of ITO NCs to Au nanostructures of similar size or peak energy. The highest extinction coefficient here, 51.5 μm^{-1}, is exceptionally high when compared to Au nanostructures with IR resonance, which exhibit an extinction coefficient of 22.7 μm^{-1} at 8620 cm^{-1}.[65] These Au nanostructures exhibit an extinction coefficient lower than that of 20 nm 3 atomic% Sn ITO NCs. Remarkably, the 20 nm 8 atomic% Sn ITO NCs have extinction coefficient quite close to 20 nm spherical Au NPs (74.2 μm^{-1}) despite having a peak nearly 14000 cm^{-1} lower in energy. The observations shown above require heterogeneous broadening to be accounted for to explore the underlying physics behind them.

EXTRACTING RELIABLE MATERIAL PARAMETERS WITH THE HEDA MODEL

The previous section exemplifies the type of conclusions that can be drawn from ensemble measurements of plasmonic NCs. General trends in extinction with size and doping can be determined, but their interpretation in terms of fundamental material properties is clouded by the contributions of size and carrier concentration polydisperity.

By fitting the extinction spectra with a model that accounts for heterogeneity, the behavior of free electrons in degenerately doped ITO NCs becomes more clear. Doping and size series optical extinction spectra were fit and analyzed using a novel fitting procedure that accounts for surface scattering, near-surface depletion, and heterogeneity. Previous simple Drude approximation (SDA) model fitting procedures require the input of pathlength and material constants that are used to fit for volume fraction, damping constant, and plasma frequency. These fitting procedures often yield a volume fraction that is not physically reconcilable with the known characteristics of the measured sample, but instead is a sort of correction factor used to simply scale the fitted extinction intensity. The model presented here, in addition to the basic inputs above, requires the input of the NC radius mean value, radius standard deviation, and measured volume fraction. The fitting procedure outputs are the electron concentration mean value and standard deviation and the non-depleted volume fraction. This represents an identical number of fit variables to previous SDA fitting procedures, but provides far richer and more accurate information regarding the properties of the NC ensemble.

Fitting with the HEDA model is compared to the SDA model using volume fraction as a fitting parameter, and to the SDA with volume fraction fixed to the directly measured value. An example of fits to experimental data using the three models is shown in Figure 3.11a and all fitted spectra are shown in Figure 3.12 and are summarized for the dopant concentration (Table 3.1) and NC size (Table 3.2) series. Comparing the fits in Figure 5a reveals shortfalls of the SDA model: the inability to fit proper peak shape, peak intensity, and converge on the measured volume fraction consistently. The SDA overestimates peak intensity and finds volume fractions lower than measured experimentally in almost every case. These discrepancies arise because the SDA does not account for near-surface depletion and the associated core-shell EMA, and it convolutes heterogeneous broadening and single NC damping as a single damping term. When the volume fraction is fixed to the measured value, the damping tends to increase and the plasma frequency red shifts as the fit attempts to decrease peak intensity, resulting in poor fits as shown in Figure 3.11a.

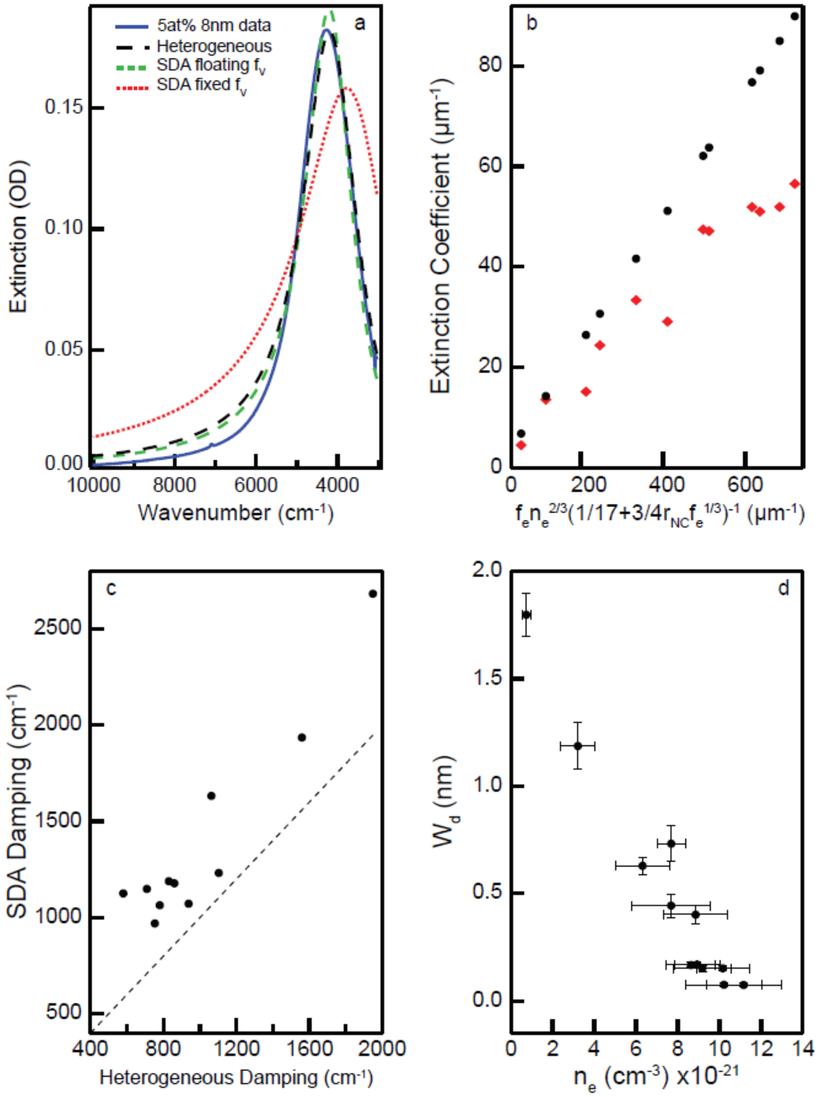

Figure 3.11: Fitting extinction spectra. Simple Drude Approximation (SDA) with a floating NC volume fraction, SDA with measured NC loading, and heterogeneous Drude (HEDA) fits to extinction data for 5atomic% 8 nm ITO (a), average NC (black) and ensemble (red) extinction coefficient dependence on plasma frequency and damping (b), SDA damping constant compared to the HEDA-derived damping (c), and near-surface depletion width versus electron concentration (d).

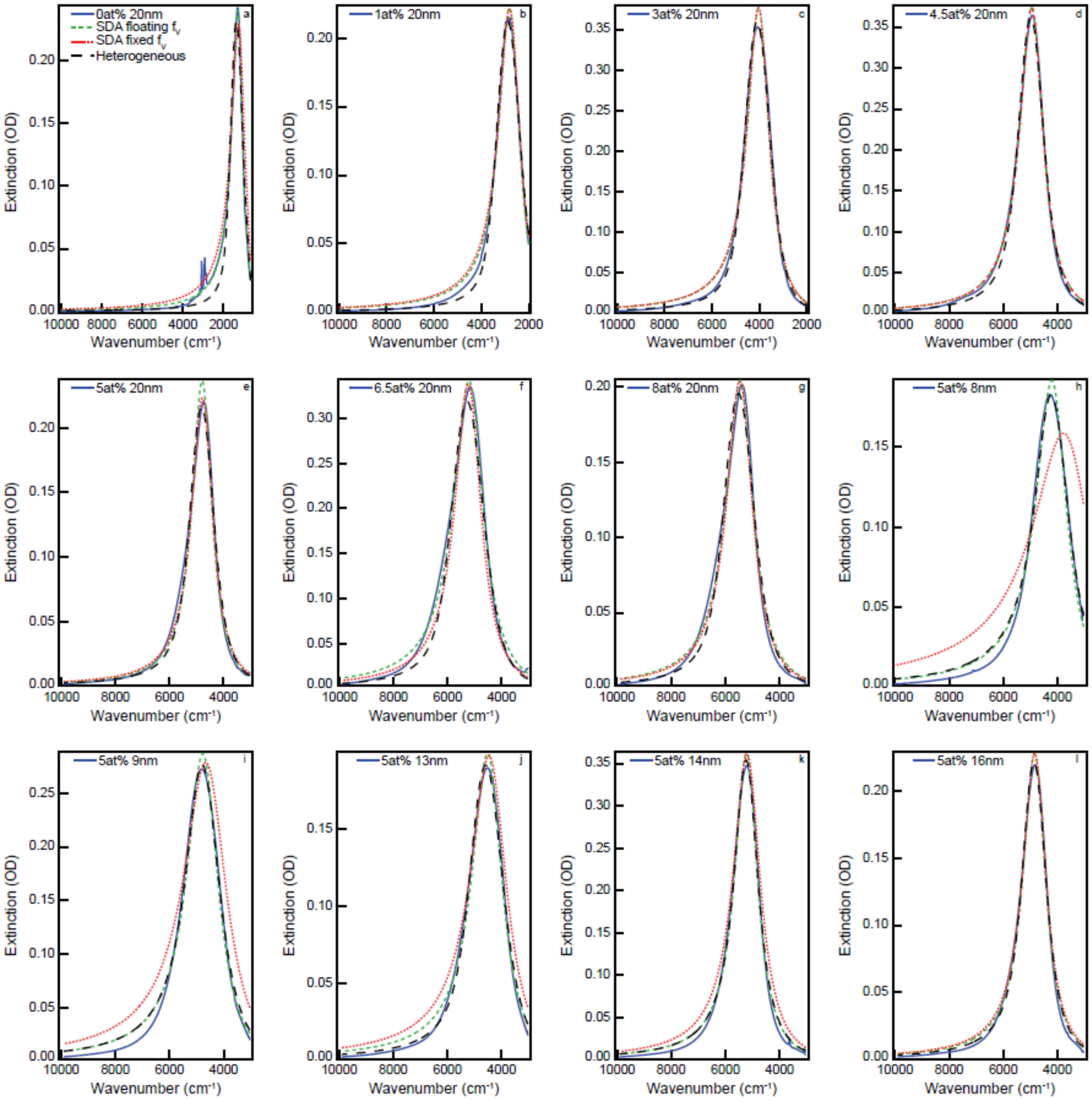

Figure 3.12: Optical extinction fits with simple Drude approximation (SDA) with a floating NC loading, SDA with measured NC loading, and heterogeneous Drude model for 20nm 0at% (a), 1at% (b), 3at% (c), 4.5at% (d), 5at% (e), 6.5at% (f), and 8at% (g) ITO NCs and 8nm (h), 9nm (i), 13nm (j), 14nm (k), and 16nm (l) 5at% ITO NCs.

Table 3.1: Dopant concentration series optical extinction fit parameters.

Sample Details	**At% Sn**	**0**	**1.07**	**2.97**	**4.45**	**6.13**	**7.68**
	μ_r (nm)	10.40	9.60	10.23	9.97	9.64	9.89
	σ_r (nm)	0.58	0.89	0.63	0.91	1.17	1.19
	f_v from ICP	2.44E-04	6.44E-05	5.43E-05	3.30E-05	2.98E-05	3.27E-05
SDA w/ Floating fv	f_v	1.90E-04	6.07E-05	5.37E-05	3.28E-05	3.48E-05	3.43E-05
	w_p (cm^{-1})	3831	8234	11777	14469	15236	15950
	Damping (cm^{-1})	667	1065	1138	1060	1360	1229
	n_e (cm^{-3})	6.6E+19	3.0E+20	6.2E+20	9.3E+20	1.0E+21	1.1E+21
SDA w/ Fixed fv	w_p (cm^{-1})	3691	8199	11771	14468	15294	15963
	Damping (cm^{-1})	835	1126	1149	1064	1189	1178
	n_e (cm^{-3})	6.1E+19	3.0E+20	6.2E+20	9.3E+20	1.0E+21	1.1E+21
Heterogeneous Model	μ_{ne} (cm^{-3})	4.2E+19	2.5E+20	5.5E+20	8.6E+20	1.0E+21	1.1E+21
	σ_{ne} (cm^{-3})	1.8E+19	7.6E+19	1.1E+20	9.9E+19	1.7E+20	1.5E+20
	dep	0.44	0.62	0.77	0.80	0.99	0.90
Calculated Heterogeneous Damping (cm^{-1})		307	539	645	718	776	798

Table 3.2: NC size series optical extinction fit parameters.

Sample Details	At% Sn	5.42	5.54	5.03	5.36	5.03	4.97
	μ_r (nm)	**4.32**	**4.55**	**6.89**	**7.11**	**7.97**	**10.19**
	σ_r (nm)	0.49	0.46	0.85	0.57	0.54	0.94
	f_v from ICP	6.06E-05	5.05E-05	3.30E-05	3.35E-05	2.12E-05	7.72E-06
SDA w/ Floating fv	f_v	3.07E-05	3.65E-05	2.70E-05	2.80E-05	2.02E-05	7.47E-06
	w_p (cm^{-1})	12305	13932	13204	15261	14159	13995
	Damping (cm^{-1})	1398	1419	1359	1037	1022	890
	n_e (cm^{-3})	6.8E+20	8.7E+20	7.8E+20	1.0E+21	9.0E+20	8.7E+20
SDA w/ Fixed fv	w_p (cm^{-1})	11035	13622	13055	15196	14143	13965
	Damping (cm^{-1})	2683	1936	1632	1232	1072	970
	n_e (cm^{-3})	5.4E+20	8.3E+20	7.6E+20	1.0E+21	8.9E+20	8.7E+20
Heterogeneous Model	μ_{ne} (cm^{-3})	3.6E+20	6.4E+20	5.9E+20	8.8E+20	8.2E+20	8.3E+20
	σ_{ne} (cm^{-3})	3.3E+19	5.4E+19	1.1E+20	3.8E+19	7.0E+19	9.3E+19
	dep	0.25	0.46	0.52	0.61	0.78	0.90
Calculated Heterogeneous Damping(cm^{-1})		1433	1405	957	1021	868	754

In addition to an improved fit quality afforded by the HEDA model, it also enables the analysis of the properties of the average NC in an ensemble by deconvoluting heterogeneous and homogeneous broadening. The absorption of the average NC in dispersion is simulated using the mean value electron concentration, size, and near-surface depletion derived from HEDA fitting (Figure 3.13). Figure 3.11b shows the extinction coefficient at LSPR peak of an average NC in the measured series and the ensembles. Single NC absorption exhibits a significantly higher extinction coefficient than the corresponding ensemble. This difference arises due to the distribution of peak locations, intensities, and widths that broaden the absorption peak of the ensemble and reducing the peak intensity. Additionally, the extinction coefficient of an average NC increases with a ratio of electron concentration to damping multiplied by the free electron volume fraction. This trend is in agreement with the analytical solution of Mie theory at the LSPR peak and the simulations conducted in Figure 3.2. This relationship reveals the key to achieving high absorbing NC ensembles in the IR as monodisperse NCs of large radius and high dopant concentration.

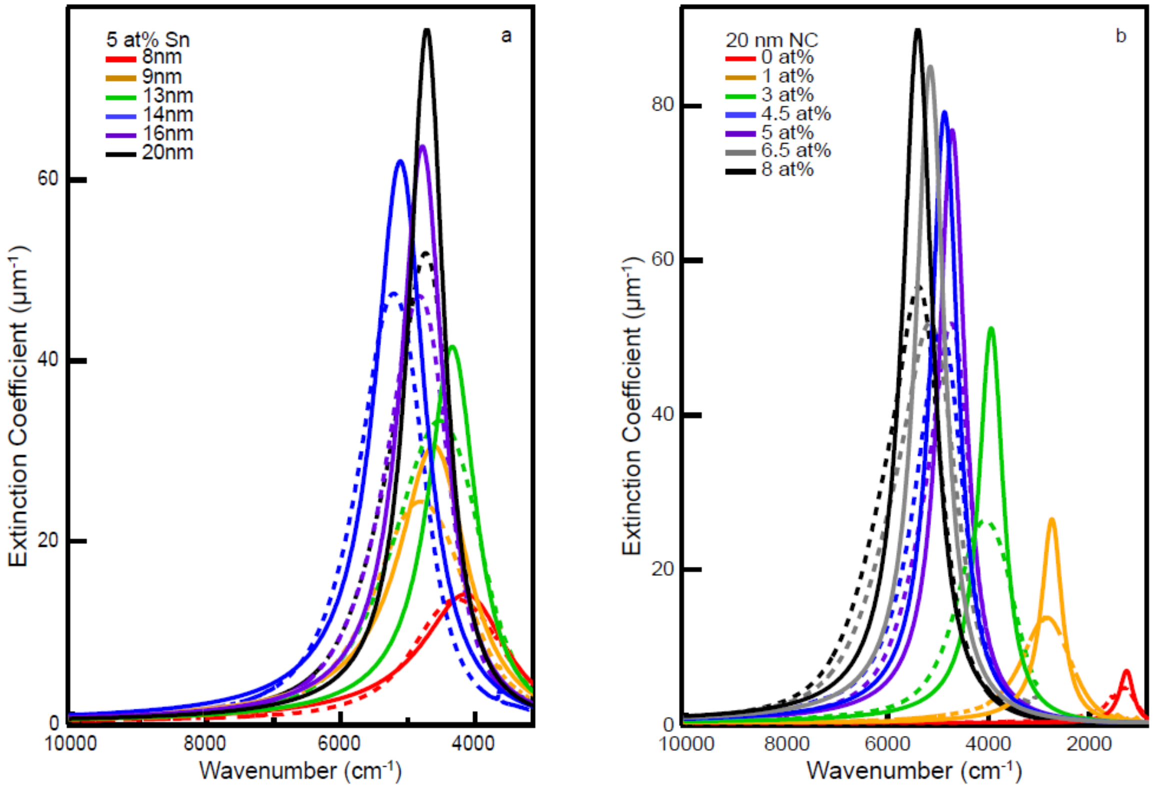

Figure 3.13: Average NC LSPR absorption spectra compared to ensemble absorption. Average NC absorption coefficient (solid) is higher and shows a narrower lineshape than ensemble absorption coefficient (dashed).

Starting from the Drude-Lorentz dielectric function,

$$\varepsilon_{NC}(\omega) = \varepsilon_{\infty} - \frac{\omega_p^2}{\omega^2 + i\omega\Gamma} \qquad (3.11)$$

The NC dielectric function can described as a summation of the real and imaginary parts of the dielectric function

$$\varepsilon_{NC}(\omega) = \varepsilon_1(\omega) + i\varepsilon_2(\omega) \qquad (3.12)$$

Where

$$\varepsilon_1(\omega) = \varepsilon_{\infty} - \frac{\omega_p^2}{\omega^2 + \Gamma^2} \qquad (3.13a)$$

and

$$\varepsilon_2(\omega) = \frac{\omega_p^2 \Gamma}{\omega(\omega^2 + \Gamma^2)} \qquad (3.13b)$$

Plugging the dielectric function into the Mie Theory absorption coefficient

$$\epsilon_{NC} = \frac{\sigma}{V_{NC}} = 6\pi\omega\sqrt{\varepsilon_m} Imag\left\{\frac{\varepsilon_{NC}(\omega)-\varepsilon_m}{\varepsilon_{NC}(\omega)+2\varepsilon_m}\right\} = 6\pi\omega\sqrt{\varepsilon_m} Imag\left\{\frac{\varepsilon_1(\omega)+i\varepsilon_2(\omega)-\varepsilon_m}{\varepsilon_1(\omega)+i\varepsilon_2(\omega)+2\varepsilon_m}\right\} \quad (3.14)$$

The LSPR condition is defined by

$$\varepsilon_1(\omega) = -2\varepsilon_m \quad (3.15)$$

Plugging (3.15) in (3.14)

$$\epsilon_{NC} = 6\pi\omega_{LSPR}\sqrt{\varepsilon_m} Imag\left\{\frac{i\varepsilon_2-3\varepsilon_m}{i\varepsilon_2}\right\} \quad (3.16)$$

(3.16) simplifies to

$$\epsilon_{NC} = 18\pi\omega_{LSPR}\sqrt{\varepsilon_m}\frac{\varepsilon_m}{\varepsilon_2} \quad (3.17)$$

The imaginary part of the dielectric is solved for as

$$\varepsilon_1 = \varepsilon_\infty - \frac{\omega_p^2}{\omega_{LSPR}{}^2+\Gamma^2} = -2\varepsilon_m \rightarrow \frac{\omega_p^2}{\omega_{LSPR}{}^2+\Gamma^2} = \varepsilon_\infty + 2\varepsilon_m \quad (3.18a)$$

$$\varepsilon_2(\omega) = \frac{\omega_p^2\Gamma}{\omega_{LSPR}(\omega_{LSPR}{}^2+\Gamma^2)} = \left(\frac{\Gamma}{\omega_{LSPR}}\right)\left(\frac{\omega_p^2}{\omega_{LSPR}{}^2+\Gamma^2}\right) = \left(\frac{\Gamma}{\omega_{LSPR}}\right)(\varepsilon_\infty + 2\varepsilon_m) \quad (3.18b)$$

Plugging (3.18b) into (3.17)

$$\epsilon_{NC} = 18\pi\varepsilon_m^{\frac{3}{2}}\frac{\omega_{LSPR}{}^2}{\Gamma} \quad (3.19)$$

The relationship between ω_{LSPR} and ω_p is found by

$$\varepsilon_1 = \varepsilon_\infty - \frac{\omega_p^2}{\omega_{LSPR}{}^2+\Gamma^2} = -2\varepsilon_m \rightarrow \omega_{LSPR}^2 = \frac{\omega_p^2}{\varepsilon_\infty+2\varepsilon_m} - \Gamma^2 \quad (3.10)$$

Finally, plugging (3.10) into (3.9)

$$\epsilon_{NC} = 18\pi\varepsilon_m^{\frac{3}{2}}\left(\frac{\omega_p^2}{\Gamma(\varepsilon_\infty+2\varepsilon_m)} - \Gamma\right) \quad (3.11)$$

It is clear from (3.11) that when $\omega_p \gg \Gamma$, $\epsilon_{NC} \propto \frac{\omega_p^2}{\Gamma} \propto n_e^{\frac{2}{3}} * \left(\frac{1}{17} + \frac{1}{\frac{4}{3}r_{NC}f_e^{\frac{1}{3}}}\right)^{-1}$

Fitting LSPR ensemble absorption with SDA is a common method for assessing the conductivity or mobility of electrons within NCs. These properties are calculated from the fitted electron concentration and damping constant. While the SDA-derived electron concentration does not differ significantly from the average electron concentration found by fitting with HEDA model, simulating absorption spectra of average NCs reveals that single NCs exhibit a significantly reduced linewidth than the associated ensemble. Using SDA to represent the apparent damping of the ensemble and HEDA model to represent the average NC, Figure 5c shows a comparison of ensemble and single NC damping. The SDA damping is 12-110% higher than the damping of an average NC in the samples fit using the HEDA model. The overestimate of damping by the SDA results from the assumption of each NC being identical, artificially broadening the LSPR when that assumption fails. The overestimation of damping results in misleadingly low conductivity and mobility within the NCs and inhibits meaningful interpretation of these material properties.

One potential source of error for the HEDA model is non-physical fit parameter correlations. While the HEDA model has an identical number of free parameters as the SDA, it contains multiple broadening parameters (specifically, f_e and σ_{n_e}). The depletion width of a semiconductor with a depleted surface is expected to be dependent on the ionized dopant concentration. Figure (3.11d) shows the depletion width, $W_d = r_{NC}(1-f_e)^{\frac{1}{3}}$, decreases with the electron concentration of NCs in the dispersion, as expected. Electron concentration is considered to be representative of the ionized dopant concentration here. The second fitted broadening parameter, σ_{n_e}, shows no correlation with the non-depleted volume fraction (Figure 3.14). This independence of the two primary broadening factors indicates the HEDA model is robust.

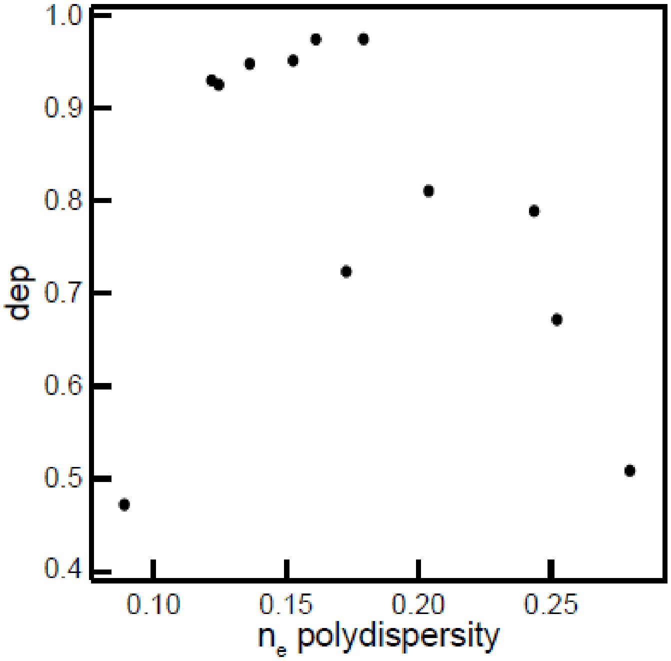

Figure 3.14: Deconvolution of optical parameters. Plasmonic volume fraction (HEDA model fit f_e), which determines homogeneous broadening, and heterogeneous broadening (HEDA model fit electron concentration polydispersity, σ_{n_e}) parameters show no correlation.

In conclusion, NC dopant concentration and size were shown to play a prominent role in determining LSPR peak location, lineshape, and intensity. These effects are understood based on surface dopant compensation, surface scattering, and near-surface depletion. These effects were analyzed using a novel fitting procedure to account for NC size and electron concentration heterogeneity and near-surface depletion, presenting a powerful for characterizing electronic properties of NCs that are not easily measured. The HEDA model showed a strong correlation between electron concentration and extinction coefficient for ITO NCs. These results should be viewed as generally valid for doped semiconductor NCs at sizes comparable to the material bulk mean free path.

We have examined the influence of NC size and dopant concentration on the LSPR of ITO NCs. NC extinction coefficient and LSPR peak position were shown to correlate with dopant concentration and NC size. This was understood by surface dopant compensation resulting in a lower dopant activation for smaller NCs. LSPR peak width was shown to be determined by single NC damping and heterogeneous broadening. In the size regime investigated here single NC damping is dominated by surface scattering and heterogeneous broadening results from NC to NC variations in size and electron concentration. These results were bulwarked by a novel LSPR peak fitting procedure, accounting for surface scattering, heterogeneity, and near surface depletion without adding fitting variables to previous models. This study indicates synthesizing large and highly doped semiconductor NCs offers a powerful method for achieving narrow and high extinction coefficient LSPR in the infrared, a necessary characteristic for electrochromic devices, sensors, and local heating applications.

Chapter 4: Mapping the Electron Transport Phase Diagram for Doped Semiconductor Nanocrystal Films

This chapter text and figures have been adapted with permission from an in preparation work written in collaboration with Gary Ong, Stephen Gibbs, and Delia Milliron. C.M.S. designed the experiments, developed the scientific theories presented, synthesized and prepared the samples, characterized the samples (XRD, XPS, optical, STEM, SEM, etc) of all samples, variable temperature conductivity measurements, variable temperature data analysis, and principle draft author. G.O. developed the ligand removal procedure. S.G. assisted in theory development. D.M. provided overall guidance.

The phase diagram of doped semiconductor nanocrystal (NC) film transport mechanisms is determined by a combination of NC size, electron concentration, and contact radius. We investigate the phase diagram using tin-doped indium oxide (ITO) NC films of various size NCs, electron concentration, and contact radius and achieve 3 distinct conduction mechanisms. We find NC films with low contact conductance conduct electrons through a hopping mechanism. NC films with contact conductance above a critical value conduct electrons through a granular metal mechanism. The transition from hopping to granular metal is known as the MIT and is independent of NC size. Finally, when the contact conductance is comparable to the intra-NC conductance, the NC film behaves as a metallic film. The transition from granular metal to metallic film is found to be independent of electron concentration.

INTRODUCTION

Nanocrystal (NC) derived transparent conductive oxide (TCO) films are investigated for use in solar cells, displays, and electrochromic windows.[14,16] These applications require highly conductive TCO films to be practical, which has traditionally been the shortfall of NC films.[17–19] Efforts to increase NC film conductivity include exchanging native synthetic ligands for shorter organic or inorganic ligands, ligand removal, dopant distribution engineering, sintering NCs, and atomic layer deposition (ALD).[18–21,26,29,36,45] While removing native ligands results in a large increase in NC film conductivity, the NC surface is left open to adventitious water species. Adsorbed water species cause the formation of a near surface depletion region, electronically separating neighboring NCs.[26,29] Near surface depletion regions can be alleviated through deposition of alumina by ALD.[26,29] Despite these advancements in methods for achieving highly conductive NC films, NC films do not exhibit conductivity comparable to that of their thin film analogs and often do not conduct electrons through the same mechanism as thin films.

Commercially available doped semiconductor thin films transport electrons through a metallic conduction mechanism. These films display a nonzero conductivity at 0K and have a negative slope of conductivity with respect to temperature. In contrast, NC films frequently exhibit thermally activated electron transport with a positive slope of conductivity with respect to temperature and zero conductivity at 0K. The electron transport properties of NC films are indicative of an insulator. Significant effort has focused on defining the criteria at which NC films undergo a metal-insulator transition (MIT).[36,42,45] The most common route on the frontier of this field is the sintering of neighboring NCs to increase inter-NC conductance. During such sintering processes, NCs fuse through a necking process that defines the electron transport between NCs.

Electron conductance through a metallic circular constriction, known as contact conductance, g_c, is defined quasiclassically by the Sharvin equation[73] as

$$g_c = \frac{k_F^2 r_c^2}{4} \qquad (4.1)$$

where k_F is the fermi wavevector and r_c is the radius of contact between neighboring NCs. The Fermi wavevector is defined as

$$k_F = (3\pi^2 n_e)^{\frac{1}{3}} \qquad (4.2)$$

where n_e is the electron concentration. Chen et al. proposed NC films undergo an MIT when the contact conductance is greater than unity.[42] For NCs in intimate contact, this criterion simplifies to

$$k_F r_c \geq 2 \qquad (4.3)$$

The criterion presented by Chen et al. intuitively requires a contact radius at least twice the size an electron at the Fermi energy.

Several studies have investigated the above criterion by varying contact radius and electron concentration. Chen et al. initially investigated the influence of increasing phosphorous dopant concentration in 7-8nm silicon NCs and found a monotonic increase of electron concentration and electron localization length.[42] Lanigan and Thimsen utilized atomic layer deposition to effectively sinter neighboring zinc oxide (ZnO) NCs together as a method for controlling contact radius from 0.6nm to over 3.5nm.[45] Lanigan and Thimsen found 7nm ZnO NC films with contact radii greater than 3nm to have a nonzero conductivity at 0K. Greenberg et al. used intense light pulses before and after atomic layer deposition of alumina to independently vary contact radius and electron concentration in films of 10nm ZnO NCs.[36] The latter two studies achieved the criterion proposed by Chen et al., but were unable to observe the classic thin film behavior of resistivity positively trending with temperature. Herein we investigate the MIT of NC films as it relates to NC size, electron concentration, and contact radius.

Specifically, we develop a phase diagram for the MIT of doped semiconductor NCs by using ITO NCs as a model system. The contact radius between neighboring NCs is varied using atomic layer deposition of indium oxide (IO) and conductivity of ITO NC films and inter-NC contact conductance are found to increase with $k_F^2 r_c^2$, as expected by the Sharvin equation. We develop novel MIT criteria to describe the NC electron transport phase space, which contains two transitions: an insulator to granular metal transition (MIT) that occurs when contact conductance is above a critical value ($\ln\left(\frac{E_C}{\delta}\right)/6\pi$ in 3D) and a granular metal to metallic transport transition when contact conductance is greater than intra-NC conductance. Based on these criteria, we show a clear transition from hopping conduction to granular metal conduction, defined as the MIT, and further, a transition to classical metal transport.

EXPERIMENTAL PROCEDURES

ITO NCs were synthesized using a method adapted from the slow growth methods developed by Jansons et. al.[32] This synthetic method yielded NCs of low size polydispersity as sized by small-angle x-ray scattering (SAXS) and validated by scanning transmission electron microscopy. Dopant incorporation was quantified by elemental analysis using inductively coupled plasma-atomic emission spectroscopy (ICP-AES) for overall Sn dopant concentration.

Colloidal NCs were spin-coated from a concentrated dispersion in a mixed solvent of 1:1 hexane:octane onto silicon and quartz substrates, yielding approximately 100-200 nm thick films. To expose the NC surface for chemical treatment, the organic ligands used in colloidal synthesis were removed by an *in situ* ligand displacement with 0.1M ammonium hydroxide in acetonitrile. Ligand exchanges of x-type to x-type nature are well known to be achievable through mass action. Ligand removal was verified by Fourier-transform infrared spectroscopy. The resulting films are comprised of densely packed hydroxyl-capped ITO NCs with direct contacts between NCs and minimal cracking (Figure 4.1a). Porosity of NC films prepared on silicon substrates was determined using ellipsometric porosimetry (EP) with toluene as the dielectric contrast solvent. EP data from 400 nm to 1000 nm wavelength was fit using software provided by JA Woollam and yielded consistent volume fractions between 0.72 and 0.78 for all films before ALD.

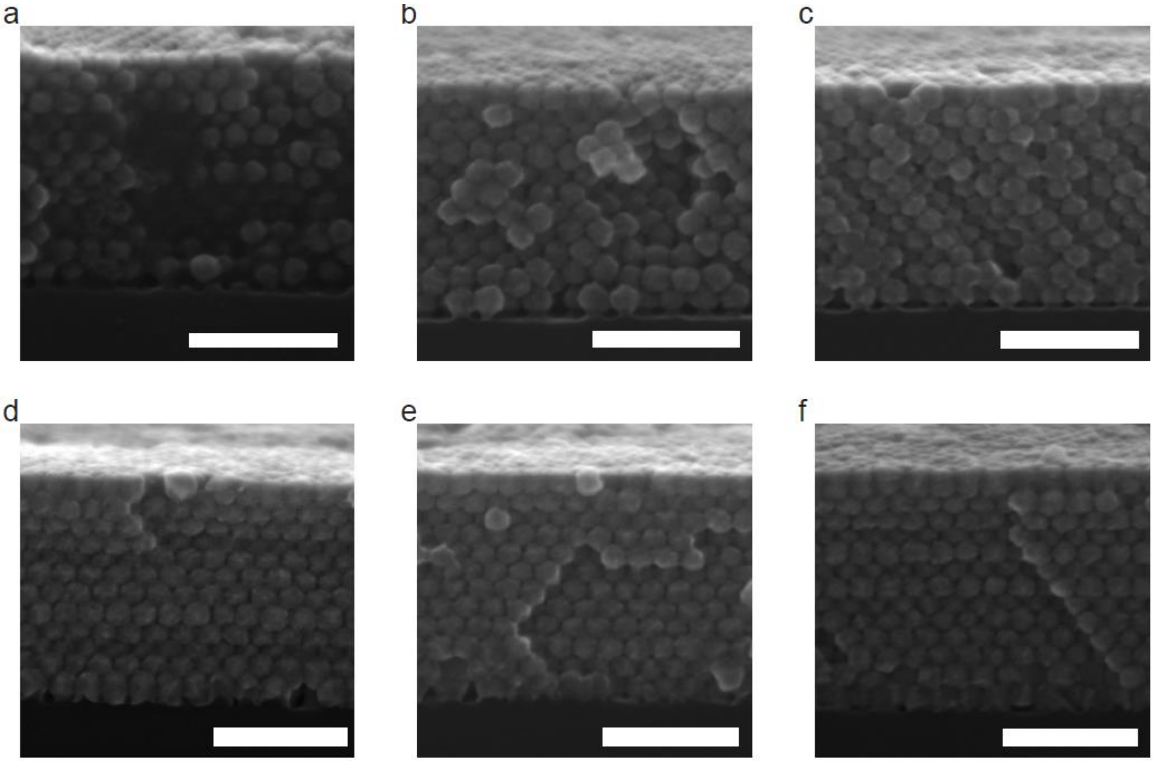

Figure 4.1: NC film SEM cross-section for 20nm 0 atomic% Sn ITO NCs following 0 (a), 8 (b), 16 (c), 24 (d), 30 (e), and 40 (f) cycles of IO ALD. Scale bars represent 100nm.

Contact radius was varied using 0-40 IO ALD cycles to effectively sinter neighboring NCs. Deposition was carried out in a Savannah ALD chamber using previously reported methods. Cyclopentadienylindium was used as the indium precursor and deposition was carried out at 180°C. These conditions correspond to a growth rate of about 0.15 nm per ALD cycle.[74] EP measurements of each sample yield porosity in agreement with the porosity expected with this growth rate using a spherical pore model. SEM images of ITO NC films following IO ALD show NCs become increasingly sintered (Figure 4.1b-f). Scherrer analysis of the ITO (222) XRD peak show a gradual increase to NC size, as expected for epitaxial growth of IO of ITO NCs. To understand the influence of contact radius, dopant concentration, and NC size on film electronic properties when surface depletion is suppressed, all films were capped with 40 ALD cycles of alumina deposition to passivate NC surfaces in accordance with previous literature.[26,27,29,45] A similar approach was use Lanigan and Thimsen who reported using

ZnO ALD on ZnO NCs to modify contact radius and alumina ALD to passivate film surfaces.

Room temperature conductivity measurements were collected on an Ecopia Hall Effect measurement system (HMS-5000) in the 4-point probe Van der Pauw geometry. Gold spring-clip contacts were placed directly on the films and edge effects were minimized by isolating a uniform square region in the center of the film using a diamond scribe. Variable temperature conductivity measurements were conducted in a Physical Property Measurement System (PPMS) from as low as 2 K up to 300 K in both decreasing and increasing temperature directions. Ohmic contact was established using indium solder pads.

RESULTS

To investigate the Chen criterion for MIT of doped semiconductor NC films, it was necessary to synthesize a series of NCs with precise size and dopant concentration to control electron concentration. Specifically, using adaptations of synthetic methods advanced by Jansons et al, 20nm ITO NCs with 0, 3, and 5 atomic% Sn and 15nm ITO NCs with 3 atomic% Sn were synthesized. NC electron concentration was assessed by fitting the localized surface plasmon resonance (LSPR) optical extinction spectrum with the heterogeneous Drude model developed by Staller et al. Details of each sample are summarized in Table 4.1. Following deposition of NC films, native ligands on NC surfaces were displaced with hydroxyls in situ to decrease inter-NC distance and create a reactive surface for ALD. Inter-NC contact radius was varied using indium oxide ALD. Electron concentration of NCs without IO ALD were assumed to be equal to those of colloidal NCs and IO filled samples electron concentration was calculated from the volume fraction of conductive material before and after IO ALD as measured by EP. Finally, film surfaces were passivated using alumina ALD to remove remaining adsorbed water species.

Table 4.1: ITO NCs.

Sample name	NC radius (nm)	Dopant concentration (at% Sn)	Electron concentration (cm^{-3})
0_20	10.0±1.6	0	4.2E19
3_20	10.2±0.6	2.96±0.01	5.5E20
5_20	10.2±0.9	4.97±0.01	8.3E20
3_15	7.5±0.6 (approx.)	3 (approx.)	5.5E20 (approx.)

Room temperature conductivity is plotted against the Chen criterion in Figure 4.2. Film conductivity increases approximately with $(k_F r_c)^2$ as expected by the Sharvin equation. The 0 atomic% Sn NC series increased from 19.0 S/cm at 1 nm contact to 155.0 S/cm at 9.6 nm contact. The 3 atomic% Sn NC series increased from 9.4 S/cm at 1 nm contact to 247.5 S/cm at 4.2 nm contact. The 5 atomic% Sn NC series increased from 14.0 S/cm at 1 nm contact to 450.0 S/cm at 5.3 nm contact. The striking increase in film conductivity requires a more thorough examination to uncover the underlying physics.

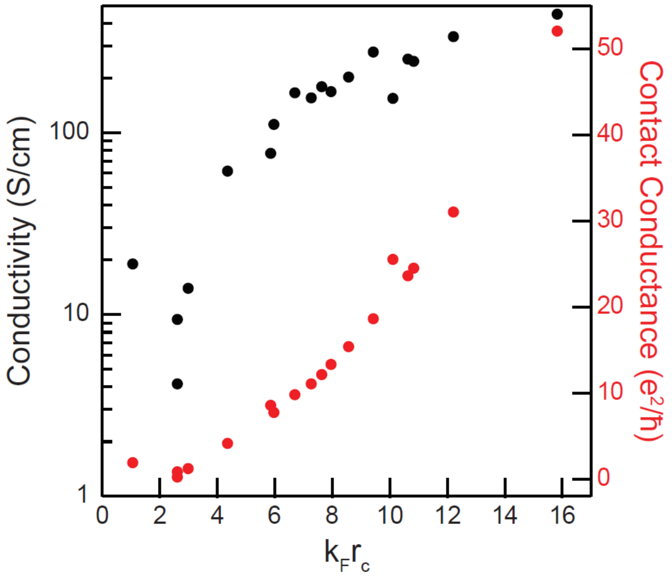

Figure 4.2: Film conductivity. Room temperature conductivity and contact conductance for Sn ITO NC films across a range of Chen criterion values.

Examination of the physics governing electron transport through an ensemble of NCs requires films to be viewed as a random resistor network composed of inter-NC resistors with conductance, g_C, and intra-NC resistors with conductance, g_{NC}. The conductance of an electron moving for the center of NC i to the center of NC j, known as bond resistance, g_{bond}, is calculated from the links and nodes model[45,46] as

$$\frac{1}{g_{bond}} = \frac{1}{g_C} + \frac{1}{g_{NC}} = \frac{q^2(\varphi - \varphi_0)^{1.9}}{h r_{NC} \sigma} \qquad (4.4)$$

where σ is the ensemble conductivity, φ is the film porosity, and φ_0 is the percolation threshold. The percolation threshold for random close packed spheres is 0.2.[29,47] The intra-NC conductance is defined using surface damping function discussed in Chapter 3 as

$$g_{NC} = \frac{r_{NC} n_e}{m_e^* \Gamma} = \frac{2 r_{NC} \pi^{\frac{1}{3}} n_e^{\frac{2}{3}}}{3^{\frac{1}{3}}} \left(\frac{1}{l_{MFP}} + \frac{1}{r_{NC}} + \frac{1}{r_c} \right) \qquad (4.5)$$

where m_e^* is the effective electron mass, Γ is the scattering frequency, l_{MFP} is the bulk mean free path, r_c is the contact radius. For samples with no IO ALD, the contact radius is defined by a tunneling junction contact, known as a b-contact. For this case, the contact radius is $\sqrt{2 r_{NC} b}$ where r_{NC} is the NC radius and b is the wavefunction decay rate, which depends on the material work function. Using the work function of alumina (4.7 eV), the b-contact radius of 20nm NCs is approximately 1nm. Given a contact conductance, the radius of contact between neighboring NCs can be calculated using the Sharvin equation as

$$r_c = \sqrt{\frac{4 g_C}{k_F^2}} \qquad (4.6)$$

Figure 2 shows the relationship between contact conductance and contact radius for the samples presented here. Contact conductance mirrors the trends with contact radius observed in conductivity. The Chen criterion is based on the concept that a NC network will exhibit metallic conduction when $g_C > g_Q$ where g_Q is the quantum resistance, unity. The contact conductance is above the quantum conductance for nearly all samples presented here, implying they are metallic under the Chen criterion. Variable temperature conductivity measurements of each sample are made to investigate the presence of metallic transport (Figure 4.3).

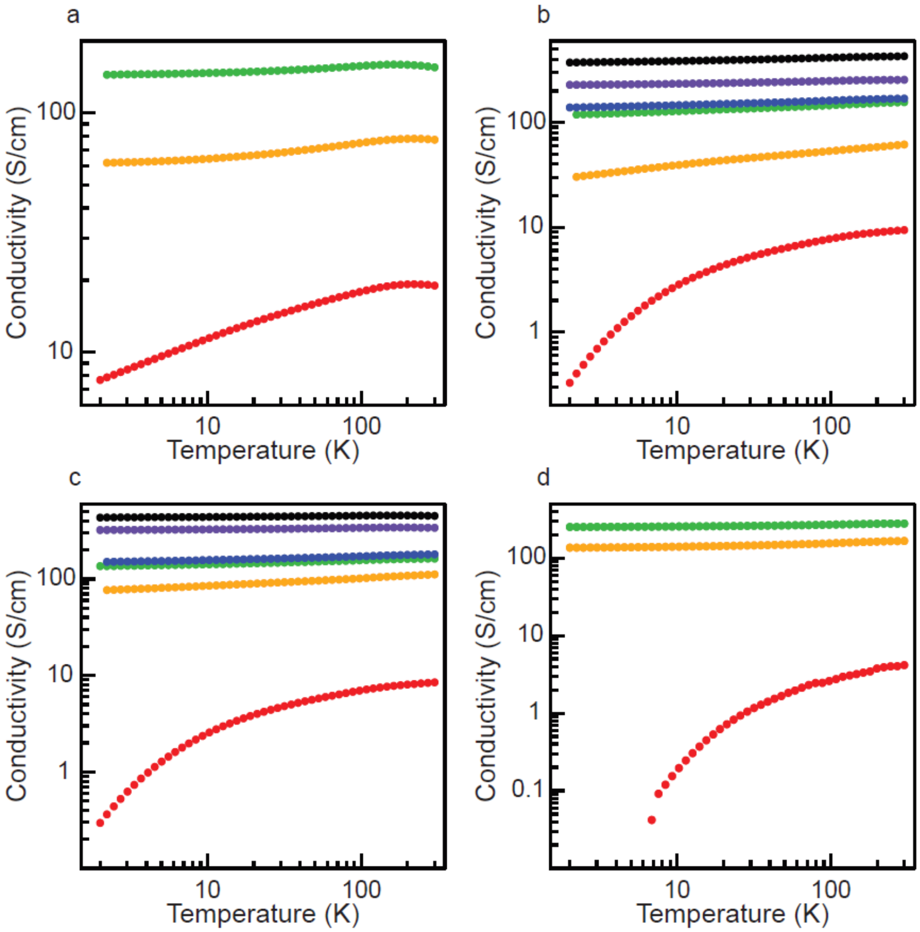

Figure 4.3: Variable Temperature Conductivity Data.

Figure 4.3a-c shows the presence of multiple conduction mechanisms across the measured temperature range. Of principal interest, all but one sample meet the Chen criterion and show a nonzero conductivity at 0K, though all of the measured samples maintain an increasing conductivity with temperature at low and intermediate temperatures. Across all sample series, the temperature dependence of conductivity flattens with increasing contact radius. This is indicative of an increased electron localization length or tunneling conductance, consistent with Figure 4.2.

ANALYSIS AND DISCUSSION

The insulating side of the NC film MIT has been thoroughly investigated by several groups. However, the metallic side of the MIT remains opaquely defined. In order to establish the metal-insulator phase diagram, the definition of a metal must be defined very specifically. Metals are somewhat dubiously defined; comments herein will use the following definitions: (1) a metal is strictly defined as a material that exhibits nonzero conductivity at 0K and (2) metallic conduction mechanism refers to a metal displaying decreasing conductivity with increasing temperature, i.e. a negative thermal coefficient of resistivity (TCR). The MIT refers to the interface of insulating behavior and metal as defined by (1). There are several reports of NC films exhibiting a nonzero conductivity at 0K that maintain a negative TCR.

Three distinct regimes for electron conduction through NC films are defined herein: insulator ($g_C < g_T^c < g_{NC}$), metal ($g_{NC} > g_C \geq g_T^c$), and conventional metal ($g_C > g_{NC}$). The inter-NC conductance is calculated from the Sharvin equation, which is considered valid unless neighboring contacts are defined by a b-contact and the critical tunneling conductance in 3D is defined by

$$g_T^c = \frac{\ln\left(\frac{E_C}{\delta}\right)}{6\pi} \qquad (4.7)$$

where $E_C = \frac{e^2}{2\pi\varepsilon\alpha}$ is the charging energy of a grain and $\delta = \left(g_{E_F}V_{NC}\right)^{-1}$ where g_{E_F} is the density of states at the Fermi energy and V_{NC} is the NC volume. With these criteria, a NC electron transport phase diagram is constructed in Figure 4.4a for 20nm NCs at electron concentrations of 1E19, 1E20, and 1E21 cm^{-3}.

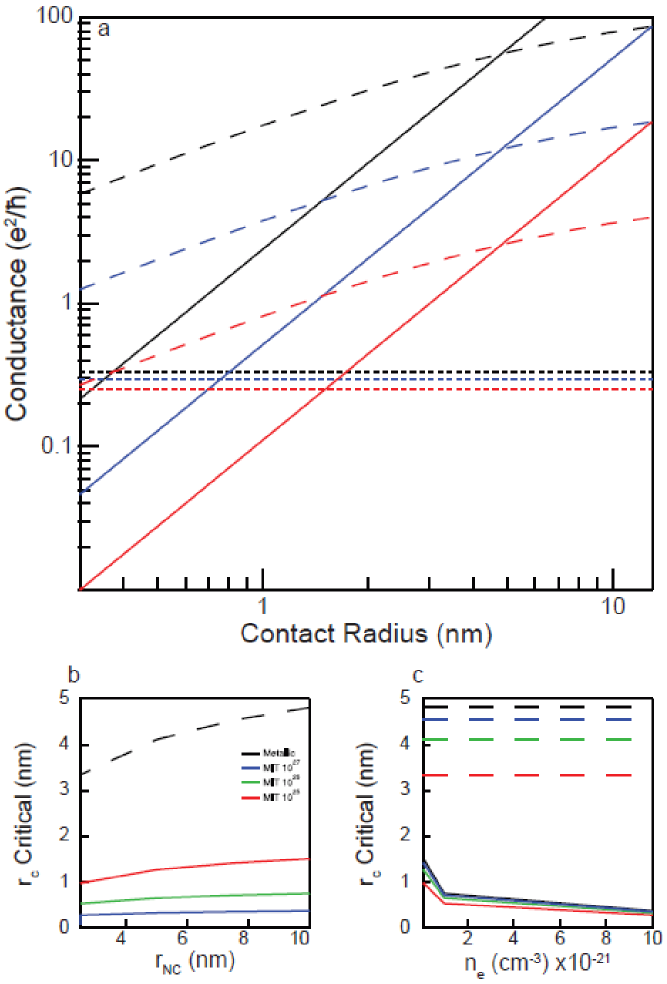

Figure 4.4: NC Transport Phase Diagram.

The NC transport phase diagram in Figure 4a illustrates the critical contact radius for the MIT depends on electron concentration. The critical contact radius at which the film shows metallic transport does not depend on electron concentration, as shown in Figure 4.4b. This results from (4.1) and (4.5) having the same electron concentration dependence. Interestingly, the critical contact radius does weakly depend on NC radius due to g_T^c containing a logarithmic dependence on NC size. In contrast, the critical contact radius at which the film shows metallic transport shows a quite significant dependence on NC size, resulting from the surface scattering dependence of g_{NC} (Figure 4.4c).

For insulators, $g_C < g_T^c$, electrons are localized to finite energetic wells of some characteristic size, a, defined by the inverse of the wavefunction decay rate. Migration of electrons between wells in such a system proceeds through an inelastic tunneling process referred to as hopping. Hopping transport is described by the general equation

$$\sigma = \sigma^* \exp\left(\left(\frac{T_0}{T}\right)^m\right) \quad (4.8a)$$

where σ^* is a material constant, T_0 is the characteristic temperature, T is the system temperature, and m depends on the specific hopping mechanism. Zabrodskii analysis for insulating samples in this work shows $m = 0.78$, corresponding to Efros-Shklovskii variable-range hopping with a Gaussian dispersion of energy levels (ES-VRH-GD). The ES-VRH-GD mechanism describes the thermal activation of electrons that are prohibited from motion due to a capacitive energy barrier known as charging energy. The ES-VRH-GD characteristic temperature is then defined as

$$T_0 = \left(\frac{3.15q^4}{4\pi^2\varepsilon^2 k_B C a^2}\right)^{\frac{1}{3}} \quad (4.8b)$$

where $C \approx 27$ is the heat capacity power-law coefficient for ITO and ε is the dielectric constant of the film. The film effective dielectric constant was calculated using methods developed by Reich and Shklovskii. Here, the electron localization length, a, defines the diameter of a sphere within which mobile electrons are confined at 0K. Only one sample measured here meets the criterion of an insulator and shows ES-VRH-GD conduction. Variable temperature data for 15nm ITO NCs with 0x IO ALD and fits to ES-VRH-GD model are shown in Figure 4.5. The sample shows a localization length of 15.4nm, indicating that electrons are confined to individual NCs.

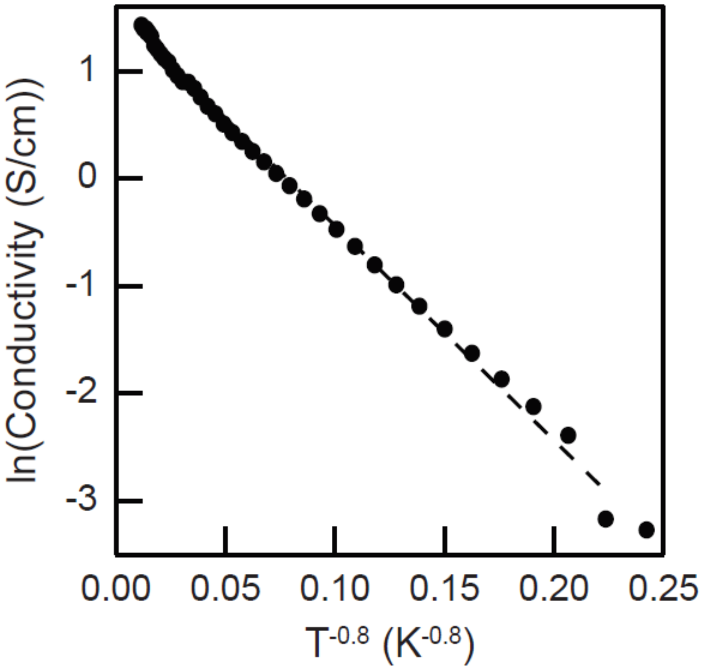

Figure 4.5: Efros-Shklovskii Variable Range Hopping Fit for 15nm 3 atomic% ITO NCs

Near the MIT, $g_C \sim g_T^c$, electrons become delocalized and may move through non-hopping processes. ITO NC films with $g_C > g_T^c$ are observed to exhibit a granular metal conduction mechanism. While hopping processes describe the activation of electron migration through thermally overcoming spatial and energetic barriers to transport, granular metals are defined by the competition between NC-NC coupling and electron charging energy. The conductivity of granular metals at moderate temperatures is defined by

$$\sigma = \sigma_0 \left(1 + \frac{1}{2\pi g_T d} \ln\left(\frac{k_B T}{g_T E_C}\right)\right) \qquad (4.9)$$

where $\sigma_0 = g_T \left(\frac{2e^2}{\hbar}\right) \alpha^{2-d}$, g_T is the non-dimensional tunneling conductance between grains, α is the grain diameter, d is the system dimensionality, and $E_C = \frac{e^2}{2\pi\varepsilon\alpha}$ is the charging energy of a grain. Fits to granular metal conduction mechanisms are shown in Figure 4.6.

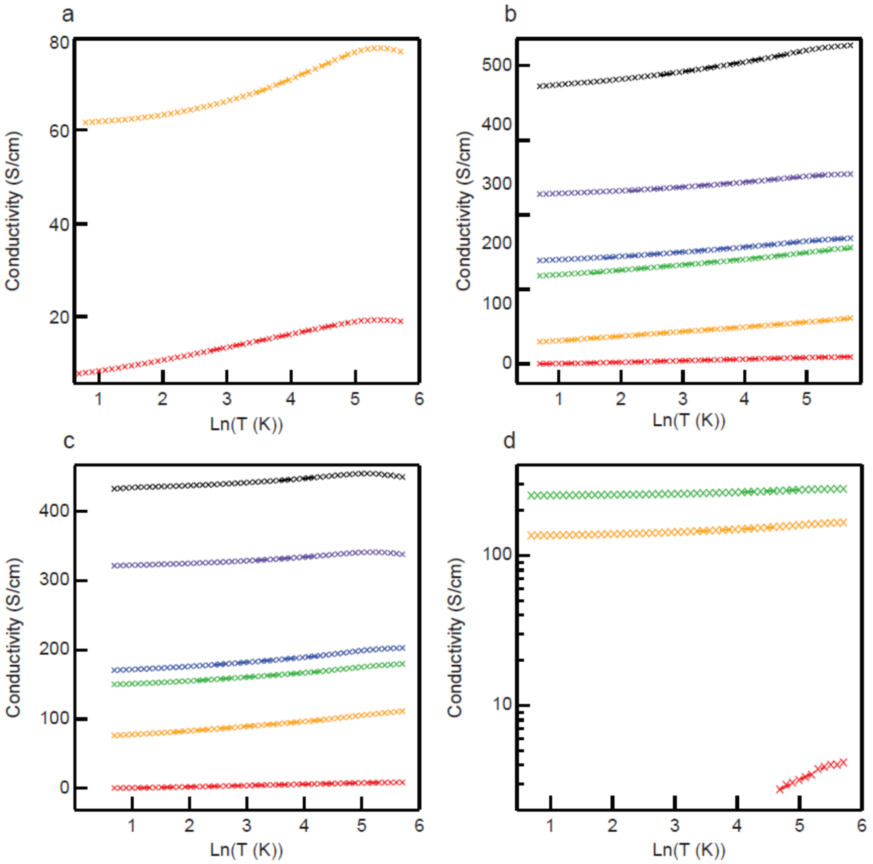

Figure 4.6: Granular Metal Fits.

The granular metal conduction model accurately described electron conduction over some temperature interval in each sample measured. Intercept and slope of conductivity vs ln(T) linear fits are used to calculate grain size and tunneling conduction. Interestingly, the grain size values for samples without IO ALD were equivalent to the NC size while after IO ALD, grain size ranged from 1nm to 4nm. This may indicate that conduction is limited by the NC size before IO ALD and the contact area after ALD, analogous to the Sharvin equation. The tunneling conductance for each sample is plotted in Figure 4.7. Tunneling conductance from the granular metal model is lower than those calculated from the links and nodes model across all samples. Interestingly, while the links and nodes model contact conductance follows the $(k_F r_c)^2$ trend expected from the Sharvin equation, the granular metal model tunneling conductance is instead linear with $k_F r_c$.

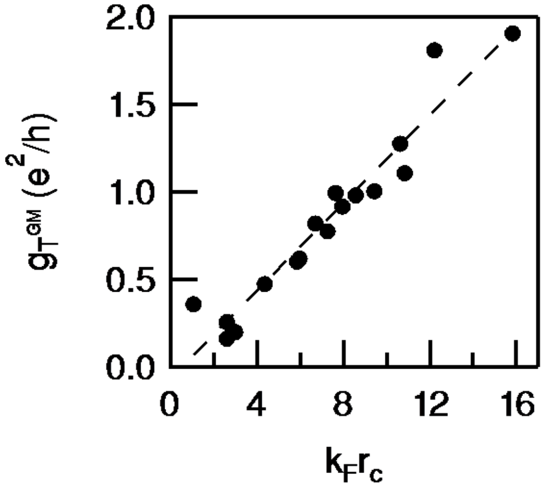

Figure 4.7: Granular Metal tunneling Conductance.

The granular metal model is valid for $T > \Gamma$ where $\Gamma = \frac{g_T\delta}{k_B}$ and $\delta = \left(g_{E_F}V_{NC}\right)^{-1}$ where g_{E_F} is the density of states at the Fermi energy and V_{NC} is the NC volume. Below this temperature, the logarithmic temperature dependence is invalid and electron physics is dominated by electron motion on scales larger than a NC-NC junction. This conduction is referred to as a Fermi liquid and is described in 3D by

$$\sigma = \sigma_0\left(1 + \frac{1}{2\pi g_T d}\ln\left(\frac{k_B\delta}{E_C}\right) + \frac{\alpha}{12\pi^2 g_T}\sqrt{\frac{T}{\Gamma}}\right) \quad (4.10)$$

where $\alpha \approx 1.38$. Fits to Fermi liquid conduction mechanisms are shown in Figure 4.8. The upper temperature for which the Fermi liquid model is valid increases with contact radius for each series. This is simply a result of increased tunneling conductance with increased contact radius.

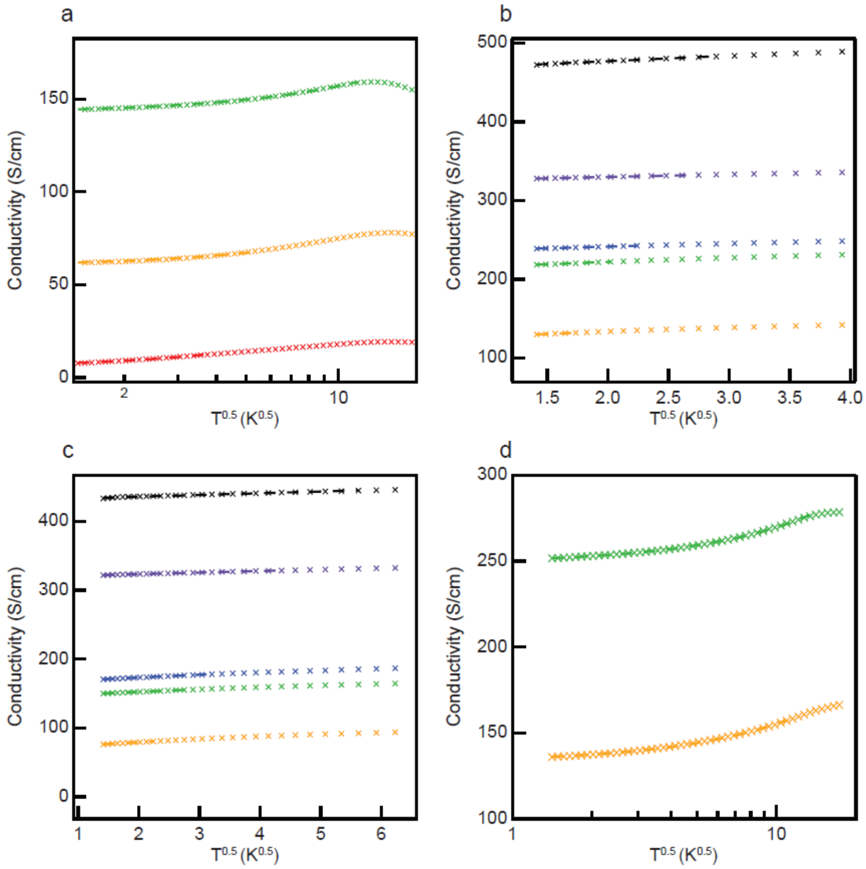

Figure 4.8: Fermi Liquid Fits.

Finally, when $g_C \sim g_{NC}$ the film conduction is limited by intra-NC conductance and the thermal dependence of conduction is metallic. From the links and nodes model, the conduction can be illustrated as an intra-NC resistor and inter-NC resistor in series. The thermal dependence of conductivity is a summation of inter- and intra-NC conduction and can be expected to depend most strongly on the most resistive component. The temperature dependence of the intra-NC resistor is expected to be similar to that of an ITO thin film, which is known to be

$$\rho = \rho_0(1 + \alpha(\Delta T)) \quad (4.11)$$

where ρ is the film resistivity, ρ_0 is the film resistivity at a reference temperature, α is the TCR, and ΔT is the difference in temperature from the reference temperature. Accounting for resistors in series, the granular metal or Fermi liquid model fit is subtracted from film resistivity to yield the measurable contribution from metallic conduction. Data and metallic conduction fits are shown in Figure 4.9.

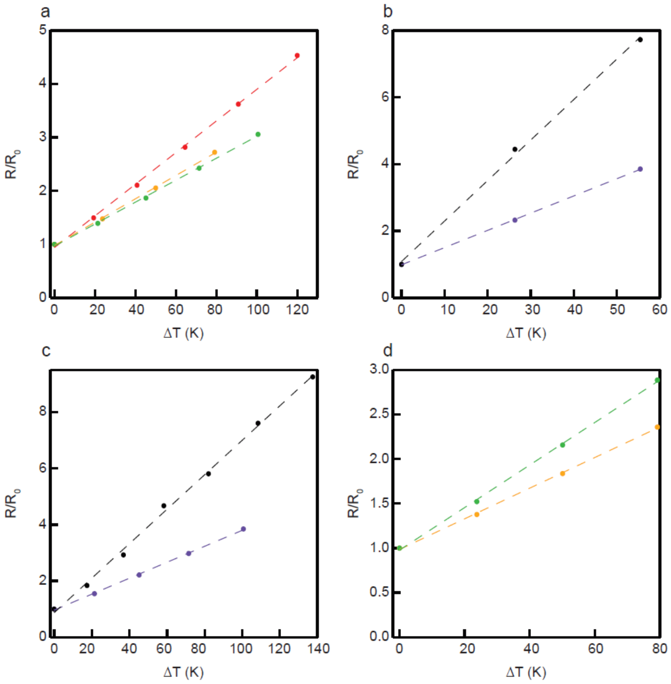

Figure 4.9: Metallic Transport.

We have shown that the NC contact conductance, g_C, varies strongly with $k_F r_c$ and the phase diagram for NC transport has three dominant regimes. These regimes describe the MIT and the transition to metallic conduction. NC films with a contact conductance below the critical value (g_T^c) conduct electrons through a hopping mechanism. Upon increasing inter-NC conductance through increasing electron concentration or contact radius such that $g_C \geq g_T^c$ the films undergo a MIT, processing nonzero conductivity at 0K and behaving as granular metals. Increasing the NC radius or contact radius such that $g_C{\sim}g_{NC}$ causes NC film conductivity to be limited by intra-NC conductance and thermal dependence becomes metallic.

Appendix I: Heterogeneous Model LSPR Fitting Code

File 1: “Extended Drude Broadened Fit”

```
%% Initialize global variables for fitting

global epsilonNC epsilonSolvent pathLength
epsilonNC=4.0;            % Dielectric background constant of nanocrystal (ITO=4)
epsilonSolvent=1.505^2; % T   E Host/solvent Dielectric Consta
lowFreqCutoff=3000;     % Low frequency cutoff for fitting in wavenumbers
hiFreqCutoff=10000;      % High frequency cutoff for fitting in wavenumbers
pathLength=0.05;       %Pathlength in cm

%% Load data

% The data should be in a text file named "spectrum_to_fit" and they should
% be formatted so that wavenumbers are in the first column and absorption
% values are in the second column
sample_name='sg5_5nm_Dil5'
spectrum=dlmread('sg5_5nm_Dil5.txt','\t',2,0);
wavenumbers=spectrum(:,1);  %load regular frequency values in cm-1
absorption=spectrum(  :,2);   %load absorption values


%set limits of fitting and grab indices
limits=find(wavenumbers>lowFreqCutoff&wavenumbers<hiFreqCutoff);
reducedFrequency=wavenumbers(limits);
reducedAbsorption=absorption(limits);%extract frequencies

%% Drude Model (freqency independent damping)

global n_point p

n_point= 41

% p -- a vector of pre parameters:
%       p(1) -- radius stdev
%       p(2) -- radius mu_r
%       p(3) -- volume fraction

p = [1 2 3];
```

```matlab
%% Fitting

options=optimoptions('lsqcurvefit','Algorithm','trust-region-
reflective','MaxFunEvals',1e20,'MaxIter',5e10,'TolFun',1e-14,'TolX',1e-15);
op.Display='on';
op.Plot=0;
op.ErrorsUnknown=1;              %set this to 1 if measurement uncertainties are unknown
op.MaxFunEvals=1e20;
op.TolX=1e-20;                   %Smallest step tolerance
op.TolFun=1e-20;
op.MaxIter=1e20;                 %Maximum iterations possible

            % ne   ne_stdev   dep
LowerBound =  [1*10^24 1*10^23 1*10^24];
initialGuess= [4*10^26 4*10^25 10*10^26];
UpperBound =  [2*10^27 1*10^27 1*10^27];
disp('$$$$$$$$$$$$$$$$$$$$$$$$$$$$$$$$$$$$$$$$$$$$')
disp('Broadened Drude')

paramsITO_ed=lsqcurvefit(@drude_broad_sol,initialGuess,reducedFrequency,reducedA
bsorption,LowerBound,UpperBound,options);
ne_mu=paramsITO_ed(1)
ne_sigma=paramsITO_ed(2)
dep=paramsITO_ed(3)/10^27


Predicted=drude_broad_sol(paramsITO_ed,reducedFrequency);
sample_name_fit=strcat(sample_name,'_fit');
plot(reducedFrequency,reducedAbsorption,'b',reducedFrequency,Predicted,'r--')

hold on
 set(gca,'XDir','reverse')
 set(gca,'box','on','xminortick','off','yminortick','off')
  set(gca,'fontsize',12,'fontweight','bold','linewidth',1,'ticklength',[0.02 0.02])
   ylabel('Extinction')
  xlabel('Wavenumber (cm^-^1)')
 legend('OriginalSpectrum','Fit','Location','Best')
  legend('Boxoff');
```

File 2: “drude_broad_sol”

```
function A=drude_broad_sol(a,omega)
%This function is used to calculate the plasmonic absorbance spectrum of an ensemble of
NCs
%It uses a 2 dimensional probability distribution function and sums the normalized
absorbance spectrum
%of each element of the PDF which is distributed in damping constant and plasma
frequency.
%   Input variables
%       omega -- frequency variable in cm^-1
%           a -- a vector of fit parameters:
%        a(1) -- plasma frequency expectation value cm^-1 mu_wp               (omega_p)
%        a(2) -- plasma frequency standard deviation cm^-1 sigma_wp
%        a(3) – volume fraction of mobile electrons fe
%
%         p -- a vector of fit parameters:
      % p(1) -- sigma_r
%        p(2) -- mu_r
%        p(3) -- volume fraction
% Output variable
% A -- absorbance of the layer

global epsilonNC epsilonSolvent pathLength n_point lower_limit upper_limit p
vol_frac=p(3);
ravg=p(2);
rstdev=p(1);
l=17;

nestdev=a(2);

r_range=(linspace(ravg-3*rstdev,ravg+3*rstdev,n_point))';
ne_range=linspace(a(1)-3*nestdev,a(1)+3*nestdev,n_point);
r_pdf=normpdf(r_range,ravg,rstdev)';
ne_pdf=normpdf(ne_range,a(1),nestdev);
dep=a(3)*10^-27;

abs_ensemble=zeros(length(omega),1);
PD=zeros(n_point,n_point);
T_PD=0;
V=0;
delr=(r_range(2)-r_range(1));
delne=(ne_range(2)-ne_range(1));
```

```
gamma=(((1.055*10^-34)*(3*pi^2)^(1/3)/(0.4*9.11*10^-
31*3*10^10*2*pi)).*ne_range.^(1/3).*(1./(4/3*r_range*10^-9*dep^(1/3))+1/(l*10^-9)));

omega_P=((ne_range)*(1.6*10^-19)^2/((8.85*10^-12)*(0.4*9.11*10^-
31))).^(1/2)/(3*10^10)/2/pi;

omega_s=((10^24)*(1.6*10^-19)^2/((8.85*10^-12)*(0.4*9.11*10^-
31))).^(1/2)/(3*10^10)/2/pi;

   for i = 1:n_point
   for j =1:n_point
            eshell=epsilonNC-omega_s^2./(omega.^2+1i*omega.*(gamma(i,j)));
            epsilonParticle=epsilonNC-
omega_P(i)^2./(omega.^2+1i*omega.*(gamma(i,j)));
            e_eff_particle=eshell.*(dep*(epsilonParticle+2*eshell)+2*(epsilonParticle-
eshell))./(dep*(epsilonParticle+2*eshell)-(epsilonParticle-eshell));
            sigA=4*r_range(j)^3*dep*2*pi^2*omega*sqrt(epsilonSolvent).*imag((
e_eff_particle-epsilonSolvent)./( e_eff_particle+2*epsilonSolvent));
            abs1=sigA;
            absc(i,j,:)=abs1;
            PD(i,j)=delr*delne*r_pdf(j)*ne_pdf(i);
            abs_ensemble=abs_ensemble+PD(i,j)*abs1; % adding onto the total abs
            T_PD=T_PD+PD(i,j);       %finding the total area of PDF for normalizing
            V=V+4/3*pi()*r_range(j)^3*PD(i,j);
   end
   end
T_PD;
A=abs_ensemble*vol_frac*pathLength/(V*log(10));
end
```

Bibliography

(1) Ashcroft, N. W.; Mermin, N. D. *Solid State Physics*; Cengage Learning, 1976.

(2) Tanner, D. B.; Larson, D. C. Electrical Resistivity of Silver Films. *Phys. Rev.* **1968**, *166* (3), 652–655. https://doi.org/10.1103/PhysRev.166.652.

(3) Mott, N. F. Conduction in Non-Crystalline Systems. *Philos. Mag.* **1968**, *17* (150), 1259–1268. https://doi.org/10.1080/14786436808223200.

(4) Mott, N. F. Conduction in Non-Crystalline Materials. *Philos. Mag.* **1969**, *19* (160), 835–852. https://doi.org/10.1080/14786436908216338.

(5) Davis, E. A.; Mott, N. F. Conduction in Non-Crystalline Systems V. Conductivity, Optical Absorption and Photoconductivity in Amorphous Semiconductors. *Philos. Mag.* **1970**, *22* (179), 0903–0922. https://doi.org/10.1080/14786437008221061.

(6) Shklovskii, B. I.; Efros, A. L. *Electronic Properties of Doped Semiconductors*; Springer-Verlag Berlin Heidelberg GmbH.

(7) Miller, A.; Abrahams, E. Impurity Conduction at Low Concentrations. *Phys. Rev.* **1960**, *120* (3), 745–755. https://doi.org/10.1103/PhysRev.120.745.

(8) Efros, A. L.; Shklovskii, B. I. Coulomb Gap and Low Temperature Conductivity of Disordered Systems. *J. Phys. C Solid State Phys.* **1975**, *8* (4), L49. https://doi.org/10.1088/0022-3719/8/4/003.

(9) Frank, G.; Köstlin, H. Electrical Properties and Defect Model of Tin-Doped Indium Oxide Layers. *Appl. Phys. A* **1982**, *27* (4), 197–206. https://doi.org/10.1007/BF00619080.

(10) Tahar, R. B. H.; Ban, T.; Ohya, Y.; Takahashi, Y. Tin Doped Indium Oxide Thin Films: Electrical Properties. *J. Appl. Phys.* **1998**, *83* (5), 2631–2645. https://doi.org/10.1063/1.367025.

(11) Lounis, S. D.; Runnerstrom, E. L.; Bergerud, A.; Nordlund, D.; Milliron, D. J. Influence of Dopant Distribution on the Plasmonic Properties of Indium Tin Oxide Nanocrystals. *J. Am. Chem. Soc.* **2014**, *136* (19), 7110–7116. https://doi.org/10.1021/ja502541z.

(12) Lounis, S. D.; Runnerstrom, E. L.; Llordés, A.; Milliron, D. J. Defect Chemistry and Plasmon Physics of Colloidal Metal Oxide Nanocrystals. *J. Phys. Chem. Lett.* **2014**, *5* (9), 1564–1574. https://doi.org/10.1021/jz500440e.

(13) M. Pasquarelli, R.; S. Ginley, D.; O'Hayre, R. Solution Processing of Transparent Conductors: From Flask to Film. *Chem. Soc. Rev.* **2011**, *40* (11), 5406–5441. https://doi.org/10.1039/C1CS15065K.

(14) Barquinha, P.; Martins, R.; Pereira, L.; Fortunato, E. *Transparent Oxide Electronics*; John Wiley & Sons, Ltd: Chichester, UK, 2012.

(15) Kim, B. H.; Staller, C. M.; Cho, S. H.; Heo, S.; Garrison, C. E.; Kim, J.; Milliron, D. J. High Mobility in Nanocrystal-Based Transparent Conducting Oxide Thin Films. *ACS Nano* **2018**, *12* (4), 3200–3208. https://doi.org/10.1021/acsnano.7b06783.

(16) Ellmer, K. Past Achievements and Future Challenges in the Development of Optically Transparent Electrodes. *Nat. Photonics* **2012**, *6* (12), nphoton.2012.282. https://doi.org/10.1038/nphoton.2012.282.

(17) Kim, J.-Y.; Kotov, N. A. Charge Transport Dilemma of Solution-Processed Nanomaterials. *Chem. Mater.* **2014**, *26* (1), 134–152. https://doi.org/10.1021/cm402675k.

(18) Pham, H. T.; Jeong, H.-D. Newly Observed Temperature and Surface Ligand Dependence of Electron Mobility in Indium Oxide Nanocrystals Solids. *ACS Appl. Mater. Interfaces* **2015**, *7* (21), 11660–11667. https://doi.org/10.1021/acsami.5b02971.

(19) Zarghami, M. H.; Liu, Y.; Gibbs, M.; Gebremichael, E.; Webster, C.; Law, M. P-Type PbSe and PbS Quantum Dot Solids Prepared with Short-Chain Acids and Diacids. *ACS Nano* **2010**, *4* (4), 2475–2485. https://doi.org/10.1021/nn100339b.

(20) Talapin, D. V.; Murray, C. B. PbSe Nanocrystal Solids for N- and p-Channel Thin Film Field-Effect Transistors. *Science* **2005**, *310* (5745), 86–89. https://doi.org/10.1126/science.1116703.

(21) Liu, W.; Lee, J.-S.; Talapin, D. V. III–V Nanocrystals Capped with Molecular Metal Chalcogenide Ligands: High Electron Mobility and Ambipolar Photoresponse. *J. Am. Chem. Soc.* **2013**, *135* (4), 1349–1357. https://doi.org/10.1021/ja308200f.

(22) Wuelfing, W. P.; Green, S. J.; Pietron, J. J.; Cliffel, D. E.; Murray, R. W. Electronic Conductivity of Solid-State, Mixed-Valent, Monolayer-Protected Au Clusters. *J. Am. Chem. Soc.* **2000**, *122* (46), 11465–11472. https://doi.org/10.1021/ja002367+.

(23) Zabet-Khosousi, A.; Trudeau, P.-E.; Suganuma, Y.; Dhirani, A.-A.; Statt, B. Metal to Insulator Transition in Films of Molecularly Linked Gold Nanoparticles. *Phys. Rev. Lett.* **2006**, *96* (15), 156403. https://doi.org/10.1103/PhysRevLett.96.156403.

(24) Garcia, G.; Buonsanti, R.; Runnerstrom, E. L.; Mendelsberg, R. J.; Llordes, A.; Anders, A.; Richardson, T. J.; Milliron, D. J. Dynamically Modulating the Surface Plasmon Resonance of Doped Semiconductor Nanocrystals. *Nano Lett.* **2011**, *11* (10), 4415–4420. https://doi.org/10.1021/nl202597n.

(25) Dong, A.; Ye, X.; Chen, J.; Kang, Y.; Gordon, T.; Kikkawa, J. M.; Murray, C. B. A Generalized Ligand-Exchange Strategy Enabling Sequential Surface Functionalization of Colloidal Nanocrystals. *J. Am. Chem. Soc.* **2011**, *133* (4), 998–1006. https://doi.org/10.1021/ja108948z.

(26) Thimsen, E.; Johnson, M.; Zhang, X.; Wagner, A. J.; Mkhoyan, K. A.; Kortshagen, U. R.; Aydil, E. S. High Electron Mobility in Thin Films Formed via Supersonic Impact Deposition of Nanocrystals Synthesized in Nonthermal Plasmas. *Nat. Commun.* **2014**, *5*. https://doi.org/10.1038/ncomms6822.

(27) Ephraim, J.; Lanigan, D.; Staller, C.; Milliron, D. J.; Thimsen, E. Transparent Conductive Oxide Nanocrystals Coated with Insulators by Atomic Layer Deposition. *Chem. Mater.* **2016**, *28* (15), 5549–5553. https://doi.org/10.1021/acs.chemmater.6b02414.

(28) Liu, Y.; Gibbs, M.; Perkins, C. L.; Tolentino, J.; Zarghami, M. H.; Bustamante, J.; Law, M. Robust, Functional Nanocrystal Solids by Infilling with Atomic Layer Deposition. *Nano Lett.* **2011**, *11* (12), 5349–5355. https://doi.org/10.1021/nl2028848.

(29) Staller, C. M.; Robinson, Z. L.; Agrawal, A.; Gibbs, S. L.; Greenberg, B. L.; Lounis, S. D.; Kortshagen, U. R.; Milliron, D. J. Tuning Nanocrystal Surface Depletion by Controlling Dopant Distribution as a Route Toward Enhanced Film Conductivity. *Nano Lett.* **2018**, *18* (5), 2870–2878. https://doi.org/10.1021/acs.nanolett.7b05484.

(30) Zandi, O.; Agrawal, A.; Shearer, A. B.; Reimnitz, L. C.; Dahlman, C. J.; Staller, C. M.; Milliron, D. J. Impacts of Surface Depletion on the Plasmonic Properties of Doped Semiconductor Nanocrystals. *Nat. Mater.* **2018**, *17* (8), 710. https://doi.org/10.1038/s41563-018-0130-5.

(31) Agrawal, A.; Kriegel, I.; Runnerstrom, E. L.; Scotognella, F.; Llordes, A.; Milliron, D. J. Rationalizing the Impact of Surface Depletion on Electrochemical Modulation of Plasmon Resonance Absorption in Metal Oxide Nanocrystals. *ACS Photonics* **2018**, *5* (5), 2044–2050. https://doi.org/10.1021/acsphotonics.7b01587.

(32) Jansons, A. W.; Hutchison, J. E. Continuous Growth of Metal Oxide Nanocrystals: Enhanced Control of Nanocrystal Size and Radial Dopant Distribution. *ACS Nano* **2016**, *10* (7), 6942–6951. https://doi.org/10.1021/acsnano.6b02796.

(33) Talapin, D. V.; Lee, J.-S.; Kovalenko, M. V.; Shevchenko, E. V. Prospects of Colloidal Nanocrystals for Electronic and Optoelectronic Applications. *Chem. Rev.* **2010**, *110* (1), 389–458.

(34) Zabet-Khosousi, A.; Dhirani, A.-A. Charge Transport in Nanoparticle Assemblies. *Chem. Rev.* **2008**, *108* (10), 4072–4124.

(35) Liu, Y.; Tolentino, J.; Gibbs, M.; Ihly, R.; Perkins, C. L.; Liu, Y.; Crawford, N.; Hemminger, J. C.; Law, M. PbSe Quantum Dot Field-Effect Transistors with Air-Stable Electron Mobilities above 7 Cm2 V–1 s–1. *Nano Lett.* **2013**, *13* (4), 1578–1587. https://doi.org/10.1021/nl304753n.

(36) Greenberg, B. L.; Robinson, Z. L.; Reich, K. V.; Gorynski, C.; Voigt, B. N.; Francis, L. F.; Shklovskii, B. I.; Aydil, E. S.; Kortshagen, U. R. ZnO Nanocrystal Networks Near the Insulator–Metal Transition: Tuning Contact Radius and Electron Density with Intense Pulsed Light. *Nano Lett.* **2017**. https://doi.org/10.1021/acs.nanolett.7b01078.

(37) Zandi, O.; Agrawal, A.; Shearer, A. B.; Gilbert, L. C.; Dahlman, C. J.; Staller, C. M.; Milliron, D. J. Impacts of Surface Depletion on the Plasmonic Properties of Doped Semiconductor Nanocrystals. *ArXiv170907136 Cond-Mat Physicsphysics* **2017**.

(38) Hewitt, R. W.; Winograd, N. Oxidation of Polycrystalline Indium Studied by X-Ray Photoelectron Spectroscopy and Static Secondary Ion Mass Spectroscopy. *J Appl Phys* **1980**, *51* (5), 2620–2624.

(39) Space Charge Calculations for Semiconductors. *J. Appl. Phys.* **1958**, *29* (7), 1034–1040. https://doi.org/10.1063/1.1723358.

(40) Kang, M. S.; Sahu, A.; Norris, D. J.; Frisbie, C. D. Size-Dependent Electrical Transport in CdSe Nanocrystal Thin Films. *Nano Lett.* **2010**, *10* (9), 3727–3732. https://doi.org/10.1021/nl102356x.

(41) Liu, Y.; Gibbs, M.; Puthussery, J.; Gaik, S.; Ihly, R.; Hillhouse, H. W.; Law, M. Dependence of Carrier Mobility on Nanocrystal Size and Ligand Length in PbSe Nanocrystal Solids. *Nano Lett.* **2010**, *10* (5), 1960–1969. https://doi.org/10.1021/nl101284k.

(42) Chen, T.; Reich, K. V.; Kramer, N. J.; Fu, H.; Kortshagen, U. R.; Shklovskii, B. I. Metal-Insulator Transition in Films of Doped Semiconductor Nanocrystals. *Nat. Mater.* **2015**, *advance online publication*. https://doi.org/10.1038/nmat4486.

(43) Arginskaya, N. V.; Kozub, V. I. Potential Influence of Pre-Exponential Factors on the Temperature Dependence of Variable-Range Hopping Conductivity. *Sov. J. Exp. Theor. Phys.* **1994**, *79*, 466–472.

(44) Yildiz, A.; Serin, N.; Serin, T.; Kasap, M. Crossover from Nearest-Neighbor Hopping Conduction to Efros–Shklovskii Variable-Range Hopping Conduction in Hydrogenated Amorphous Silicon Films. *Jpn. J. Appl. Phys.* **2009**, *48* (11R), 111203. https://doi.org/10.1143/JJAP.48.111203.

(45) Lanigan, D.; Thimsen, E. Contact Radius and the Insulator–Metal Transition in Films Comprised of Touching Semiconductor Nanocrystals. *ACS Nano* **2016**, *10* (7), 6744–6752. https://doi.org/10.1021/acsnano.6b02190.

(46) Shklovskiĭ, B. I.; Éfros, A. L. Percolation Theory and Conductivity of Strongly Inhomogeneous Media. *Sov. Phys. Uspekhi* **1975**, *18* (11), 845. https://doi.org/10.1070/PU1975v018n11ABEH005233.

(47) Powell, M. J. Site Percolation in Randomly Packed Spheres. *Phys. Rev. B* **1979**, *20* (10), 4194–4198. https://doi.org/10.1103/PhysRevB.20.4194.

(48) Beloborodov, I. S.; Lopatin, A. V.; Vinokur, V. M. Universal Description of Granular Metals at Low Temperatures: Granular Fermi Liquid. *Phys. Rev. B* **2004**, *70* (20), 205120. https://doi.org/10.1103/PhysRevB.70.205120.

(49) Zabrodskii, A. G. The Coulomb Gap: The View of an Experimenter. *Philos. Mag. Part B* **2001**, *81* (9), 1131–1151. https://doi.org/10.1080/13642810108205796.

(50) Houtepen, A. J.; Kockmann, D.; Vanmaekelbergh, D. Reappraisal of Variable-Range Hopping in Quantum-Dot Solids. *Nano Lett.* **2008**, *8* (10), 3516–3520. https://doi.org/10.1021/nl8020347.

(51) Lin, J.-J.; Li, Z.-Q. Electronic Conduction Properties of Indium Tin Oxide: Single-Particle and Many-Body Transport. *J. Phys. Condens. Matter* **2014**, *26*.

(52) Reich, K. V.; Shklovskii, B. I. Dielectric Constant and Charging Energy in Array of Touching Nanocrystals. *Appl. Phys. Lett.* **2016**, *108* (11), 113104. https://doi.org/10.1063/1.4944407.

(53) Cordfunke, E. H. P.; Westrum, Jr, E. F. The Heat Capacity and Derived Thermophysical Properties of In2O3 from 0 to 1000 K. *J. Phys. Chem. Solids* **1992**, *53* (3), 361–365.

(54) Berggren, K.-F.; Sernelius, B. E. Band-Gap Narrowing in Heavily Doped Many-Valley Semiconductors. *Phys. Rev. B* **1981**, *24* (4), 1971–1986. https://doi.org/10.1103/PhysRevB.24.1971.

(55) Hamberg, I.; Granqvist, C. G.; Berggren, K.-F.; Sernelius, B. E.; Engström, L. Band-Gap Widening in Heavily Sn-Doped In_2O_3. *Phys. Rev. B* **1984**, *30* (6), 3240–3249. https://doi.org/10.1103/PhysRevB.30.3240.

(56) Beloborodov, I. S.; Lopatin, A. V.; Vinokur, V. M.; Efetov, K. B. Granular Electronic Systems. *Rev. Mod. Phys.* **2007**, *79* (2), 469–518. https://doi.org/10.1103/RevModPhys.79.469.

(57) Zhang, Y.-J.; Li, Z.-Q.; Lin, J.-J. Logarithmic Temperature Dependence of Hall Transport in Granular Metals. *Phys. Rev. B* **2011**, *84* (5), 052202. https://doi.org/10.1103/PhysRevB.84.052202.

(58) Beloborodov, I. S.; Efetov, K. B.; Lopatin, A. V.; Vinokur, V. M. Transport Properties of Granular Metals at Low Temperatures. *Phys. Rev. Lett.* **2003**, *91* (24), 246801. https://doi.org/10.1103/PhysRevLett.91.246801.

(59) Wang, Y.; Runnerstrom, E. L.; Milliron, D. J. Switchable Materials for Smart Windows. *Annu. Rev. Chem. Biomol. Eng.* **2016**, *7* (1), 283–304. https://doi.org/10.1146/annurev-chembioeng-080615-034647.

(60) Llordés, A.; Garcia, G.; Gazquez, J.; Milliron, D. J. Tunable Near-Infrared and Visible-Light Transmittance in Nanocrystal-in-Glass Composites. *Nature* **2013**, *500* (7462), 323–326. https://doi.org/10.1038/nature12398.

(61) Anker, J. N.; Hall, W. P.; Lyandres, O.; Shah, N. C.; Zhao, J.; Van Duyne, R. P. Biosensing with Plasmonic Nanosensors. In *Nanoscience and Technology*; Co-Published with Macmillan Publishers Ltd, UK, 2009; pp 308–319. https://doi.org/10.1142/9789814287005_0032.

(62) Harris, N.; Ford, M. J.; Cortie, M. B. Optimization of Plasmonic Heating by Gold Nanospheres and Nanoshells. *J. Phys. Chem. B* **2006**, *110* (22), 10701–10707. https://doi.org/10.1021/jp0606208.

(63) Herzog, J. B.; Knight, M. W.; Natelson, D. Thermoplasmonics: Quantifying Plasmonic Heating in Single Nanowires. *Nano Lett.* **2014**, *14* (2), 499–503. https://doi.org/10.1021/nl403510u.

(64) Donner, J. S.; Thompson, S. A.; Alonso-Ortega, C.; Morales, J.; Rico, L. G.; Santos, S. I. C. O.; Quidant, R. Imaging of Plasmonic Heating in a Living Organism. *ACS Nano* **2013**, *7* (10), 8666–8672. https://doi.org/10.1021/nn403659n.

(65) Jain, P. K.; Lee, K. S.; El-Sayed, I. H.; El-Sayed, M. A. Calculated Absorption and Scattering Properties of Gold Nanoparticles of Different Size, Shape, and Composition: Applications in Biological Imaging and Biomedicine. *J. Phys. Chem. B* **2006**, *110* (14), 7238–7248. https://doi.org/10.1021/jp057170o.

(66) Aksu, S.; Yanik, A. A.; Adato, R.; Artar, A.; Huang, M.; Altug, H. High-Throughput Nanofabrication of Infrared Plasmonic Nanoantenna Arrays for Vibrational Nanospectroscopy. *Nano Lett.* **2010**, *10* (7), 2511–2518. https://doi.org/10.1021/nl101042a.

(67) Huang, X.; El-Sayed, I. H.; Qian, W.; El-Sayed, M. A. Cancer Cell Imaging and Photothermal Therapy in the Near-Infrared Region by Using Gold Nanorods. *J. Am. Chem. Soc.* **2006**, *128* (6), 2115–2120. https://doi.org/10.1021/ja057254a.
(68) El-Sayed, I. H. Nanotechnology in Head and Neck Cancer: The Race Is On. *Curr. Oncol. Rep.* **2010**, *12* (2), 121–128. https://doi.org/10.1007/s11912-010-0087-2.
(69) Wokaun, A.; Gordon, J. P.; Liao, P. F. Radiation Damping in Surface-Enhanced Raman Scattering. *Phys. Rev. Lett.* **1982**, *48* (14), 957–960. https://doi.org/10.1103/PhysRevLett.48.957.
(70) Johns, R. W.; Bechtel, H. A.; Runnerstrom, E. L.; Agrawal, A.; Lounis, S. D.; Milliron, D. J. Direct Observation of Narrow Mid-Infrared Plasmon Linewidths of Single Metal Oxide Nanocrystals. *Nat. Commun.* **2016**, *7*, 11583. https://doi.org/10.1038/ncomms11583.
(71) Moroz, A. Electron Mean Free Path in a Spherical Shell Geometry. *J. Phys. Chem. C* **2008**, *112* (29), 10641–10652. https://doi.org/10.1021/jp8010074.
(72) Agrawal, A.; Johns, R. W.; Milliron, D. J. Control of Localized Surface Plasmon Resonances in Metal Oxide Nanocrystals. *Annu. Rev. Mater. Res.* **2017**, *47* (1), null. https://doi.org/10.1146/annurev-matsci-070616-124259.
(73) Sharvin, Y. V. ON THE POSSIBLE METHOD FOR STUDYING FERMI SURFACES. *Zh Eksperim Teor Fiz* **1965**, *Vol: 48*.
(74) Libera, J. A.; Hryn, J. N.; Elam, J. W. Indium Oxide Atomic Layer Deposition Facilitated by the Synergy between Oxygen and Water. *Chem. Mater.* **2011**, *23* (8), 2150–2158. https://doi.org/10.1021/cm103637t.